

# Asymmetrical S-Band Coupled Resonator Filters

Nicola Coetzee



Thesis presented in partial fulfilment of the requirements for the degree of  
Master of Science in Engineering at the University of Stellenbosch.

Supervisor: Prof. P. Meyer

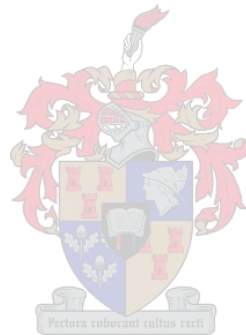
December 2005

# Declaration

I, the undersigned, hereby declare that the work contained in this thesis is my own original work and that I have not previously in its entirety or in part submitted it at any university for a degree.

N. Coetzee \_\_\_\_\_

Date \_\_\_\_\_



# Abstract

*Keywords* - Coupled Resonator Filter, Asymmetrical Transfer Function, Negative Coupling, Tapped Feed Line, Evanescent Mode, Capacitive Probe

Due to a more densely packed frequency spectrum, there is an increasing demand for narrow band filters with asymmetrical transfer function characteristics. The resulting coupling matrices contain both positive and negative couplings, cross couplings and individual resonator frequency offsets.

The non-negligible series inductance present in a tapped feed line structure, inverts the behaviour of the system impedance and also eliminates the use of certain parameter extraction methods. From a more accurate model of the feed line, theory is developed with which to measure the external Q-factor realised by the feed line.

Three different methods of establishing negative coupling are investigated, namely iris-, evanescent mode- and capacitive probe coupling. Filter dimensions play an important role in each of these coupling schemes, which are evaluated and compared in terms of their limitations and ease of implementation.

To compare the performance of different negative coupling elements, two fourth order filters with centre frequency of 3 GHz and bandwidth of 3% are designed, built and measured.

# Opsomming

*Sleutelwoorde* - Gekoppelde Resoneerder Filter, Asimetriese Oordragsfunksie, Negatiewe Koppeling, Getapte Voerlyn, Golfleier Onder Afknip, Kapasitiewe Probe

Een van die gevolge van die hedendaagse groter benutting van die frekwensiespektrum, is 'n toenemende aanvraag vir noubandfilters met asimetriese oordragsfunksies. Die ooreenstemmende koppelmatrakte bevat beide positiewe en negatiewe koppelings, sowel as kruiskoppelings en individuele resoneerder frekwensie-afsette.

Die nie-weglaatbare serie induktansie teenwoordig in die getapte voerlynstruktuur, inverseer die gedrag van die stelselimpedansie en elimineer sekere parameteronttrekkingsprosedures. Vanaf 'n meer akkurate model van die voerlyn word teorie ontwikkel wat die meting van die eksterne Q-faktor, wat deur die voerlyn gerealiseer word, moontlik maak.

Drie verskillende negatiewe koppelstrukture word ondersoek, naamlik iris-, golfleier onder afknip-, en kapasitiewe probe koppelstrukture. Elk van die bogenoemde strukture word ge-evalueer in terme van hul implementeringsgemak en beperkings. Daar is gevind dat filterafmetings 'n belangrike rol speel in die werking van die koppelstrukture.

Om die vergelyking van verskillende negatiewe koppelstrukture te bewerkstellig, is twee vierde orde filters ontwerp, gebou en getoets. Die filters het 'n sentrefrekwensie van 3 GHz en bandwydte van 3%.

# Acknowledgements

Without the grace of God, and the help and support of so many people, the completion of my thesis would never have been a reality.

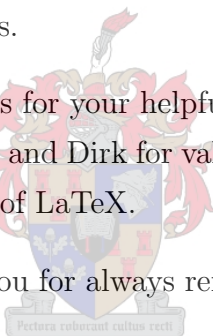
Firstly, I have to thank my study leader Prof. Petrie Meyer, whose never-ending patience and positive attitude made this valuable learning experience such a pleasant one.

For the precise and careful manufacturing of the two filters, I am indebted to Mr Wessel Croukamp and Mr Lincon Saunders. Your meticulous attention to detail lead to the successful realisation of my designs.

Thank you to all my E206 partners for your helpful insights and regular Plakkies breaks. Special thanks to Marlize, Thomas and Dirk for valuable proofreading and help with some of the more interesting challenges of LaTeX.

To my family and friends, thank you for always reminding me how much more there is to life outside of the office doors.

Lastly, I have to thank my fiance Ian, whose love is even more constant and sure than Maxwell's equations.



# Contents

<b>List of Tables</b>	<b>viii</b>
<b>List of Figures</b>	<b>ix</b>
<b>1 Introduction</b>	<b>1</b>
1.1 Historical Perspective . . . . .	1
1.2 Project Background . . . . .	2
1.3 About the Thesis . . . . .	2
<b>2 Basic Theory of Narrow Band Coupled Resonator Filter Synthesis</b>	<b>4</b>
2.1 Introduction . . . . .	4
2.2 Manipulation of the General Equivalent Circuit . . . . .	4
2.3 Equation of Y-parameters . . . . .	9
2.4 Conclusion . . . . .	10
<b>3 General Coupling Matrix Synthesis Methods for Chebyshev Filtering Functions</b>	<b>11</b>
3.1 Introduction . . . . .	11
3.2 Transfer and Reflection Polynomial Synthesis . . . . .	12
3.3 Synthesis of the Coupling Matrix . . . . .	16
3.4 Conclusion . . . . .	18
<b>4 Physical Realisation of the Coupling Matrix</b>	<b>19</b>
4.1 Introduction . . . . .	19

4.2	Resonant Cavities . . . . .	19
4.3	Positive Coupling Mechanisms . . . . .	22
4.4	Negative Coupling Mechanisms . . . . .	25
4.4.1	Iris Coupling . . . . .	25
4.4.2	Evanescent Mode Coupling . . . . .	31
4.4.3	Capacitive Probe Coupling . . . . .	39
4.5	Port Impedance Transformation . . . . .	40
4.5.1	Inductance in the Feed Structure . . . . .	41
4.5.2	Measurement of the External Q-factor . . . . .	45
4.6	Realisation of Coupling Matrix Diagonal Entries . . . . .	50
4.7	Conclusion . . . . .	51
<b>5</b>	<b>Parameter Extraction from Simulation and Measurements</b>	<b>52</b>
5.1	Introduction . . . . .	52
5.2	Extraction with a Short-Circuited Final Cavity . . . . .	53
5.2.1	Coupling Coefficients from $\angle S_{11}$ . . . . .	53
5.2.2	Computer-Aided Parameter Extraction from $\angle S_{11}$ . . . . .	56
5.2.3	A Deterministic Tuning Procedure with $\angle S_{11}$ . . . . .	59
5.2.4	Parameter Extraction via $S_{11}$ Group Delay . . . . .	62
5.3	Parameter Extraction via Optimisation . . . . .	64
5.3.1	Automated Filter Tuning Using Gradient-Based Parameter Extrac- tion . . . . .	65
5.3.2	Sequential Tuning Using Adaptive Models and Parameter Extraction	68
5.3.3	Parameter Extraction in Microwave Office . . . . .	71
5.4	Conclusion . . . . .	74
<b>6</b>	<b>Prototype Filters</b>	<b>77</b>

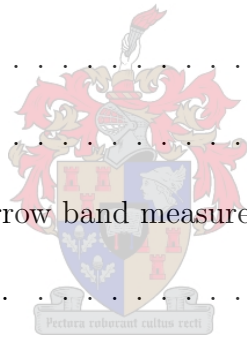
6.1	Introduction . . . . .	77
6.2	Coupling Matrix Synthesis . . . . .	77
6.3	The External Q-factor . . . . .	79
6.4	Prototype Filter 1 . . . . .	80
6.4.1	Filter dimensions . . . . .	80
6.4.2	Measurements . . . . .	82
6.5	Prototype Filter 2 . . . . .	85
6.5.1	Filter Dimensions . . . . .	85
6.5.2	Measurements . . . . .	87
6.6	Conclusion . . . . .	90
<b>7</b>	<b>Conclusion</b>	<b>91</b>
<b>A</b>	<b>Bandwidth and Frequency Scaling of the Coupling Matrix</b>	<b>93</b>
<b>B</b>	<b>Impedance and Admittance Inverters</b>	<b>95</b>
B.1	General Definition . . . . .	95
B.2	Equivalent Circuits of K- and J-inverters . . . . .	96
<b>C</b>	<b>Derivation of Two Port Driving Point Impedance</b>	<b>99</b>
	<b>Bibliography</b>	<b>101</b>





# List of Tables

4.1	Q-factor simulations with different cavity $z$ -dimensions. . . . .	21
4.2	Unloaded Q-factor as a function of resonator post diameter. . . . .	26
6.1	Filter specifications. . . . .	77
6.2	Dimensions of Fig. 6.4. . . . .	81
6.3	Dimensions of Fig. 6.5. . . . .	81
6.4	Dimensions of Fig. 6.6. . . . .	82
6.5	Dimensions of Fig. 6.7. . . . .	82
6.6	Summary of filter 1 narrow band measurements. . . . .	84
6.7	Dimensions of Fig. 6.12. . . . .	86
6.8	Dimensions of Fig. 6.13. . . . .	86
6.9	Dimensions of Fig. 6.14. . . . .	87
6.10	Dimensions of Fig. 6.15. . . . .	87
6.11	Summary of filter 2 narrow band measurement. . . . .	87
6.12	Comparison between MWO and CST results. . . . .	89
B.1	Summary of impedance and admittance inverters. . . . .	98



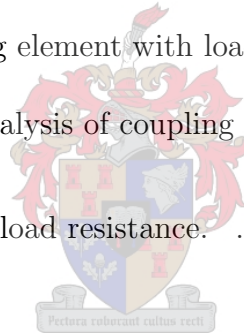
# List of Figures

2.1	Equivalent circuit of $n$ coupled cavities. . . . .	5
2.2	Coupled resonator two port network: Definition of currents and voltages. .	6
2.3	Coupled resonator two port network with termination impedances. . . . .	8
3.1	Two port definition of currents and voltages to be used with Z-parameters.	16
4.1	A single coaxial resonator post and cavity. . . . .	20
4.2	Cross section of a coaxial resonator cavity. . . . .	20
4.3	Cross section and circuit representation of a single coaxial resonator. . . .	21
4.4	Equivalent circuit of two magnetically coupled resonators. . . . .	23
4.5	Equivalent circuit of two electrically coupled resonators. . . . .	24
4.6	General distribution of E-fields and H-fields in a coaxial resonator cavity. .	24
4.7	Two magnetically coupled coaxial resonator cavities. . . . .	25
4.8	Structure used for the Q-factor simulations. . . . .	26
4.9	Setup to compare the negative coupling of two sizes of filter. . . . .	26
4.10	Coupling coefficient versus aperture height for different coaxial resonators.	27
4.11	The effect of the coaxial resonator post radius on the coupling coefficient, and electric and magnetic energy at the aperture. . . . .	30
4.12	The effect of the aperture height on the coupling coefficient, and electric and magnetic energy at the aperture. . . . .	30
4.13	The effect of the length of the coaxial resonator post on the coupling coef- ficient, and electric and magnetic energy at the aperture. . . . .	31

4.14	Coaxial resonators coupled by a single-pole evanescent mode filter. . . . .	32
4.15	Dimensions of the evanescent mode waveguide. . . . .	32
4.16	Construction of a bandpass filter with evanescent mode elements. . . . .	33
4.17	A single-pole bandpass filter constructed from evanescent mode elements. . . . .	33
4.18	A single-pole evanescent mode bandpass filter with J-inverters. . . . .	34
4.19	Even and odd mode admittances of the single-pole evanescent mode filter. . . . .	34
4.20	An ideal J-inverter with end capacitors. . . . .	35
4.21	Parameters used in the evanescent mode coupling element experiments. . . . .	36
4.22	Coupling coefficient and frequency of mode 1 as a function of $L_p$ . . . . .	37
4.23	Coupling coefficient and frequency of mode 1 as a function of $h$ . . . . .	38
4.24	Coupling coefficient and frequency of mode 1 as a function of $L_e$ . . . . .	38
4.25	Coupling coefficient and frequency of mode 1 as a function of $r$ . . . . .	38
4.26	Two coaxial resonators coupled by a capacitive probe. . . . .	39
4.27	Parameters used in the capacitive probe coupling experiments. . . . .	39
4.28	Coupling coefficient as a function of capacitive probe parameters. . . . .	40
4.29	Coupled resonator filter in a $50 \Omega$ environment. . . . .	41
4.30	A single coaxial resonator cavity with tapped feed line. . . . .	41
4.31	Inductance in the feed structure. . . . .	42
4.32	External Q-factor versus feed tap position. . . . .	44
4.33	Single cavity resonator and feed. . . . .	45
4.34	Comparison of $S_{11}$ phase of a single coaxial resonator with tapped feed, an ideal parallel resonator and an ideal series resonator. . . . .	47
4.35	Model of a single parallel $LC$ resonator with feed inductance $L_s$ . . . . .	47
4.36	Transformed model of a single parallel resonator with feed inductance. . . . .	49
5.1	Equivalent circuit of $n$ coupled cavities. . . . .	53

5.2	Phase response of a short-circuited set of two coupled series resonators. . .	55
5.3	Phase response of a open-circuited set of two coupled parallel resonators. . .	55
5.4	Phase response of 3 parallel coupled resonators, terminated in an open circuit, with and without a complex feed structure. . . . .	56
5.5	Equivalent circuit representation of $n$ cascaded coupled resonators. . . . .	57
5.6	Modified equivalent circuit including an unknown length of transmission line to account for the shift in the short circuit reference plane. . . . .	59
5.7	Circuits corresponding to the (a) low pass, (b) bandpass and (c) inverter-coupled resonator prototypes. . . . .	63
5.8	Prototype filter model of $n$ coupled resonators. . . . .	65
5.9	Equivalent circuit of $n$ coupled parallel resonators. . . . .	68
5.10	Equivalent circuit as a simplified two port network. . . . .	69
5.11	Model of tapped feed structure. . . . .	72
5.12	Microwave Office parameter extraction model. . . . .	76
6.1	Coaxial resonator cavity dimensions. . . . .	78
6.2	Resonator side view with tapped feed position. . . . .	79
6.3	Prototype filter one. . . . .	80
6.4	Filter 1: Cavities 1 and 3. . . . .	81
6.5	Filter 1: Couplings 1-2 and 3-4. . . . .	81
6.6	Filter 1: Cavities 2 and 4. . . . .	82
6.7	Filter 1: Tuning posts. . . . .	82
6.8	Filter 1: Measurements with different transmission zero frequencies, $f_z$ . . .	83
6.9	Filter 1: Wide band measurement. . . . .	84
6.10	Filter 1: Spurious response location with respect to different transmission zero frequencies, $f_z$ . . . . .	84
6.11	Prototype filter two. . . . .	85

6.12	Filter 2: Cavities 1 and 3 with capacitive coupling probe. . . . .	86
6.13	Filter 2: Cavities 1 and 3 with magnetic coupling irises. . . . .	86
6.14	Filter 2: Cavities 1 and 2. . . . .	87
6.15	Filter 2: Resonators 2 and 4, with filter tuning posts. . . . .	87
6.16	Filter 2: Narrow band measurement. . . . .	88
6.17	Traveling microscope measurements of capacitive probe. . . . .	88
6.18	Filter 2: Wide band measurement. . . . .	89
A.1	Systematic scaling of the coupling matrix equivalent circuit. . . . .	94
B.1	Inverter definitions. . . . .	95
B.2	Circuit representation of magnetic coupling. . . . .	96
B.3	Ideal magnetic coupling element with load impedance. . . . .	96
B.4	Even and odd mode analysis of coupling element. . . . .	97
C.1	Two port network and load resistance. . . . .	99



# Chapter 1

## Introduction

### 1.1 Historical Perspective

The past 60 years have seen the coupled resonator cavity filter develop from a little-known technology used by only a few experts, to a well-researched subject used by high frequency engineers worldwide. The history of coupled resonator cavity filters can be traced back to 1948, when Ragan first described the implementation of a filter consisting of direct-coupled waveguide cavities separated by thin inductive irises [1]. Although the synthesis and implementation still contained some obstacles, this first step led to an active interest in the field, with major contributions, among others, by S.B. Cohn, R. Levy and L. Young.

The result of this activity was, firstly, the expansion of the small aperture theory first presented by Bethe in 1944 [2], to enable accurate prediction of coupling values. The main contributors in this field were Cohn, who developed an electrolytic tank to measure the polarisability of small apertures of arbitrary shape [3, 4], McDonald who introduced a method for evaluating the coupling between resonant cavities coupled by a small aperture in a wall of arbitrary thickness [5], and Levy who expanded the theory to include large apertures [6].

Secondly, the research led to the establishment of rigorous and flexible synthesis techniques. In 1971, Atia and Williams presented a method which synthesises a general coupling matrix from desired transfer function characteristics, through the use of admittance parameters [7]. Today, filter synthesis with the aid of a coupling matrix forms a key part in most microwave filter designs.

## 1.2 Project Background

Narrow band filters are key components in many systems, especially in the field of telecommunication. In the base station of an antenna, a diplexer employs two side by side narrow band filters to isolate the transmit (Tx) and receive (Rx) signals. Optimal utilisation of the frequency spectrum requires close proximity of the Tx and Rx channels. As the transmitted power levels can be as much as a million times higher than the received power, it is important to achieve good isolation between the two channels, so as to prevent interference and damage to sensitive receiver equipment. Such high isolation requires sharp cutoff in the frequency band between the Tx and Rx channels. However, on the outside of the two channels, rejection requirements tend to be less stringent, thereby creating the need for an asymmetrical transfer function.

In recent years, synthesis techniques have been expanded to enable the creation of coupling matrices corresponding to such asymmetrical transfer functions, making it possible to obtain the required Tx-Rx isolation with filters of order lower than that of their symmetrical counterparts. The resulting coupling matrices contain both positive and negative coupling values, in contrast with the all-positive coupling values of symmetrical transfer functions with infinite transmission zeros. In a coupled resonator filter, there exists various ways in which to establish these positive and negative coupling values, ranging from classic iris coupling to evanescent mode- and capacitive probe coupling. As existing literature does not contain a comprehensive discussion of the characteristics of negative coupling mechanisms, one of the aims of this thesis is to study the applications and restrictions of different negative coupling realisations.

## 1.3 About the Thesis

The topic of this thesis is the investigation of the issues related to the realisation of an asymmetric filter characteristic in coaxial coupled resonator technology. The natural starting point of a microwave filter design, is to study the fundamental coupled resonator theory of Atia and Williams [7], as this forms the basis of most modern filter synthesis techniques. Accordingly, this is the topic of Chapter 2. In order to synthesise a coupling matrix corresponding to an asymmetric transfer function specification, the theory presented by Cameron [8] is utilised. This is outlined in Chapter 3. After obtaining the coupling matrix, the next step is to realise these values in a coaxial coupled resonator structure. Chapter 4 covers the many issues related to the physical realisation of the coupling matrix. Following the initial construction of the filter, be it in electromagnetic simulation software or the workshop, it is necessary to extract the resonant frequencies

and coupling values established by the individual elements, to enable the tuning of elements for optimal filter performance. Many parameter extraction techniques have been presented over the past two decades, some of which are summarised and evaluated in Chapter 5. Two fourth order asymmetrical filters were designed and built, which realise two different methods of negative coupling. In Chapter 6, these filters are compared in terms of their manufacturing ease and performance. Finally, the work completed in this thesis is evaluated in Chapter 7.





# Chapter 2

## Basic Theory of Narrow Band Coupled Resonator Filter Synthesis

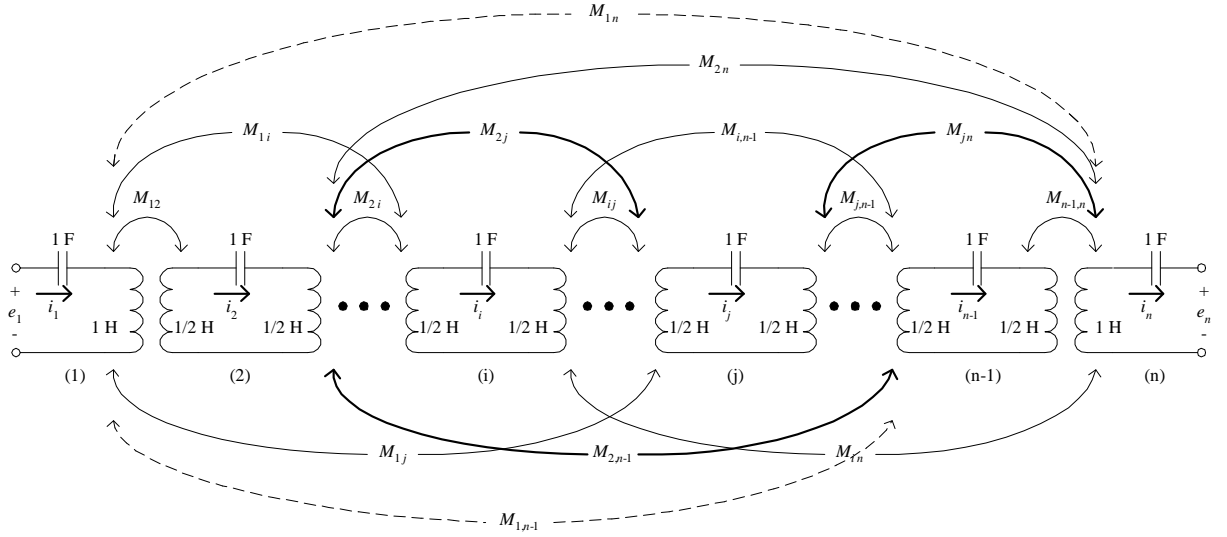
### 2.1 Introduction

One of the most elegant theories in high frequency engineering is the theory of narrow band coupled resonator filter synthesis, first presented by Atia and Williams in 1971 [7]. Through the application of network theory and linear algebra, it is possible to connect a required low pass transfer function with a low pass prototype circuit. The synthesis is based on the equation of two admittance matrices, one obtained from the equivalent circuit, and the other obtained from the required filter specifications. This chapter will outline this fundamental procedure, first approaching it from the viewpoint of the equivalent circuit in Section 2.2, then from the viewpoint of the filter specification in Section 2.3. The final result is a coupling matrix, which describes the required resonant frequencies and coupling values between resonators.

### 2.2 Manipulation of the General Equivalent Circuit

One way in which to construct a narrow band high frequency filter, is as a set of multiple-coupled, high-Q resonant cavities. When the frequency band of interest is narrow (ideally less than 10%), each cavity can be treated as a single resonator with multiple couplings to all other resonant cavities. By controlling the resonator frequencies and coupling values, it is possible to create a structure which behaves like a filter. The starting point for the synthesis procedure is therefore a circuit consisting of  $n$  multiple-coupled series resonators, shown in Fig. 2.1 [7, 9, 10].

Each cavity is tuned to a resonant frequency of  $\omega_0 = \frac{1}{\sqrt{LC}} = 1$  rad/s, and has a charac-


 Fig. 2.1. Equivalent circuit of  $n$  coupled cavities.

teristic impedance of  $Z_0 = \sqrt{\frac{L}{C}} = 1 \Omega$ . This means that the total loop capacitance and inductance equals 1 Farad and 1 Henry, respectively, which leads to s-plane impedances of  $Z_C = \frac{1}{s} \Omega$  and  $Z_L = s \Omega$ ,  $s = j\omega$ .

The narrow band approximation is implemented by assuming that the inductive coupling does not vary with frequency.

$$j\omega M \simeq j\omega_0 M \simeq jM \quad (2.1)$$

Analysis of the general circuit yields an  $n \times n$  impedance matrix. For the sake of simplicity, a new frequency variable  $S = s + \frac{1}{s}$  is created.

$$\begin{bmatrix} e_1 \\ 0 \\ 0 \\ \cdot \\ \cdot \\ 0 \\ -e_n \end{bmatrix} = \begin{bmatrix} S & -jM_{12} & -jM_{13} & \cdots & \cdot & -jM_{1n} \\ -jM_{12} & S & -jM_{23} & \cdots & \cdot & -jM_{2n} \\ -jM_{13} & -jM_{23} & S & \cdots & \cdot & \cdot \\ \cdot & \cdot & \cdot & \cdots & \cdot & \cdot \\ \cdot & \cdot & \cdot & \cdots & \cdot & \cdot \\ \cdot & \cdot & \cdot & \cdots & S & -jM_{n-1,n} \\ -jM_{1n} & \cdot & \cdot & \cdots & -jM_{n-1,n} & S \end{bmatrix} \cdot \begin{bmatrix} i_1 \\ i_2 \\ i_3 \\ \cdot \\ \cdot \\ i_{n-1} \\ i_n \end{bmatrix} \quad (2.2)$$

Therefore,

$$\begin{aligned} \mathbf{E} &= \mathbf{Z} \cdot \mathbf{I} \\ &= (S\mathcal{I} - j\mathbf{M}) \cdot \mathbf{I} \end{aligned} \quad (2.3)$$

with  $\mathcal{I}$  the identity matrix.

To determine the coupling matrix  $\mathbf{M}$  in terms of a low pass transfer function,  $S$  is replaced by  $s = j\omega$ . Because  $\mathbf{M}$  remains unchanged in this step, the coupling matrix is effectively

made completely frequency-invariant. Next, the aim is to write the two port Y-parameters of the equivalent circuit in terms of the Z-matrix. For this purpose, the currents are defined as inward, as illustrated in Fig. 2.2.

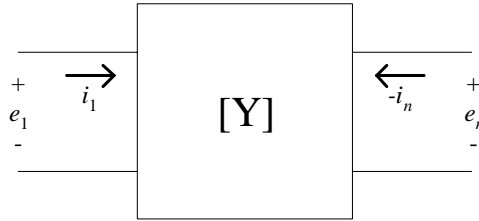


Fig. 2.2. Coupled resonator two port network: Definition of currents and voltages.

The Y-parameters, in terms of the two port currents and voltages, are given by eqn. 2.4.

$$\begin{aligned}
 y_{11} &= \left. \frac{i_1}{e_1} \right|_{e_n=0} \\
 y_{12} &= \left. \frac{i_1}{e_n} \right|_{e_1=0} \\
 y_{21} &= \left. -\frac{i_n}{e_1} \right|_{e_n=0} \\
 y_{22} &= \left. -\frac{i_n}{e_n} \right|_{e_1=0}
 \end{aligned} \tag{2.4}$$

By multiplying both sides of eqn. 2.3 with the inverse of  $\mathbf{Z}$  and carrying out the scalar product, the port currents can be expressed as

$$\begin{aligned}
 i_1 &= \mathbf{Z}_{11}^{-1}(e_1) + \mathbf{Z}_{1n}^{-1}(-e_n) \\
 i_n &= \mathbf{Z}_{n1}^{-1}(e_1) + \mathbf{Z}_{nn}^{-1}(-e_n)
 \end{aligned} \tag{2.5}$$

where  $\mathbf{Z}_{mn}^{-1}$  refers to the  $(m, n)^{\text{th}}$  element of the inverse of the impedance matrix.

Substitution of eqn. 2.4 into eqn. 2.5 yields the two port Y-parameters in terms of the Z-matrix.

$$\begin{aligned}
 y_{11} &= \mathbf{Z}_{11}^{-1} \\
 y_{12} &= -\mathbf{Z}_{1n}^{-1} \\
 y_{21} &= -\mathbf{Z}_{n1}^{-1} \\
 y_{22} &= \mathbf{Z}_{nn}^{-1}
 \end{aligned} \tag{2.6}$$

In terms of eqn. 2.3, this becomes

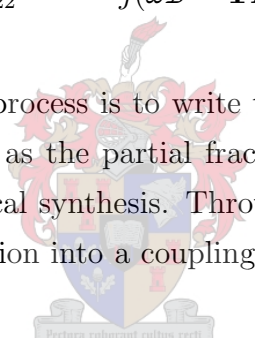
$$\begin{aligned} y_{21} &= -(s\mathcal{I} - j\mathbf{M})_{n1}^{-1} \\ &= j(\omega\mathcal{I} - \mathbf{M})_{n1}^{-1} \end{aligned} \quad (2.7)$$

$$\begin{aligned} y_{22} &= (s\mathcal{I} - j\mathbf{M})_{nn}^{-1} \\ &= -j(\omega\mathcal{I} - \mathbf{M})_{nn}^{-1} \end{aligned} \quad (2.8)$$

If one assumes that the network is symmetric, the matrix  $\mathbf{M}$  has real eigenvalues and is real and symmetric about its diagonal. Therefore, a matrix  $\mathbf{T}$  exists which satisfies the equation  $\mathbf{M} = \mathbf{T}\mathbf{\Lambda}\mathbf{T}^t$ . The eigenvalues of  $\mathbf{M}$  are given by  $\mathbf{\Lambda} = \text{diag}(\lambda_1 \lambda_2 \cdots \lambda_n)$ , and  $\mathbf{T}\mathbf{T}^t = \mathbf{T}^t\mathbf{T} = \mathcal{I}$ , as explained in [11, p.443–448]. The  $k^{\text{th}}$  column of  $\mathbf{T}$  is the eigenvector corresponding to the  $k^{\text{th}}$  eigenvalue  $\lambda_k$ . The Y-parameters can now be written as

$$\begin{aligned} y_{21} &= j(\omega\mathcal{I} - \mathbf{T}\mathbf{\Lambda}\mathbf{T}^t)_{n1}^{-1} \\ y_{22} &= -j(\omega\mathcal{I} - \mathbf{T}\mathbf{\Lambda}\mathbf{T}^t)_{nn}^{-1} \end{aligned} \quad (2.9)$$

The next step in the synthesis process is to write the Y-parameters as partial fractions. This is the crux of the matter, as the partial fraction expansion is where the practical specification meets the theoretical synthesis. Through this process, one is able to transform the required transfer function into a coupling matrix. Consider the inverse term in eqn. 2.9.



$$\begin{aligned} (\omega\mathcal{I} - \mathbf{T}\mathbf{\Lambda}\mathbf{T}^t)^{-1} &= (\omega\mathbf{T}\mathcal{I}\mathbf{T}^t - \mathbf{T}\mathbf{\Lambda}\mathbf{T}^t)^{-1} \\ &= (\mathbf{T}(\omega\mathcal{I} - \mathbf{\Lambda})\mathbf{T}^t)^{-1} \\ &= (\mathbf{T}^t)^{-1}(\omega\mathcal{I} - \mathbf{\Lambda})^{-1}\mathbf{T}^{-1} \\ &= \mathbf{T}(\omega\mathcal{I} - \mathbf{\Lambda})^{-1}\mathbf{T}^t \\ &= \mathbf{T} \text{diag}\left(\frac{1}{\omega - \lambda_1}, \frac{1}{\omega - \lambda_2}, \dots, \frac{1}{\omega - \lambda_n}\right)\mathbf{T}^t \\ &= \begin{bmatrix} T_{11} & T_{12} & \cdots & T_{1n} \\ T_{21} & \cdot & \cdots & \cdot \\ \vdots & & & \vdots \\ T_{n1} & \cdot & \cdots & T_{nn} \end{bmatrix} \begin{bmatrix} \frac{T_{11}}{\omega - \lambda_1} & \frac{T_{21}}{\omega - \lambda_1} & \cdots & \frac{T_{n1}}{\omega - \lambda_1} \\ \frac{T_{12}}{\omega - \lambda_2} & \frac{T_{22}}{\omega - \lambda_2} & \cdots & \frac{T_{n2}}{\omega - \lambda_2} \\ \vdots & & & \vdots \\ \frac{T_{1n}}{\omega - \lambda_n} & \frac{T_{2n}}{\omega - \lambda_n} & \cdots & \frac{T_{nn}}{\omega - \lambda_n} \end{bmatrix} \end{aligned} \quad (2.10)$$

By taking the scalar product of the two matrices in eqn. 2.10, it is clear that the  $(i, j)^{\text{th}}$  component of the inverse term can be written as

$$(\omega\mathcal{I} - \mathbf{T}\mathbf{\Lambda}\mathbf{T}^t)_{ij}^{-1} = \sum_{k=1}^n \frac{T_{ik}T_{jk}}{\omega - \lambda_k} \quad (2.11)$$

Accordingly, the expressions for the Y-parameters become

$$\begin{aligned} y_{21} &= j \sum_{k=1}^n \frac{T_{1k} T_{nk}}{\omega - \lambda_k} \\ y_{22} &= -j \sum_{k=1}^n \frac{(T_{nk})^2}{\omega - \lambda_k} \end{aligned} \quad (2.12)$$

However, the partial fraction expansions of eqn. 2.12 refer to the internal network of the filter and does not take the termination impedances into account. In order to do this, the two port network of Fig. 2.2 is expanded to include two ideal transformers and a normalised source and load impedance of  $1 \Omega$ , as shown in Fig. 2.3.

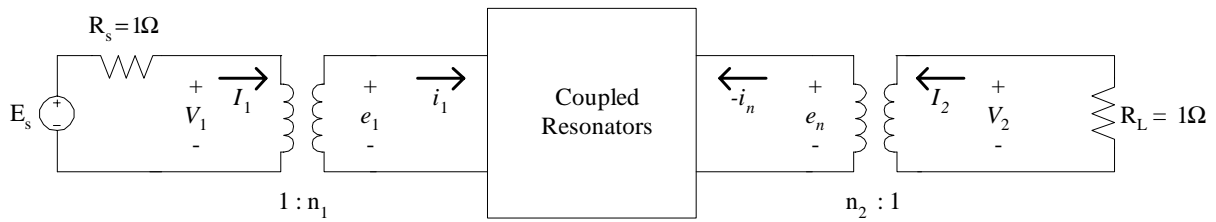


Fig. 2.3. Coupled resonator two port network with termination impedances.

A new set of Y-parameters will now be obtained in terms of the previous set, and is defined as

$$\begin{bmatrix} I_1 \\ I_2 \end{bmatrix} = \begin{bmatrix} y_{11}' & y_{12}' \\ y_{21}' & y_{22}' \end{bmatrix} \begin{bmatrix} V_1 \\ V_2 \end{bmatrix} \quad (2.13)$$

By taking the transformer ratios into account, the following holds:

$$\begin{aligned} \begin{bmatrix} I_1 \\ I_2 \end{bmatrix} &= \begin{bmatrix} n_1 & 0 \\ 0 & n_2 \end{bmatrix} \begin{bmatrix} i_1 \\ -i_n \end{bmatrix} \\ &= \begin{bmatrix} n_1 & 0 \\ 0 & n_2 \end{bmatrix} \begin{bmatrix} y_{11} & y_{12} \\ y_{21} & y_{22} \end{bmatrix} \begin{bmatrix} e_1 \\ e_n \end{bmatrix} \\ &= \begin{bmatrix} n_1 & 0 \\ 0 & n_2 \end{bmatrix} \begin{bmatrix} y_{11} & y_{12} \\ y_{21} & y_{22} \end{bmatrix} \begin{bmatrix} n_1 & 0 \\ 0 & n_2 \end{bmatrix} \begin{bmatrix} V_1 \\ V_2 \end{bmatrix} \\ &= \begin{bmatrix} n_1^2 y_{11} & n_1 n_2 y_{12} \\ n_1 n_2 y_{21} & n_2^2 y_{22} \end{bmatrix} \begin{bmatrix} V_1 \\ V_2 \end{bmatrix} \end{aligned} \quad (2.14)$$

The new parameters are therefore given by

$$\begin{aligned}
 y_{21}' &= n_1 n_2 y_{21} \\
 &= j \sum_{k=1}^n \frac{n_1 n_2 T_{1k} T_{nk}}{\omega - \lambda_k} \\
 &= - \sum_{k=1}^n \frac{n_1 n_2 T_{1k} T_{nk}}{s - j\lambda_k}
 \end{aligned} \tag{2.15}$$

and

$$\begin{aligned}
 y_{22}' &= n_2^2 y_{22} \\
 &= -j \sum_{k=1}^n \frac{n_2^2 (T_{nk})^2}{\omega - \lambda_k} \\
 &= \sum_{k=1}^n \frac{n_2^2 (T_{nk})^2}{s - j\lambda_k}
 \end{aligned} \tag{2.16}$$

At this point in the synthesis procedure, it is possible to equate the Y-parameters of the equivalent model with those obtained from the practical specification.

## 2.3 Equation of Y-parameters

From the theory on passive, lossless two port devices,  $y_{21,spec}$  and  $y_{22,spec}$  can be constructed from the original filter specification as

$$y_{21,spec} = - \sum_{k=1}^n \frac{K_{21,k}}{s - p_k} \tag{2.17}$$

and

$$y_{22,spec} = \sum_{k=1}^n \frac{K_{22,k}}{s - p_k} \tag{2.18}$$

The equation of  $y_{22}'$  and  $y_{22,spec}$  implies that

$$\begin{aligned}
 K_{22,k} &= (T_{nk})^2 n_2^2 \\
 p_k &= j\lambda_k
 \end{aligned} \tag{2.19}$$

From the definition  $\mathbf{T}\mathbf{T}^t = \mathcal{I}$ ,

$$\sum_{k=1}^n (T_{nk})^2 = 1$$

Therefore,

$$\begin{aligned}
 \sum_{k=1}^n K_{22,k} &= n_2^2 \sum_{k=1}^n (T_{nk})^2 \\
 &= n_2^2
 \end{aligned} \tag{2.20}$$

Substitution of eqn. 2.20 into eqn. 2.19 makes it possible to solve the  $n^{\text{th}}$  row of the T-matrix in terms of the known residues  $K_{22,k}$ .

$$T_{nk} = \sqrt{\frac{K_{22,k}}{\sum_{k=1}^n K_{22,k}}} \quad (2.21)$$

Similarly, one can equate eqn. 2.15 and eqn. 2.17. It follows that

$$\begin{aligned} n_1 n_2 T_{1k} T_{nk} &= K_{21,k} \\ \Rightarrow T_{1k} &= \frac{K_{21,k}}{n_1 n_2 T_{nk}} \end{aligned} \quad (2.22)$$

with

$$n_1^2 = \sum_{k=1}^n \frac{(K_{21,k})^2}{K_{22,k}} \quad (2.23)$$

At this stage, the first and last rows of the T-matrix, together with the transformer ratios are known in terms of the residues  $K_{21}$  and  $K_{22}$ .

To compose the remaining rows of the T-matrix, the Gram-Schmidt orthonormalisation procedure can be applied to  $T_1$  and  $T_n$ . In linear algebra, the Gram-Schmidt process is a method which orthogonalises a set of vectors in an inner product space. Orthogonalisation in this context means to start with a set of linearly independent vectors, and find another set of vectors which are mutually orthogonal and generate the same subspace as the initial set. To obtain an orthonormal set of vectors, one has to divide each vector by its norm. As an alternative to the Gram-Schmidt procedure, [12] recommends the Householder transformation, which apparently provides greater numerical stability. It has however not been verified in this thesis.

With  $\mathbf{\Lambda} = \text{diag}(\lambda_1, \lambda_2, \dots, \lambda_n)$  obtained from the poles  $p_k$ , the coupling matrix can now be constructed as

$$\mathbf{M} = \mathbf{T}\mathbf{\Lambda}\mathbf{T}^t \quad (2.24)$$

Many texts construct the impedance matrix as  $(S\mathcal{I} + j\mathbf{M})$ . This is then taken into account by defining the coupling matrix as  $-\mathbf{T}\mathbf{\Lambda}\mathbf{T}^t$ .

## 2.4 Conclusion

This chapter has outlined the procedure which connects the coupled resonator model of a narrow band filter to the specification of the desired transfer function. The result is a coupling matrix which describes the coupling magnitudes between cavities, as well as their individual resonant frequencies.

# Chapter 3

## General Coupling Matrix Synthesis Methods for Chebyshev Filtering Functions

### 3.1 Introduction

A microwave filter using the Chebyshev class of transfer function has long been one of the most popular filters in the field. Some of its features include equiripple amplitude inside the pass band and sharp cutoff at the edge of the pass band, together with good compromise between pass band signal degradation and out of band rejection. Recently, it has gained even more use in the ability to prescribe certain symmetrical or asymmetrical transmission zeros to improve close to band rejection slopes.

Especially in the field of diplexer design, filter transfer function requirements tend to be asymmetrical. Transmit/Receive (Tx/Rx) channels lie very close together and high rejection is required between the Tx and Rx band to prevent interference and damage to equipment. However, on the outer sides of the Tx and Rx channels, the rejection specifications tend to be less severe. These asymmetrical requirements are best realised by an asymmetrical transfer function. Using a symmetrical transfer function to reach the required rejection levels would require a higher degree of filter, thereby increasing the insertion loss, in-band distortion and mass [8]. The difference in degree between the symmetrical and asymmetrical filter characteristic is determined by the amount of rejection required, with sharper cutoff requiring a higher degree of symmetrical filter.

The design of asymmetrical filters remained a problem for many years, until Cameron [8] presented a new algorithm in 1999. This chapter will discuss Cameron's method of creating the transfer polynomials and coupling matrix from an asymmetrical Chebyshev specification.



## 3.2 Transfer and Reflection Polynomial Synthesis

By using the notation first implemented by Darlington in 1939 [13], the reflection coefficient and transfer function of any lossless two port network composed of  $n$  interconnected resonator cavities (see Fig. 2.1), is expressed as the ratio of two  $n^{\text{th}}$  degree polynomials.

$$S_{11}(s) = \frac{\pm F_n(s)}{E_n(s)} \quad (3.1)$$

$$S_{21}(s) = \frac{P_n(s)}{\epsilon E_n(s)} \quad (3.2)$$

For a Chebyshev transfer function,  $\epsilon$  is a constant normalising  $S_{21}$  to the chosen equiripple level at  $\omega = 1$  rad/s.

The synthesis procedure starts with the specification of a normalised transfer function with transmission zeros  $s_k$  in the complex s-plane. The aim is therefore to determine  $E_n(s)$ ,  $P_n(s)$  and  $F_n(s)$  in terms of these transmission zeros. Due to the fact that, for a coupled resonator structure, it is not possible to have direct coupling between the input and output ports, the transfer function may have a maximum of  $n - 2$  finite transmission zeros. The remaining transmission zeros are placed at infinity. Additionally, in order for  $P_n(\omega)$  and  $F_n(\omega)$  to have real coefficients, the prescribed transmission zeros have to be symmetrical about the imaginary axis of the s-plane [8].

With transmission zeros placed on the imaginary axis, the numerator polynomial of  $S_{21}$  can be written as

$$P_n(\omega) = \prod_{k=1}^n (\omega - \omega_k) \quad (3.3)$$

where  $s_k = j\omega_k$  represents the  $k^{\text{th}}$  transmission zero.

The Feldtkeller equation is defined as [14, p.196–204]

$$E(s)E(-s) = F(s)F(-s) + \frac{1}{\epsilon^2}P(s)P(-s) \quad (3.4)$$

By applying the conservation of energy formula for a lossless two port network to eqns. 3.1 and 3.2 and using eqn. 3.4,

$$\begin{aligned} |S_{11}(\omega)|^2 + |S_{21}(\omega)|^2 &= 1 \\ \frac{|F_n(\omega)|^2}{|E_n(\omega)|^2} + \frac{|P_n(\omega)|^2}{\epsilon^2|E_n(\omega)|^2} &= 1 \\ \frac{\epsilon^2|E_n(\omega)|^2}{|P_n(\omega)|^2} &= 1 + \frac{\epsilon^2|F_n(\omega)|^2}{|P_n(\omega)|^2} \end{aligned} \quad (3.5)$$

Therefore,

$$\begin{aligned}
 |S_{21}(\omega)|^2 &= \frac{1}{\frac{\epsilon^2 |E_n(\omega)|^2}{|P_n(\omega)|^2}} \\
 &= \frac{1}{1 + \epsilon^2 C_n^2(\omega)} \\
 &= \frac{1}{(1 + j\epsilon C_n(\omega))(1 - j\epsilon C_n(\omega))}
 \end{aligned} \tag{3.6}$$

with

$$C_n(\omega) = \frac{F_n(\omega)}{P_n(\omega)} \tag{3.7}$$

$C_n(\omega)$  is defined as the filtering function on degree  $n$  with the general Chebyshev characteristic

$$C_n(\omega) = \cosh \left[ \sum_{k=1}^n \cosh^{-1}(x_k) \right] \tag{3.8}$$

where

$$x_k = \frac{\omega - 1/\omega_k}{1 - \omega/\omega_k} \tag{3.9}$$

Substitution of the identity  $\cosh^{-1}(x) = \ln(x + \sqrt{x^2 - 1})$  into eqn. 3.8 yields

$$\begin{aligned}
 C_n(\omega) &= \cosh \left[ \sum_{k=1}^n \ln \left( x_k + \sqrt{x_k^2 - 1} \right) \right] \\
 &= \cosh \left[ \sum_{k=1}^n \ln(a_k + b_k) \right] \\
 &= \frac{1}{2} \left[ \exp \left( \sum_{k=1}^n \ln(a_k + b_k) \right) + \exp \left( - \sum_{k=1}^n \ln(a_k + b_k) \right) \right] \\
 &= \frac{1}{2} \left[ \prod_{k=1}^n (a_k + b_k) + \frac{1}{\prod_{k=1}^n (a_k + b_k)} \right]
 \end{aligned}$$

By multiplying the numerator and denominator of the second term by  $\prod(a_k - b_k)$ ,

$$\begin{aligned}
 C_n(\omega) &= \frac{1}{2} \left[ \prod_{k=1}^n (a_k + b_k) + \frac{\prod_{k=1}^n (a_k - b_k)}{\prod_{k=1}^n (a_k^2 - b_k^2)} \right] \\
 &= \frac{1}{2} \left[ \prod_{k=1}^n (a_k + b_k) + \prod_{k=1}^n (a_k - b_k) \right] \\
 &= \frac{1}{2} \left[ \prod_{k=1}^n \left( x_k + \sqrt{x_k^2 - 1} \right) + \prod_{k=1}^n \left( x_k - \sqrt{x_k^2 - 1} \right) \right]
 \end{aligned}$$

Substitution of eqn. 3.9 results in

$$\begin{aligned}
C_n(\omega) &= \frac{1}{2} \prod_{k=1}^n \left( \frac{\omega - 1/\omega_k}{1 - \omega/\omega_k} + \sqrt{\left( \frac{\omega - 1/\omega_k}{1 - \omega/\omega_k} \right)^2 - 1} \right) \\
&\quad + \frac{1}{2} \prod_{k=1}^n \left( \frac{\omega - 1/\omega_k}{1 - \omega/\omega_k} - \sqrt{\left( \frac{\omega - 1/\omega_k}{1 - \omega/\omega_k} \right)^2 - 1} \right) \\
&= \frac{1}{2} \left[ \frac{\prod_{k=1}^n (c_k + d_k) + \prod_{k=1}^n (c_k - d_k)}{\prod_{k=1}^n \left( 1 - \frac{\omega}{\omega_k} \right)} \right] \tag{3.10}
\end{aligned}$$

with

$$c_k = \omega - \frac{1}{\omega_k} \tag{3.11}$$

and

$$\begin{aligned}
d_k &= \sqrt{(\omega^2 - 1)(1 - 1/\omega_k^2)} \\
&= \omega' \sqrt{1 - 1/\omega_k^2} \tag{3.12}
\end{aligned}$$

The aim of the above manipulation is to implement a recursive technique with which one can determine  $F_n(\omega)$  from the specified asymmetrical transmission zeros. Accordingly, eqn. 3.10 can be rewritten in the following way:

$$\text{Num}\{C_n(\omega)\} = F_n(\omega) = \frac{1}{2} \left[ G_n(\omega) + G_n'(\omega) \right] \tag{3.13}$$

with

$$G_n(\omega) = \prod_{k=1}^n (c_k + d_k) = \prod_{k=1}^n \left[ \left( \omega - \frac{1}{\omega_k} \right) + \omega' \sqrt{1 - \frac{1}{\omega_k^2}} \right] \tag{3.14}$$

and

$$G_n'(\omega) = \prod_{k=1}^n (c_k - d_k) = \prod_{k=1}^n \left[ \left( \omega - \frac{1}{\omega_k} \right) - \omega' \sqrt{1 - \frac{1}{\omega_k^2}} \right] \tag{3.15}$$

Further, in  $G_n$  one can group all the terms in  $\omega$  and  $\omega'$  as  $U_n(\omega)$  and  $V_n(\omega)$ , respectively.

$$G_n(\omega) = U_n(\omega) + V_n(\omega) \tag{3.16}$$

To construct  $G_n(\omega)$  in a systematic way, the addition of each product in eqn. 3.14 will be followed by the regrouping of terms in  $\omega$  and  $\omega'$ . The recursive cycle is begun with the first prescribed transmission zero.

$$\begin{aligned}
G_1(\omega) &= c_1 + d_1 \\
&= \left( \omega - \frac{1}{\omega_1} \right) + \omega' \sqrt{1 - \frac{1}{\omega_1^2}} \\
&= U_1(\omega) + V_1(\omega)
\end{aligned}$$

Next, the terms corresponding to the second prescribed transmission zero are multiplied with the  $G_1$  and re-ordered.

$$\begin{aligned}
 G_2(\omega) &= G_1(\omega) [c_2 + d_2] \\
 &= \left[ U_1(\omega) + V_1(\omega) \right] \left[ \omega - \frac{1}{\omega_2} + \omega' \sqrt{1 - \frac{1}{\omega_2^2}} \right] \\
 &= \left( \omega U_1 - \frac{1}{\omega_2} U_1 + V_1 \omega' \sqrt{1 - \frac{1}{\omega_2^2}} \right) + \left( \omega V_1 - \frac{1}{\omega_2} V_1 + U_1 \omega' \sqrt{1 - \frac{1}{\omega_2^2}} \right) \\
 &= U_2(\omega) + V_2(\omega)
 \end{aligned}$$

$G_n(\omega)$  can be constructed by continuing the process for all of the remaining transmission zeros, including those at infinity. By then repeating the process for  $G'_n(\omega)$ , it can be written as

$$G'_n(\omega) = U'_n(\omega) + V'_n(\omega) \quad (3.17)$$

Due to the sign difference between the definitions of  $G_n(\omega)$  and  $G'_n(\omega)$  in eqns. 3.14 and 3.15,  $U_n(\omega) = U'_n(\omega)$  and  $V_n(\omega) = -V'_n(\omega)$ . Substitution of this result into eqn. 3.13, leads to an expression for  $F_n(\omega)$ .

$$\begin{aligned}
 F_n(\omega) &= \frac{1}{2} [G_n(\omega) + G'_n(\omega)] \\
 &= \frac{1}{2} [U_n(\omega) + V_n(\omega) + U'_n(\omega) + V'_n(\omega)] \\
 &= U_n(\omega)
 \end{aligned} \quad (3.18)$$

At this point,  $P_n(\omega)$  and  $F_n(\omega)$  have been determined, which leaves the determination of the normalisation constant  $\epsilon$  and  $E_n(\omega)$ . To find an expression for  $\epsilon$ , again consider the equation for conservation of energy in a lossless two port network.

$$\begin{aligned}
 |S_{21}(\omega)^2| &= 1 - |S_{11}(\omega)^2| \\
 &= 1 - 10^{-\text{RL}/10} \Big|_{\omega=\pm 1} \\
 \Rightarrow \frac{|P_n(1)|^2}{\epsilon^2 |E_n(1)|^2} &= \frac{10^{\text{RL}/10} - 1}{10^{\text{RL}/10}} \\
 \Rightarrow \epsilon &= \sqrt{\frac{10^{\text{RL}/10}}{10^{\text{RL}/10} - 1} \frac{|P_n(1)|^2}{|E_n(1)|^2}} \\
 &= \frac{1}{\sqrt{10^{\text{RL}/10} - 1}} |P_n(1)| \sqrt{\frac{1}{|S_{11}(1)|^2} \frac{1}{|E_n(1)|^2}} \\
 &= \frac{1}{\sqrt{10^{\text{RL}/10} - 1}} \frac{|P_n(\omega)|}{|F_n(\omega)|} \Big|_{\omega=1}
 \end{aligned} \quad (3.19)$$

Substitution of  $\epsilon$ ,  $F_n(\omega)$  and  $P_n(\omega)$  into the Feldtkeller equation now allows one to calculate  $E_n(\omega)^2$ . It is important to use normalised polynomials (highest order coefficient equal to one) in eqn. 3.4 and 3.19, as it ensures that  $E_n(\omega)^2$  is a normalised polynomial.

To construct  $E_n(s)$  from  $E_n(\omega)^2$ , the roots of  $E_n(\omega)^2$  are multiplied by  $j$  to obtain the roots in  $s$ . The left half plane roots are then used to reconstruct  $E_n(s)$ , as  $E_n(s)$  is required to be a Hurwitz polynomial in practically realisable networks [14]. The roots of  $P_n(s)$  and  $F_n(s)$  are simply the roots of  $P_n(\omega)$  and  $F_n(\omega)$ , multiplied by  $j$ .

This completes the synthesis of the transfer and reflection polynomials in terms of the prescribed transmission zeros. The next step in the creation of the coupling matrix, is the determination of the rational polynomials for the short-circuit admittance parameters in terms of the transfer polynomials.

### 3.3 Synthesis of the Coupling Matrix

Through the manipulation of  $Z_{in}$ , it is possible to unite the transfer polynomials and admittance parameters. Fig. 3.1 shows a lossless two port network terminated in a load impedance  $R_L$ .

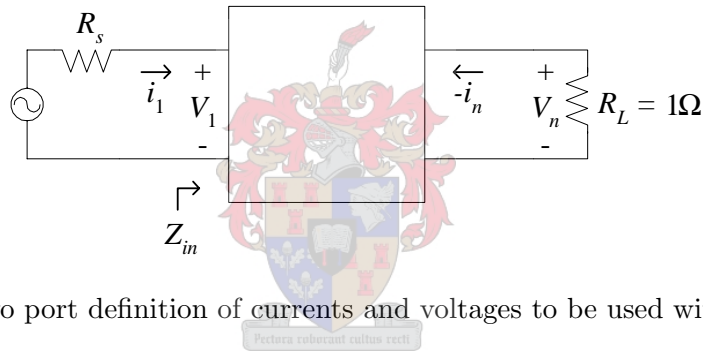


Fig. 3.1. Two port definition of currents and voltages to be used with Z-parameters.

In terms of its short- and open-circuit parameters, the driving point impedance of this network is given by eqn. 3.20 [15, p.346]. The derivation of this expression is completed in Appendix C.

$$Z_{in}(s) = \frac{z_{11} [1/y_{22} + R_L]}{z_{22} + R_L} = \frac{z_{11} [1/y_{22} + 1]}{z_{22} + 1} \quad (3.20)$$

for a load resistance of 1  $\Omega$ . For a source resistance of 1  $\Omega$ ,  $Z_{in}$  can be written in terms of  $S_{11}$  as

$$\begin{aligned} Z_{in}(s) &= \frac{1 + S_{11}(s)}{1 - S_{11}(s)} \\ &= \frac{E(s) \pm F(s)}{E(s) \mp F(s)} \\ &= \frac{m_1 + n_1}{m_2 + n_2} \end{aligned} \quad (3.21)$$

where  $m_1$ ,  $m_2$ ,  $n_1$ , and  $n_2$  are complex-even and complex-odd polynomials constructed from  $E(s)$  and  $F(s)$ . Let

$$\begin{aligned} \text{Num}\{Z_{in}(s)\} &= E(s) + F(s) \\ &= a_0 + a_1s + a_2s^2 + a_3s^3 + \dots \end{aligned} \quad (3.22)$$

Then,  $m_1$  and  $n_1$  are constructed as

$$m_1 = \operatorname{Re}\{a_0\} + j\operatorname{Im}\{a_1\}s + \operatorname{Re}\{a_2\}s^2 + \dots \quad (3.23)$$

and

$$n_1 = j\operatorname{Im}\{a_0\} + \operatorname{Re}\{a_1\}s + j\operatorname{Im}\{a_2\}s^2 + \dots \quad (3.24)$$

In the case of an even order filter, one factorises eqn. 3.21 as follows:

$$Z_{in}(s) = \frac{n_1 [m_1/n_1 + 1]}{m_2 + n_2} \quad (3.25)$$

Comparison of eqns. 3.20 and 3.25 leads to

$$y_{22} = \frac{n_1}{m_1} \quad (3.26)$$

For an even order filter, the order of  $m_1$  is one higher than the order of  $n_1$ . This makes  $y_{22}$  a proper rational function which can be expanded into partial fractions. Because  $y_{21}$  has the same transmission zeros as  $S_{21}$  [15, p.43–46], and the denominators of  $y_{21}$  and  $y_{22}$  are the same,  $y_{21}$  is constructed as

$$y_{21} = \frac{P_n(s)}{\epsilon m_1} \quad (3.27)$$

For a filter of odd order,  $n_1$  would have a higher order than  $m_1$ . Therefore, the driving point admittance is factorised as

$$Z_{in}(s) = \frac{m_1 [n_1/m_1 + 1]}{m_2 + n_2} \quad (3.28)$$

which leads to

$$y_{22} = \frac{m_1}{n_1} \quad (3.29)$$

and

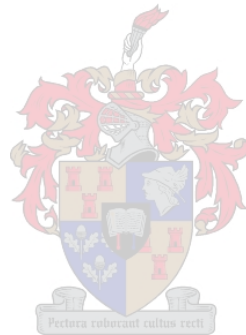
$$y_{21} = \frac{P_n(s)}{\epsilon n_1} \quad (3.30)$$

Finally, by expanding the above short-circuit parameters as partial fractions,  $y_{21}$  and  $y_{22}$  are equal to  $y_{21,spec}$  and  $y_{22,spec}$  of eqns. 2.17 and 2.18. The coupling matrix construction is completed by following the steps outlined in Section 2.3.

For the current realisation of an asymmetrical Chebyshev filtering characteristic, it is correct to use  $P(s)$  as the numerator of  $y_{21}$ , as this yields  $y_{21}$  residues which are real. However, due to the essentially non-physical narrow band approximation in the synthesis procedure,  $j\omega M \simeq j\omega_0 M \simeq jM$ , the coefficients of  $P(s)$  may indeed be imaginary. This is usually detected when  $y_{21}$  is expanded into partial fractions and found to have imaginary residues, which cannot be the case for a physical two port network. In order to correct this,  $P(s)$  in the numerator of  $y_{21}$  is then replaced by  $jP(s)$ . As this substitution does not alter the Feldtkeller equation, and therefore not  $E(s)$  or  $F(s)$ , it is mathematically acceptable.

### 3.4 Conclusion

A general method for the construction of the transfer and reflection polynomials for a Chebyshev filtering function, together with the short-circuit parameters needed for the generation of the coupling matrix, has been outlined in this chapter. For a filter of degree  $n$ , it is possible to prescribe certain transmission zeros in order to improve close-to-band rejection slopes. A maximum number of  $n - 2$  finite transmission zeros are allowed, with a symmetric distribution about the imaginary axis of the complex  $s$ -plane.

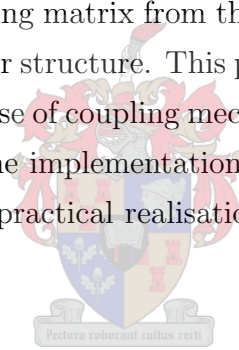


# Chapter 4

## Physical Realisation of the Coupling Matrix

### 4.1 Introduction

After having obtained the coupling matrix from the filter specification, the next step is to realise it with a coupled resonator structure. This part of the process involves the selection of a certain resonator type, the use of coupling mechanisms to provide the desired coupling value between resonators and the implementation of a feed structure. Some of the most important issues related to the practical realisation of the filter will be discussed in this chapter.



### 4.2 Resonant Cavities

When faced with the choice of which type of resonator to use for the structure, there are various options to consider. Although lumped element resonators are today being used at frequencies up to 18 GHz, their attainable unloaded Q-factors vary with frequency. At S-band, lumped element resonators can yield Q-factors of at most a few hundred [16], making it comparable with microstrip resonators. Lumped element resonators have the one major advantage of being smaller than distributed element resonators. However, if high power handling capabilities and low insertion loss are required, one has to make use of high Q (low loss) distributed resonators, like waveguide cavities or coaxial resonator cavities. For resonant frequencies in the low Gigahertz range, the large size of the waveguide cavities required for propagation above cutoff, makes it an unattractive choice. Coaxial resonators are smaller than waveguide resonators of the same frequency, and with unloaded Q-factors in the range of 3000 - 6000, this implementation is the resonator of choice for the current application. Fig. 4.1 shows an example of a coaxial resonator cavity used in the filter



realisation.

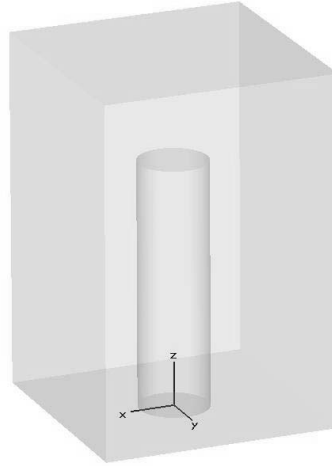


Fig. 4.1. A single coaxial resonator post and cavity.

According to Matthaei, Young and Jones [17, p.167], a coaxial line has the lowest amount of loss if  $\sqrt{\epsilon_r}Z_0 = 77 \Omega$ . Although the given graphs apply to lines with outside conductors of circular cross section, the assumption is still accurate for coaxial conductors of other shapes. For the chosen coaxial resonator realisation, the dielectric material is air. Therefore,  $\epsilon_r = 1$ , implying an optimal resonator characteristic impedance of  $77 \Omega$ .

Lin [18] used the complex potential function to work out the characteristic impedance of a polygonal line with  $N$  sides and a round inner coaxial conductor. For  $N = 4$ , the equation reduces to

$$Z_0 = 59.952 \left( \ln \left( \frac{b}{a} \right) + 0.06962 \right) \quad (4.1)$$

with  $b$  the length of one side of the square outside conductor and  $a$  the diameter of the inside conductor, as illustrated in Fig. 4.2. Substitution of  $Z_0 = 77 \Omega$  in eqn. 4.1 yields  $b/a = 3.369$ . The choice of which combination of  $b$  and  $a$  to use, is a subject discussed in Section 4.4.

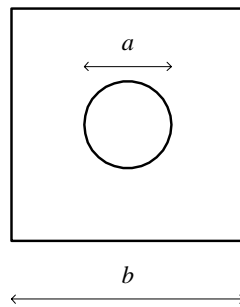


Fig. 4.2. Cross section of a coaxial resonator cavity.

Fig. 4.3 shows a side view and approximate circuit representation of a resonant cavity consisting of a short-circuited transmission line of length  $l$ .

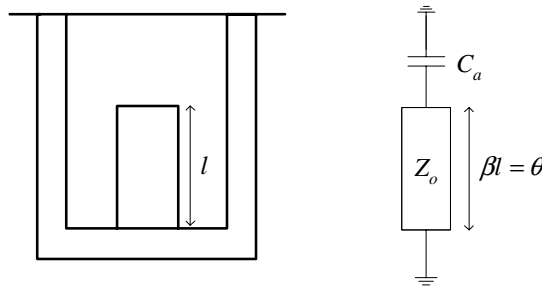


Fig. 4.3. Cross section and circuit representation of a single coaxial resonator.

Capacitor  $C_a$  represents the total capacitance between the end of the centre post and the grounded roof of the cavity. At resonance, the total parallel admittance of the transmission line and capacitor must be zero.

$$\begin{aligned} \frac{Y_0}{j \tan \theta_0} + j\omega_0 C_a &= 0 \\ \Rightarrow C_a &= \frac{1}{Z_0 \omega_0 \tan \theta_0} \end{aligned} \quad (4.2)$$

In the case where the transmission line is exactly a quarter wavelength long,  $\theta_0$  is equal to  $\pi/2$ , which means that  $C_a$  would have to be zero at resonance. This would require an infinite roof height, together with no parasitic capacitance. However, in practice there is always a certain amount of parasitic capacitance present. For this reason, the length of the resonator is always chosen to be less than a quarter wavelength. Although one can determine the required value of  $C_a$  from eqn. 4.2, there is no simple relation between that value and the distance to the cavity roof. This process is therefore best completed in a simulation package like CST Microwave Studio Version 5, where one chooses a suitable cavity roof height, and then optimises the post length for resonance at  $f_0$ . From eqn. 4.2 it is also clear that the shorter the post length, the bigger  $C_a$  has to be at resonance, which means that the distance between the cavity roof and centre post is reduced. However, this reduction in size comes at the price of a loss in unloaded Q, as the ratio of stored energy to dissipated energy is decreased. Table 4.1 lists the results of Q-factor calculations in CST with three different cavity sizes.

$l$ [mm]	Cavity roof height [mm]	Unloaded Q-factor
14.12	15	3720
21.17	30	4325
21.31	40	4326

TABLE 4.1

Q-factor simulations with different cavity  $z$ -dimensions;  $a = 6$  mm,  $b = 20.22$  mm.

Reduction of the cavity roof height from 30 mm to 15 mm causes the Q-factor to show a substantial decrease of 605. Additionally, because  $C_a$  contains a  $1/\tan \theta_0$  term, another disadvantage of a smaller cavity (with smaller resonator post length  $\theta_0$ ) is the more rapid variation of the capacitance  $C_a$  with  $\theta_0$ , making the resonant frequency more sensitive to

manufacturing tolerances and more difficult to tune than that of a larger cavity. When the roof height is increased from 30 mm to 40 mm, there is no increase in the Q-factor. The best cavity roof height is therefore one which reaches a good compromise between size and unloaded Q.

### 4.3 Positive Coupling Mechanisms

There are various ways in which to couple two neighbouring coaxial resonators. The easiest and most obvious way is to cut a hole in the wall which separates the two cavities. This is called iris coupling. Depending on where the iris is positioned, the coupling will be predominantly magnetic, or electric. As the establishment of coupling values is done mainly via simulation, the extraction of coupling values from simulation will be discussed next. Although the theory will be developed for a series coupled *LC* circuit, it can be applied directly to a parallel coupled circuit, as the same principles are used in the dual parallel derivation.

From Matthaei, Young and Jones [17, p.432] the coupling coefficient of a K-inverter between resonators *i* and *j* is given by eqn. 4.3.

$$k_{ij} = \frac{K_{ij}}{\sqrt{x_i x_j}} \quad (4.3)$$

where *x* is the reactance slope parameter of the two series resonators and *K* is the value of the impedance inverter. Please refer to Appendix B for the relation between coupling values and impedance and admittance inverters. For a simple series *LC* circuit,

$$\begin{aligned} x &= \left. \frac{\omega_0}{2} \frac{dX}{d\omega} \right|_{\omega_0} \\ &= \left. \frac{\omega_0}{2} \frac{d}{d\omega} \left( \omega L - \frac{1}{\omega C} \right) \right|_{\omega_0} \\ &= \omega_0 L \end{aligned} \quad (4.4)$$

as at resonance

$$\omega_0 L = \frac{1}{\omega_0 C}$$

Also, the value of a K-inverter realized by a T-network of inductors of value *M* is given by [17, p.436]

$$K = \omega M \quad (4.5)$$

By now substituting eqns. 4.4 and 4.5 into 4.3, the coupling coefficient at resonance is

$$k_{ij} = \frac{M_{ij}}{\sqrt{L_i L_j}} \quad (4.6)$$

For identical resonators,

$$k_{ij} = \frac{M_{ij}}{L} \quad (4.7)$$

The next step in the definition of the coupling factor, is to look at the planes of symmetry utilised by so many analysis methods. Take the simple magnetically coupled two-resonator structure of Fig. 4.4.

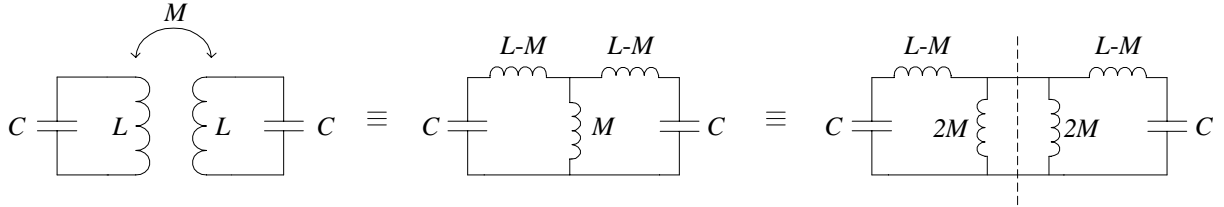


Fig. 4.4. Equivalent circuit of two magnetically coupled resonators.

The introduction of a plane of symmetry makes it possible to determine the resonant frequencies of only half of the structure, first with an electric wall (short circuit) and then with a magnetic wall (open circuit) at the symmetry plane, corresponding to  $f_e$  and  $f_m$ , respectively.

$$\begin{aligned} f_e &= \frac{1}{2\pi\sqrt{(L-M)C}} \\ f_m &= \frac{1}{2\pi\sqrt{(L+M)C}} \end{aligned} \quad (4.8)$$

By substituting eqn. 4.7 into eqn. 4.8 and squaring it, the resonant frequencies can be expressed in terms of the magnetic coupling coefficient  $k_m$ .

$$\begin{aligned} f_e^2 &= \frac{1}{4\pi^2(1-k_m)LC} \\ f_m^2 &= \frac{1}{4\pi^2(1+k_m)LC} \end{aligned} \quad (4.9)$$

Therefore,

$$\frac{1}{4\pi^2LC} = f_e^2(1-k_m) \quad (4.10)$$

and

$$f_m^2 = \frac{(1-k_m)f_e^2}{(1+k_m)} \quad (4.11)$$

It is now possible to solve the coupling coefficient in terms of the electric and magnetic resonant frequencies.

$$k_m = \frac{f_e^2 - f_m^2}{f_e^2 + f_m^2} \quad (4.12)$$

The same procedure can be repeated for two electrically-coupled resonators, as shown in Fig. 4.5 [19].

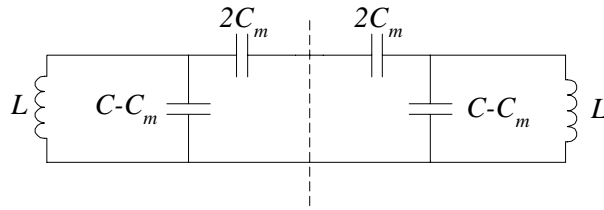


Fig. 4.5. Equivalent circuit of two electrically coupled resonators.

$L$  and  $C$  form the parallel resonator, with  $C_m$  the value of the electrical coupling. The result is a coupling coefficient of

$$k_c = \frac{f_m^2 - f_e^2}{f_m^2 + f_e^2} \quad (4.13)$$

Comparison with eqn. 4.12 shows that the magnetic and electric coupling coefficients differ in sign. It has become common practice to choose magnetic coupling as positive. Therefore, for positive coupling,  $f_e > f_m$ . In the current implementation, the  $LC$  resonators are realised with coaxial resonant cavities. Therefore, when using a simulation package like CST Microwave Studio, the first establishment of coupling will be through the analysis of two cavities, coupled by an iris of certain size and location. After solving the first two eigenmodes in frequency of the structure and inspecting the field distributions, one finds that one of the modes possesses perpendicular electric fields, while the other mode possesses perpendicular magnetic fields at the plane of symmetry. This corresponds to the introduction of an electric wall (short circuit) and magnetic wall (open circuit), respectively, at the plane of symmetry. As a result, the frequency of the mode with perpendicular E-fields is  $f_e$ , and the frequency of the mode with perpendicular H-fields is  $f_m$ . For positive coupling, the eigenmode with perpendicular E-fields at the aperture location should therefore occur at a higher frequency than the eigenmode with perpendicular H-fields. When this is not the case, the coupling is considered negative.

The main fields inside a coaxial resonator have the general distribution shown in Fig. 4.6.

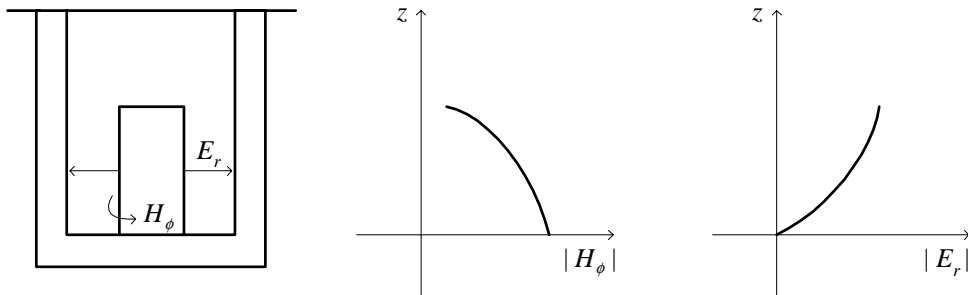


Fig. 4.6. General distribution of E-fields and H-fields in a coaxial resonator cavity.

The radial electric fields are zero at the bottom of the cavity (at  $z = 0$ ) and increase toward the top, while the magnetic fields around the centre post are a maximum at the bottom of the cavity and decrease toward the top. Accordingly, if one is interested in

magnetic coupling, one should place an iris at the bottom of the cavity, as illustrated in Fig 4.7.

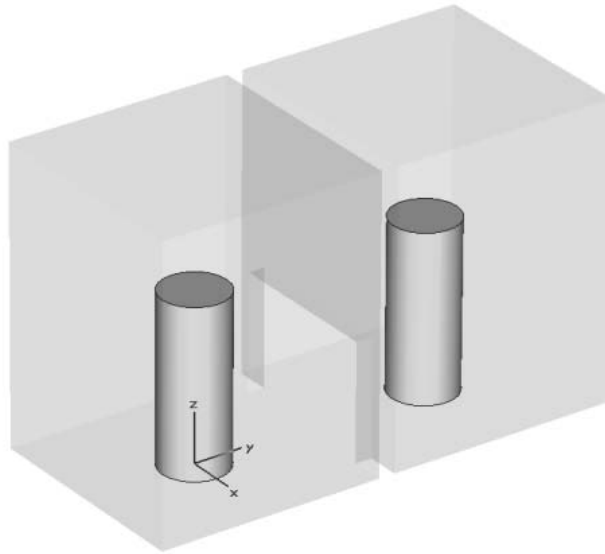


Fig. 4.7. Two magnetically coupled coaxial resonator cavities.

It is, however, possible to achieve magnetic coupling with the iris located at the open ended side of the cavity. In this case, the iris dimension in the  $z$ -direction has to be large enough for the magnetic energy at the short-circuited end of the cavity to dominate.

## 4.4 Negative Coupling Mechanisms

The achievement of negative coupling between two neighbouring coaxial resonators is no trivial matter. Although the placement of an iris at the open end of the cavity (where the electric fields dominate) can indeed yield negative coupling, these values are small and have a limited range. This poses a problem, as many synthesised values for capacitive coupling require values larger than what iris coupling can provide. Additionally, the dimensions of the structure have a significant effect on the realisability of negative coupling. For example, with large values of resonator base length  $b$ , capacitive iris coupling becomes impossible, irrespective of other resonator dimensions. The three negative coupling mechanisms that are commonly used include iris-, evanescent mode- and capacitive probe coupling.

### 4.4.1 Iris Coupling

From simulations in CST Microwave Studio, it was found that the unloaded Q-factor shows considerable variation with respect to the resonator centre post diameter. The

structure used in the experiment is illustrated in Fig. 4.8.

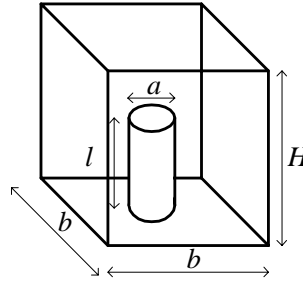


Fig. 4.8. Structure used for the Q-factor simulations.

For ease of comparison, the cavity height  $H$  was kept constant at 30 mm, while varying the resonator post diameter  $a$  and resonator side length  $b$ . As calculated in Section 4.2,  $b/a = 3.369$  for a  $77 \Omega$  filter. For each new value of  $a$  and  $b$ , the resonator post length  $l$  was optimised for resonance at 3 GHz. Table 4.2 summarises the results.

$a$ [mm]	$b$ [mm]	$l$ [mm]	$H$ [mm]	$Q_u$
4	13.48	22.51	30	3066
6	20.22	21.17	30	4325
8	26.95	19.71	30	5496
10	33.69	18.16	30	6197

TABLE 4.2

Unloaded Q-factor as a function of resonator post diameter.

For the first iteration of the resonant cavity design, it was therefore decided to pick a relatively thick centre post with a diameter of 10 mm in order to create a resonator with unloaded Q values in the range of 6000. However, it was found that this structure is unable to realise capacitive coupling, irrespective of the iris location and size.

Comparison with a coaxial resonator design by El Sabbagh [20] pointed out a considerable difference in the behaviour of the coupling coefficients with the increase of iris height in the  $z$ -direction, as shown in Fig. 4.10. In both cases, the iris is placed at the open end of the resonator, as shown in Fig. 4.9.

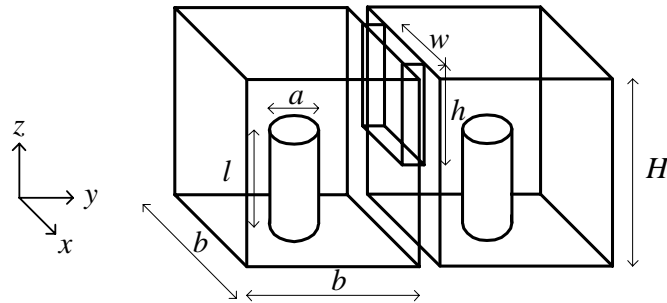


Fig. 4.9. Setup to compare the negative coupling of two sizes of filter.

The expected behaviour of the electric coupling, as illustrated by the El Sabbagh filter, is to increase with iris height, until the magnetic energy at the short-circuited end of

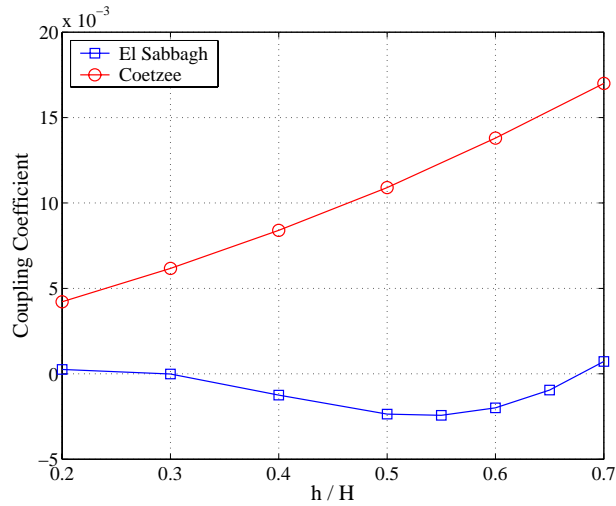


Fig. 4.10. Coupling coefficient versus aperture height for different coaxial resonators. El Sabbagh dimensions [mm]:  $a=5.84$ ,  $b=19.05$ ,  $l=25.27$ ,  $H=33.40$ ,  $w=19.05$ . Coetzee dimensions [mm]:  $a=10$ ,  $b=33.69$ ,  $l=18.36$ ,  $H=32.0$ ,  $w=19.05$ .

the cavity starts to reduce the electric coupling and eventually dominates by making the coupling coefficient positive. The main difference between the two filters is the diameter of the centre posts, and accordingly, the width of the resonator sides. The El Sabbagh filter has a much smaller centre conductor radius, with the result that its cavities have a smaller base in the  $xy$ -plane.

To investigate this further, the E-fields and H-fields at the aperture location on the cavity wall were monitored for cavities of different sizes, and compared with the corresponding coupling value. The following relations between cavity size and coupling value were found:

- For post diameter values ranging from 5 mm to 10 mm, the aperture normal E-field at the  $z$ -value corresponding to the open end of the resonator, increases with an increase in post length, while tangential H-field does not show substantial change.
- The thicker the centre post, the smaller the aforementioned E-field.
- For post diameters smaller than 8 mm, negative (E-field) coupling becomes possible when the post length is increased beyond a certain value. The thicker the post, the more difficult it becomes to realise negative coupling. For a post diameter of 10 mm it is impossible, irrespective of the post length.

Thus, it would appear that there is a boundary value which the E-field must reach at the aperture location before E-field coupling becomes possible, and also that the strong magnetic field present at the aperture location when shorter thicker posts are used, make E-field coupling impossible. This notion was investigated further with the aid of small aperture theory.



The determination of the field coupled through small apertures is a problem which was first addressed by Bethe in 1944 [2]. This original theory is applicable to small circular and elliptical apertures, but not to rectangular or more geometrically complex apertures. Still, Bethe's electric and magnetic dipole moments have been used extensively in many coupled cavity and waveguide system designs. In the 1950's, Cohn developed an electrolytic tank in which he measured the polarizability of small apertures of arbitrary shape [3, 4]. Before the days of sophisticated simulation packages, this data was used in many aperture designs. Up to this point, the effect of finite wall thickness and large apertures had not been taken into account. A major extension to the work was made by Cohn in 1952 [21] which enabled the theory of Bethe to be applied to large apertures of finite thickness. However, this thickness correction factor was not exact, and effective thickness factors had to be included to ensure agreement with measurements. In 1972 McDonald developed a rigorous method for evaluating the coupling between two identical resonant cavities coupled by small apertures in a plane wall of arbitrary thickness [5]. The inclusion of his thickness correction factor in modified Bethe-Cohn theory resulted in excellent agreement between theory and measurements, with no required empirical adjustments. Levy improved the large aperture theory in 1979 by averaging fields over the aperture [6], resulting in an additional correction term to Cohn's aperture resonance term.

As the goal of this section is to investigate the effect of post thickness on the electric coupling capability, and not the exact determination of the coupling coefficient (as this can be calculated from simulation), the full suite of correction terms will not be included. The coupling coefficient  $k$  through a small aperture in a wall of zero thickness between two lossless, identical resonant cavities is given by eqn. 4.14 [5].

$$k = p_m \frac{\mathbf{H}_{\text{pt}} \cdot \mathbf{H}_{\text{pt}}}{\int \int \int_v \mathbf{H}_{\mathbf{p}} \cdot \mathbf{H}_{\mathbf{p}} dv} + p_e \frac{\mathbf{E}_{\text{pn}} \cdot \mathbf{E}_{\text{pn}}}{\int \int \int_v \mathbf{E}_{\mathbf{p}} \cdot \mathbf{E}_{\mathbf{p}} dv} \quad (4.14)$$

with  $p_m$  and  $p_e$  the magnetic and electric polarizability,  $\mathbf{H}_{\text{pt}}$  and  $\mathbf{E}_{\text{pn}}$  the tangential magnetic field and normal electric field at the aperture, and  $\mathbf{H}_{\mathbf{p}}$  and  $\mathbf{E}_{\mathbf{p}}$  the magnetic and electric fields in the cavity. The normalising integration in the denominator is performed over the volume of one cavity. The equivalent polarizabilities of a small rectangular aperture are given by McDonald as

$$\begin{aligned} p_m &= R_H A^3 \\ p_e &= -R_E A^3 \end{aligned} \quad (4.15)$$

The dimensionless coefficients  $R_H$  and  $R_E$  are provided for various aspect ratios in [5], with  $A$  the maximum aperture dimension.

Eqn. 4.14 assumes that the fields over the aperture are constant. In order to expand it for apertures large with regards to a wavelength, Levy proposes that one computes the

average fields at the aperture location [6]. Therefore,

$$\begin{aligned} \mathbf{H}_{\text{pt}} \cdot \mathbf{H}_{\text{pt}} &\rightarrow \frac{\int \int_A |\mathbf{H}_{\text{pt}}|^2 da}{wh} \\ \mathbf{E}_{\text{pn}} \cdot \mathbf{E}_{\text{pn}} &\rightarrow \frac{\int \int_A |\mathbf{E}_{\text{pn}}|^2 da}{wh} \end{aligned} \quad (4.16)$$

with  $wh$  the aperture area in  $\text{m}^2$ . The data needed to compute these numerical integrations was obtained from single cavity simulations in CST Microwave Studio, with 2D field monitors placed at the aperture location and 3D monitors placed in the cavity volume. Numerical area integration was performed by multiplying the field value at every point with the incremental square area connected to it. The numerical volume integrals were computed similarly.

Coupling values obtained with this type of small aperture theory differ slightly from the CST values, but show the same basic behaviour. This is to be expected, as the thickness correction factor and aperture resonance factor were not included in the calculations. To compute the coupling values in CST, two resonators are coupled by an aperture, with dimensions as illustrated in Fig. 4.9. The trends observed with the variation of different filter parameters will now be summarised.

### Effect of Post Radius

A comparison between the coupling values obtained with small aperture theory (SAT) and CST Microwave Studio simulations is given in Fig. 4.11(a). For this experiment, the post radii ( $a/2$ ) were varied, followed by an adjustment in the cavity side length  $b$  according to the  $b/a = 3.369$  condition for a  $77 \Omega$  resonator. The cavity height and aperture size were maintained at predetermined values of  $H = 35 \text{ mm}$  and  $h \times w = 0.4H \times b$ , respectively, to ensure sensible comparison of coupling values. The aperture location is at the open end of the resonator post.

Both the SAT calculations and CST simulations show how the coupling factor becomes positive when the resonator post radius is increased above a certain value. As the post radius increases, the ratio of average E-field to H-field in the aperture decreases, as illustrated in Fig. 4.11(b). This was calculated by taking the ratio of the two terms in eqn. 4.16. The downward trend corresponds to the earlier findings in CST that showed a reduction in normal E-field at the aperture location for thicker resonator posts. Referring to eqn. 4.14, it can be seen that a decrease in the second term containing the electrical energy will eventually lead to positive coupling.

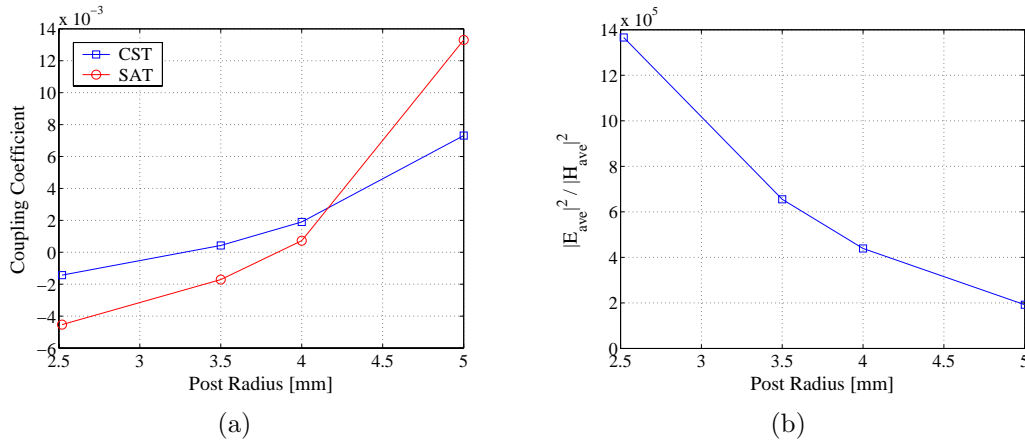


Fig. 4.11. The effect of the coaxial resonator post radius on the coupling coefficient, and electric and magnetic energy at the aperture. Dimensions [mm]:  $b=[17 \ 23.59 \ 26.95 \ 33.59]$ ,  $l=[21.91 \ 20.65 \ 19.95 \ 18.56]$ ,  $H=35$ ,  $w=b$ ,  $h=14$ .

### Effect of Aperture Height

The aperture used in this experiment was again made at the open end of the resonator, with its width  $w$  equal to the cavity side length  $b$ , and height  $h$ . The total cavity height is defined as  $H$ . A small post radius of 2.52 mm was chosen, to ensure that negative coupling is indeed possible. As  $h$  increases from  $0.3H$  to  $0.7H$ , the average E-field at the aperture increases 5 times, while the average H-field increases 22 times. The ratio of average E-field to H-field is plotted in Fig 4.12(b). The magnetic energy thus increases quicker than the electric energy toward the short circuit end of the post, which means that when electric coupling is possible, it will first increase with  $h$ , then decrease as the magnetic energy begins to dominate. The coupling coefficient calculated with eqn. 4.14 shows it to indeed be the case, as illustrated in Fig. 4.12(a). This behaviour agrees with CST simulations and the findings of El Sabbagh in [20].

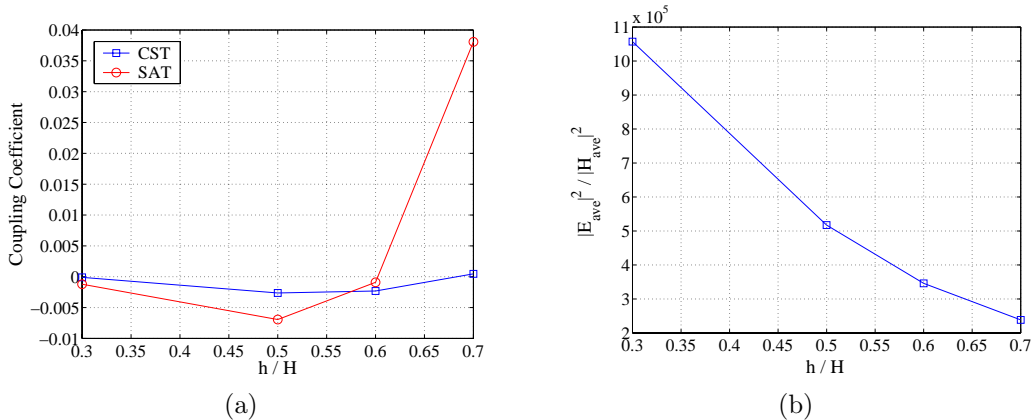


Fig. 4.12. The effect of the aperture height on the coupling coefficient, and electric and magnetic energy at the aperture. Dimensions [mm]:  $a=5.04$ ,  $b=17$ ,  $l=21.91$ ,  $H=35$ ,  $w=17$ .

### Effect of Post Length

For this experiment, a post radius of 3.5 mm was chosen, with an aperture height  $h$  of  $0.4H$  and aperture width  $w$  equal to the cavity side length  $b$ , situated at the open end of the resonator. For each new post length  $l$ , the cavity height was re-optimised for resonance at 3 GHz. Fig. 4.13(b) shows the ratio of average E-field to H-field at the aperture location, as calculated with eqn. 4.16. It illustrates a clear increase in E-field with increasing post length. When a certain boundary value is surpassed, the coupling becomes negative, as illustrated in Fig. 4.13(a).

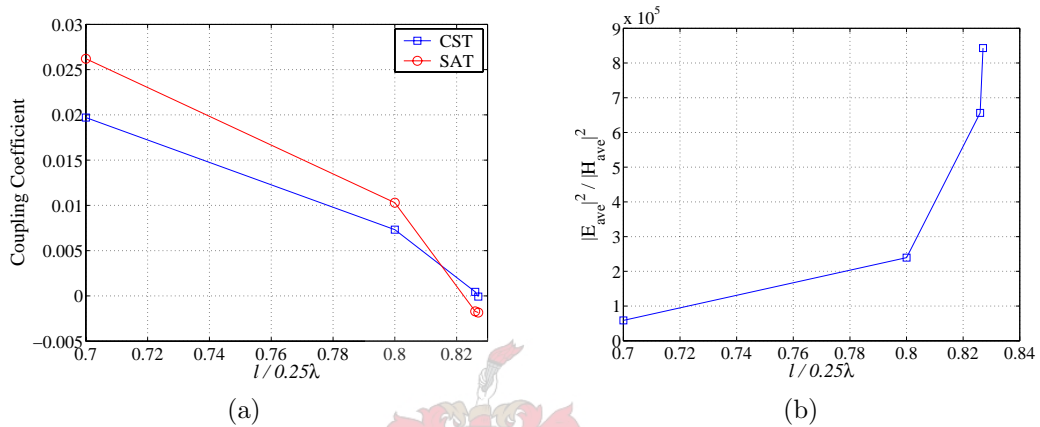


Fig. 4.13. The effect of the length of the coaxial resonator post on the coupling coefficient, and electric and magnetic energy at the aperture. Dimensions [mm]:  $a=7$ ,  $b=23.59$ ,  $l=[17.5 \ 20 \ 20.65 \ 20.68]$ ,  $H=[20.1 \ 26.57 \ 35 \ 38.9]$ ,  $w=23.59$ ,  $h=[8.04 \ 10.63 \ 14 \ 15.56]$ .

The results obtained with small aperture theory agrees well with CST simulations, and aids one in the understanding of the mechanisms behind aperture coupling. For each of the above parameter sweeps, the transitions between positive and negative coupling can be explained in terms of the average electric and magnetic energy at the aperture location.

Although negative iris coupling is simple to construct, its uses are limited by the small range and size of the coupling values obtainable.

### 4.4.2 Evanescent Mode Coupling

In a 1997 article by Snyder [22], the use of an evanescent mode coupling element is proposed as an alternative method for realizing positive and negative couplings. A large range of coupling values is obtained by utilising the phase shift and impedance characteristics of the bandpass element represented by a short resonated section of evanescent waveguide. Essentially, the coupling element is a single-pole evanescent mode bandpass filter, of which the transfer function provides the necessary coupling between two adjacent resonant cavities of the main bandpass filter. Fig. 4.14 shows an example of two coaxial resonator cavities coupled by such an element.

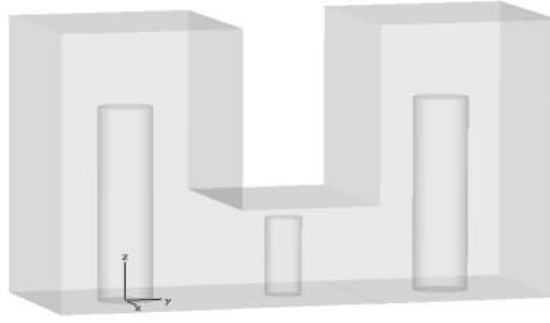


Fig. 4.14. Coaxial resonators coupled by a single-pole evanescent mode filter.

The basic theory behind such waveguide filters was presented in 1971 by Craven and Mok [23]. When one works with the assumption that the only mode in the guide is the  $TE_{10}$  evanescent mode, it is possible to represent the guide with a simple lossless transmission line equivalent of characteristic impedance

$$Z_0 = jX_0 \quad (4.17)$$

with

$$\begin{aligned} X_0 &= \frac{120\pi b}{a\sqrt{\left(\frac{\lambda}{\lambda_c}\right)^2 - 1}} \\ f_{c,10} &= \frac{1}{2a\sqrt{\mu\epsilon}} \\ \lambda_c &= \frac{c}{f_{c,10}} = 2a \end{aligned} \quad (4.18)$$

In eqn. 4.18,  $\lambda_c$  represents the cutoff wavelength of the waveguide,  $\lambda$  is the free space wavelength,  $f_{c,10}$  is the cutoff frequency of the  $TE_{10}$  mode, and  $a$  and  $b$  are the waveguide dimensions, as illustrated in Fig. 4.15.

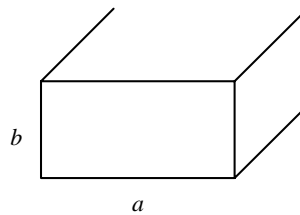


Fig. 4.15. Dimensions of the evanescent mode waveguide.

The propagation constant  $\gamma$  is given by

$$\gamma = \frac{2\pi}{\lambda} \sqrt{\left(\frac{\lambda}{\lambda_c}\right)^2 - 1} \quad (4.19)$$

Fig. 4.16(a) shows the transmission line equivalent circuit of a piece of evanescent mode

waveguide, which can be expressed in terms of an equivalent Pi-section.

$$j\omega_0 L_s = jX_0 \sinh(\gamma l) \tag{4.20}$$

$$j\omega_0 L_{p1} = jX_0 \coth\left(\frac{\gamma l}{2}\right) \tag{4.21}$$

As the propagation constant is real over the frequency range  $\{0 < f < f_{c,10}\}$ , the elements in the Pi-section can be treated as lumped inductors. To create a bandpass filter, one simply adds lumped capacitors to the model, as shown in Fig. 4.16(b).

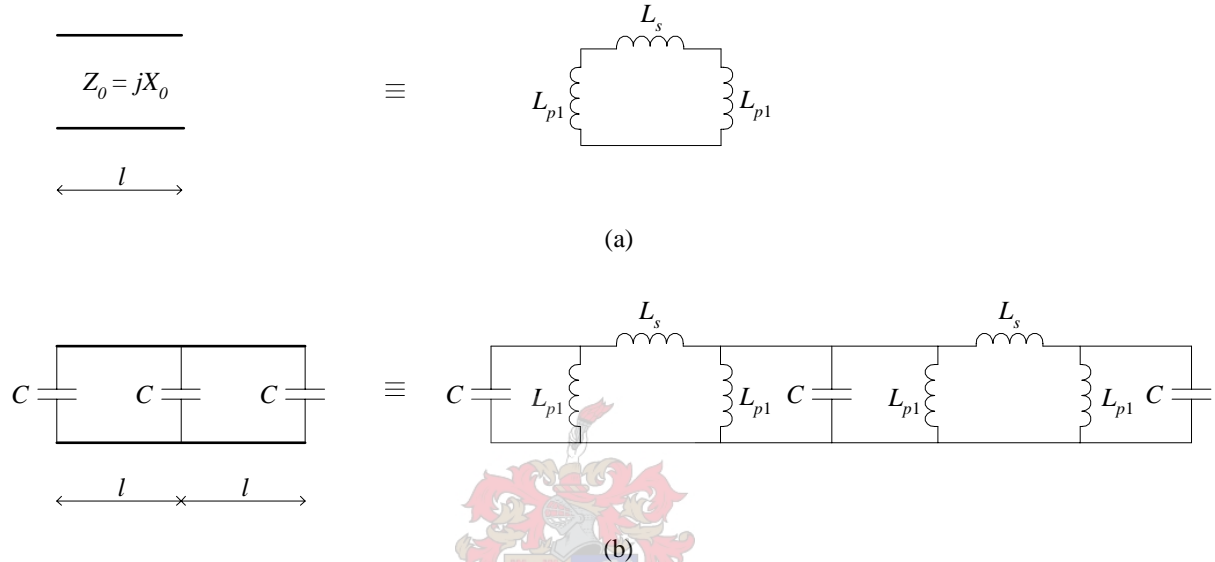


Fig. 4.16. Construction of a bandpass filter with evanescent mode elements.

For the purpose of a single-pole coupling element, one uses the equivalent circuit of Fig. 4.17, with two sections of evanescent guide on either side of a capacitor, providing a single pole of resonance. An unknown transformer is included at the ends where the evanescent sections couple to the main cavities. Additionally, there exists a net parallel reactance that transforms across to the main cavity, altering the original resonant frequency. To reverse the effect of this offset, it is recommended that a tuning mechanism is included in the main cavity.

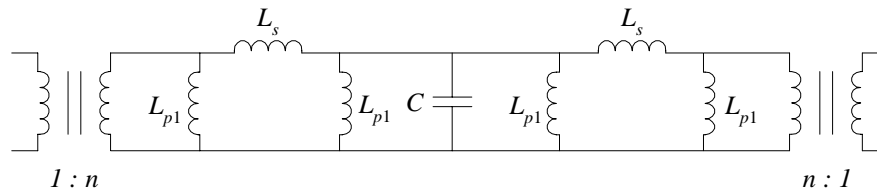


Fig. 4.17. A single-pole bandpass filter constructed from evanescent mode elements.

It is not a big leap of the imagination to imagine the Pi-network of inductors in Fig. 4.17 as a J-inverter. For that to be possible, the two parallel inductors on either side of the series inductor must have the same value as the series inductor, but with a different sign. One can create this artificially by dividing the current parallel inductor up into

two parts, with the inside element having the required value, and the impedance of the parallel combination equal to the original value of  $jX_0 \coth(\frac{\gamma l}{2})$ . This leads to the circuit in Fig. 4.18, with

$$j\omega_0 L_s = jX_0 \sinh(\gamma l) \quad (4.22)$$

$$j\omega_0 L_p = jX_0 \tanh(\gamma l) \quad (4.23)$$

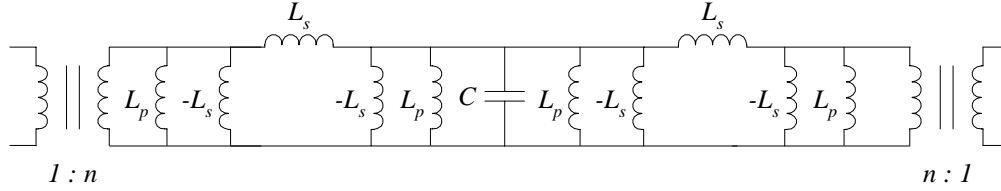


Fig. 4.18. A single-pole evanescent mode bandpass filter with J-inverters.

In order to gain a better understanding of the requirements for negative coupling in this structure, an even-odd mode analysis is completed with the equivalent circuit of Fig. 4.18 and compared with an even-odd analysis of an ideal J-inverter. Referring to Fig. 4.19 and using the properties of an ideal J-inverter outlined in Appendix B, the even mode and odd mode admittances of the single-pole evanescent mode filter can be determined in eqn. 4.24.  $Y_{in,e}$  and  $Y_{in,o}$  is the input admittance with an open circuit and short circuit, respectively, at the plane of symmetry. Also,  $B_c = \omega C$ ,  $X_s = \omega_0 L_s$  and  $X_p = \omega_0 L_p$ .

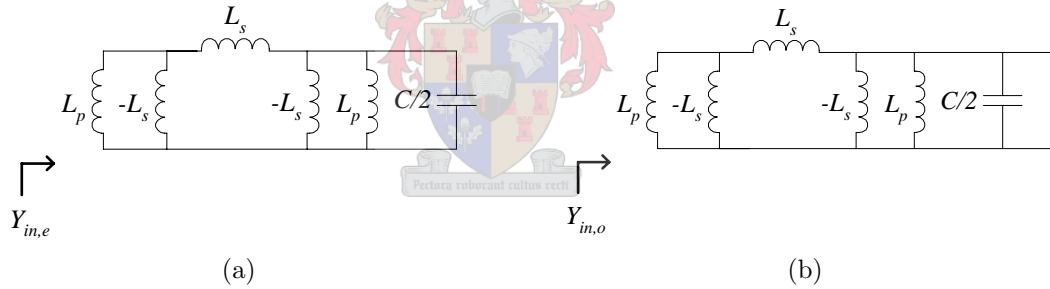


Fig. 4.19. Even and odd mode admittances of the single-pole evanescent mode filter.

$$\begin{aligned} Y_{in,e} &= \frac{1}{jX_p} + \frac{\left(\frac{1}{X_s}\right)^2}{\frac{1}{jX_p} + j\frac{B_c}{2}} \\ &= -j \left[ \frac{X_s^2 \left(\frac{B_c}{2} - \frac{1}{X_p}\right) + X_p}{X_p X_s^2 \left(\frac{B_c}{2} - \frac{1}{X_p}\right)} \right] \\ Y_{in,o} &= \frac{1}{jX_p} \end{aligned} \quad (4.24)$$

Next, the evanescent mode filter is modeled as an ideal J-inverter, with unknown parallel capacitances of admittance  $jB_p$  at its ends and the plane of symmetry indicated by a dotted line, as illustrated in Fig. 4.20.

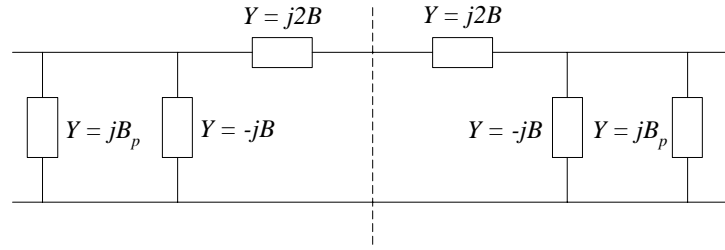


Fig. 4.20. An ideal J-inverter with end capacitors.

For this circuit,

$$\begin{aligned} Y_{in,e} &= jB_p - jB \\ Y_{in,o} &= jB_p + jB \end{aligned} \quad (4.25)$$

It follows that

$$Y_{in,o} - Y_{in,e} = j2B \quad (4.26)$$

This can now be applied to eqn. 4.24.

$$\begin{aligned} Y_{in,o} - Y_{in,e} &= \frac{1}{jX_p} + j \left[ \frac{X_s^2 \left( \frac{B_c}{2} - \frac{1}{X_p} \right) + X_p}{X_p X_s^2 \left( \frac{B_c}{2} - \frac{1}{X_p} \right)} \right] \\ &= j \frac{1}{\frac{X_s^2 B_c}{2} - \frac{X_s^2}{X_p}} \end{aligned} \quad (4.27)$$

From the theory of inverters, the coupling is negative if  $B > 0$ , and therefore also if  $2B > 0$ . Applying this negative coupling criterion to eqn. 4.27 results in

$$\begin{aligned} \frac{1}{\frac{X_s^2 B_c}{2} - \frac{X_s^2}{X_p}} &> 0 \\ \Rightarrow \frac{X_s^2 B_c}{2} &> \frac{X_s^2}{X_p} \\ \Rightarrow B_c &> \frac{2}{X_p} \end{aligned} \quad (4.28)$$

This result indicates that in order to realise negative coupling, the capacitor must exceed a certain value, related to the parallel inductor  $L_p$ , and therefore to the length of the evanescent section.

This was confirmed by building the model of Fig. 4.18 in Microwave Office Version 6.01 and inserting it between two identical  $LC$  resonators. The S-parameters were then compared with the S-parameters of an ideal J-inverter between the same two identical resonators. By making the parameters of the evanescent coupling element tunable and setting the ideal J-inverter coupling value to negative, the two sets of S-parameters were made equivalent



by adjusting the evanescent coupling parameters, thereby realising negative coupling. When tested against eqn. 4.28,  $B_c$  is indeed greater than  $2/X_p$ . Positive coupling was also realised by repeating the process for a positive ideal coupling element, and this time  $B_c$  is smaller than  $2/X_p$ , as expected. The main difference between the two sets of values is the value of the capacitor, which must be sufficiently large to realise negative coupling.

In order to implement evanescent mode coupling with a physical structure in CST, two coaxial resonator cavities are coupled by a certain length of below cutoff guide with a capacitive post inside, as illustrated in Fig. 4.21. As discussed in Section 4.3, the resonant frequencies  $f_e$  and  $f_m$  (corresponding to a perfect electric and magnetic wall at the symmetry plane, respectively) can be determined from the first two resonant modes and their corresponding field distributions, making it possible to determine the coupling coefficient. The relevant evanescent mode element parameters are illustrated in Fig. 4.21.

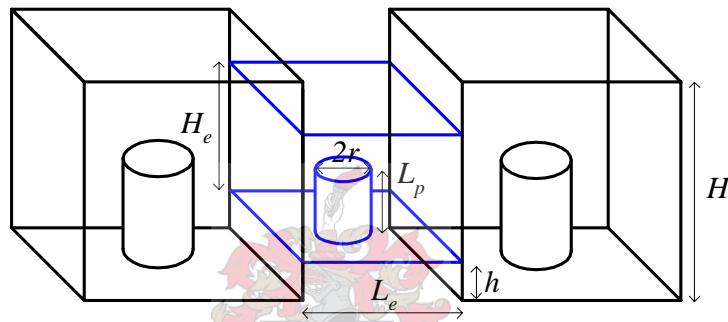


Fig. 4.21. Parameters used in the evanescent mode coupling element experiments.

By adjusting one parameter at a time, the following trends were identified:

- The larger the length  $L_p$  of the capacitive post, the lower the frequency of the first eigenmode, mode 1, becomes (Fig. 4.22(b)). Beyond a certain length of  $L_p$ , the E-fields of mode 1 exist only around the capacitive post in the evanescent section. Mode 1 can then be treated as a spurious mode and disregarded in the coupling calculation. Accordingly, mode 2 and mode 3 are treated as the first two eigenmodes in frequency. When  $L_p$ , which essentially determines the capacitance of the evanescent section, is large enough to cause this behaviour, it was found that mode 2 corresponds to  $f_e$  and mode 3 corresponds to  $f_m$ . This is, per definition, negative coupling (Fig. 4.22(a)).
- The effect of mode 1 is, however, not negligible. When completing a two port S-parameter simulation, there exists a very narrow spurious pass band at the frequency of mode 1. The aim is, therefore, to establish negative coupling with mode 1 as low in frequency as possible, to prevent interference in the pass band.
- When considering the offset  $h$  of the evanescent section from the shorted end of the main cavities, it is found that the smaller the value of  $h$ , the larger the negative

coupling (Fig. 4.23(a)), and the lower the frequency of mode 1 (Fig. 4.23(b)). As the evanescent mode coupling element is primarily an H-field coupling element, with inversion created by the centre capacitor, the coupling value will be the largest where the H-fields in the main resonator cavities are the largest. As discussed in Section 4.3, this is the case at the shorted end of the cavity, where  $h = 0$ .

- The shorter the length  $L_e$  of evanescent section, the larger the value of the negative coupling and the lower the frequency of the spurious mode 1 (Fig. 4.24). The reason for this increase in negative coupling value lies in the dependence of inductors  $L_s$  and  $L_p$  on the length of the evanescent section. In eqns. 4.22 and 4.23,  $X_0$  is independent of  $l$ . Accordingly, by using  $L_s \propto \sinh(\gamma l)$  and  $L_p \propto \tanh(\gamma l)$ , and choosing a value for  $B_c$  which satisfies the negative coupling condition in eqn. 4.28, the value of the J-inverter equivalent to the evanescent mode coupling element can be calculated with the aid of eqn. 4.26 and 4.27.

$$J = B = \frac{1}{X_s^2 B_c - \frac{2X_s^2}{X_p}} \quad (4.29)$$

Eqn. 4.29 shows the negative coupling value  $B$  to increase with a decrease in  $l$ , and therefore also with a decrease in  $L_e$ .

- When the radius  $r$  of the evanescent post is increased above a certain value, its capacitance becomes large enough to realise negative coupling (Fig. 4.25(a)). For larger  $r$ , mode 1 also moves down in frequency (Fig. 4.25(b)).

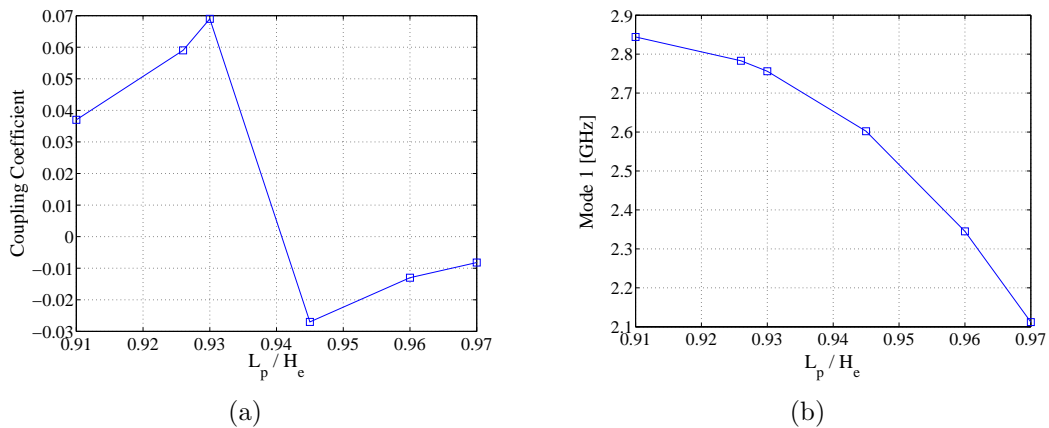


Fig. 4.22. Coupling coefficient and frequency of mode 1 as a function of  $L_p$ .  $H_e/H = 0.35$ ,  $r = 4.4$  mm,  $L_e = 16$  mm,  $h = 0$ .

From the above simulations, it can be seen that coupling is a very strong function of post radius, post length and offset. The fact that this coupling mechanism is tunable after initial construction, makes it an attractive option.

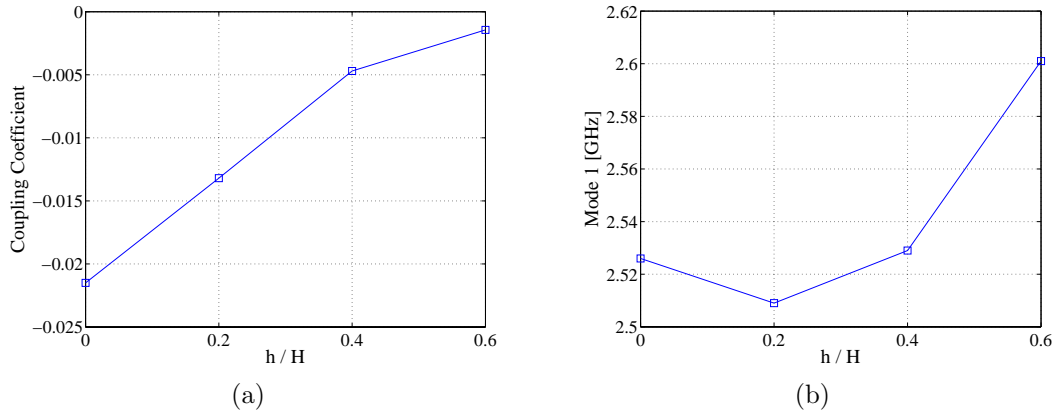


Fig. 4.23. Coupling coefficient and frequency of mode 1 as a function of  $h$ .  $H_e/H = 0.35$ ,  $L_p/H_e = 0.95$ ,  $r = 4.4$  mm,  $L_e = 16$  mm.

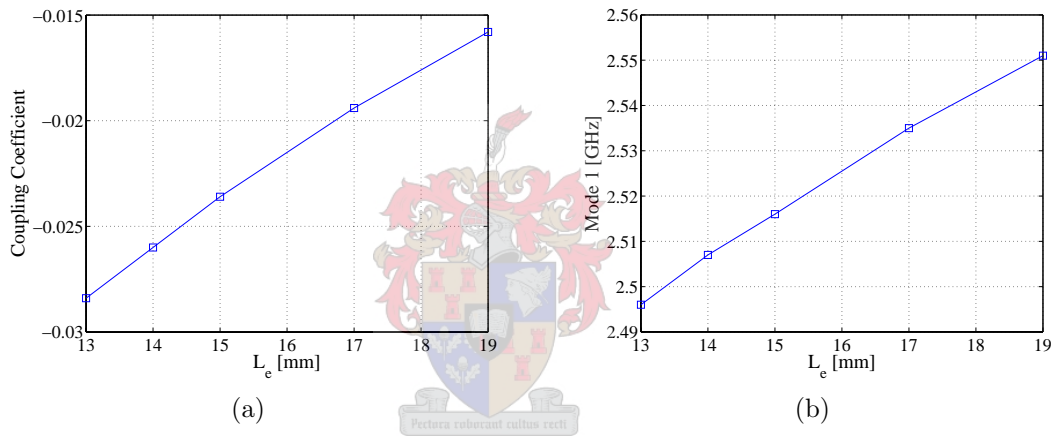


Fig. 4.24. Coupling coefficient and frequency of mode 1 as a function of  $L_e$ .  $H_e/H = 0.35$ ,  $L_p/H_e = 0.95$ ,  $r = 4.4$  mm,  $h = 0$  mm.

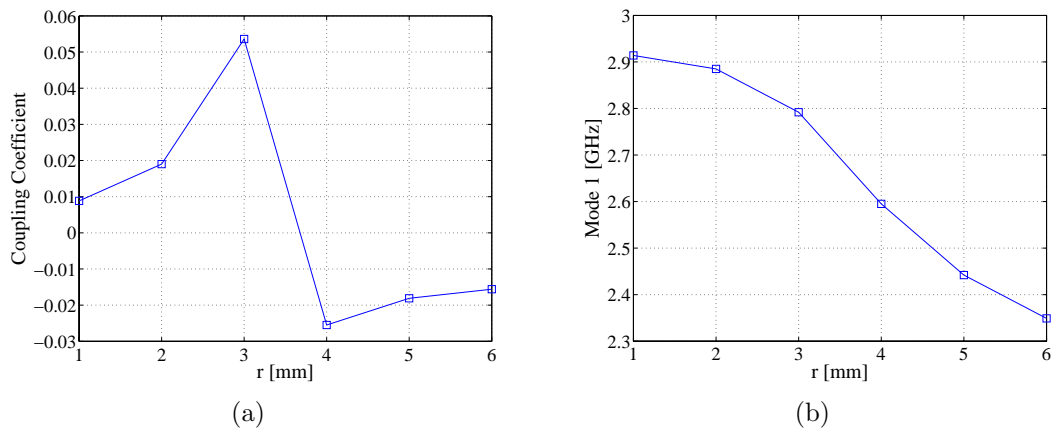


Fig. 4.25. Coupling coefficient and frequency of mode 1 as a function of  $r$ .  $H_e/H = 0.35$ ,  $L_p/H_e = 0.95$ ,  $L_e = 16$  mm,  $h = 0$ .

### 4.4.3 Capacitive Probe Coupling

The third negative coupling mechanism to be investigated is probe coupling. Fig. 4.26 gives an example of two coaxial resonator cavities coupled by a section of transmission line with extended centre conductors terminated in circular disks.

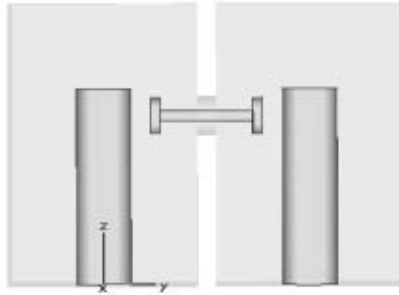


Fig. 4.26. Two coaxial resonators coupled by a capacitive probe.

This mechanism couples only capacitively (negatively), unlike the iris- and evanescent mode coupling discussed in previous sections. A useful range of couplings can be achieved with this structure, ranging from about  $-0.003$  to  $-0.09$ . In Figs. 4.28(a)–(d) the coupling values are plotted versus various parameters like the probe offset  $h$ , probe length  $L$ , disk thickness  $t$ , and disk radius  $r$ . The definitions of these parameters are illustrated in Fig. 4.27.

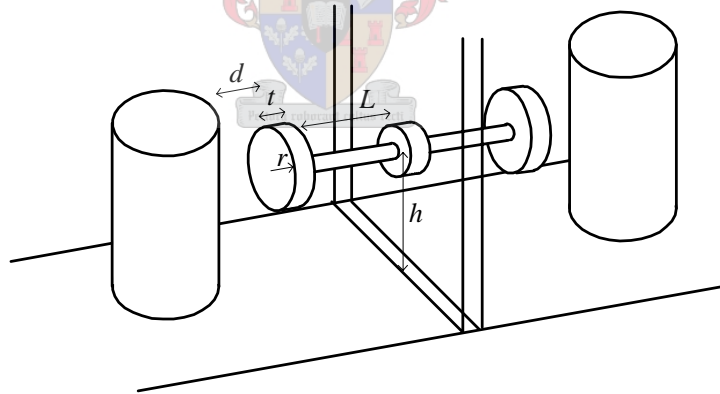


Fig. 4.27. Parameters used in the capacitive probe coupling experiments.

When considering Fig. 4.28(a), it is clear that the coupling value shows great variation with probe offset. The maximum coupling value exists at the value of  $h$  where the E-fields of the coaxial resonator reach their maximum. By varying the distance between the terminating disks and resonator post, a large range of coupling values can be achieved, as shown in Fig. 4.28(b). As  $d$  is decreased, the E-field strength between the disk and resonator post increases, leading to an increase in coupling value. In Fig. 4.28(c), variation of the disk thickness has a relatively small effect on the coupling. Larger values of disk radius, however, lead to a substantial increase in coupling, due to the greater amount of E-field lines terminating on the disks. This is illustrated in Fig. 4.28(d).

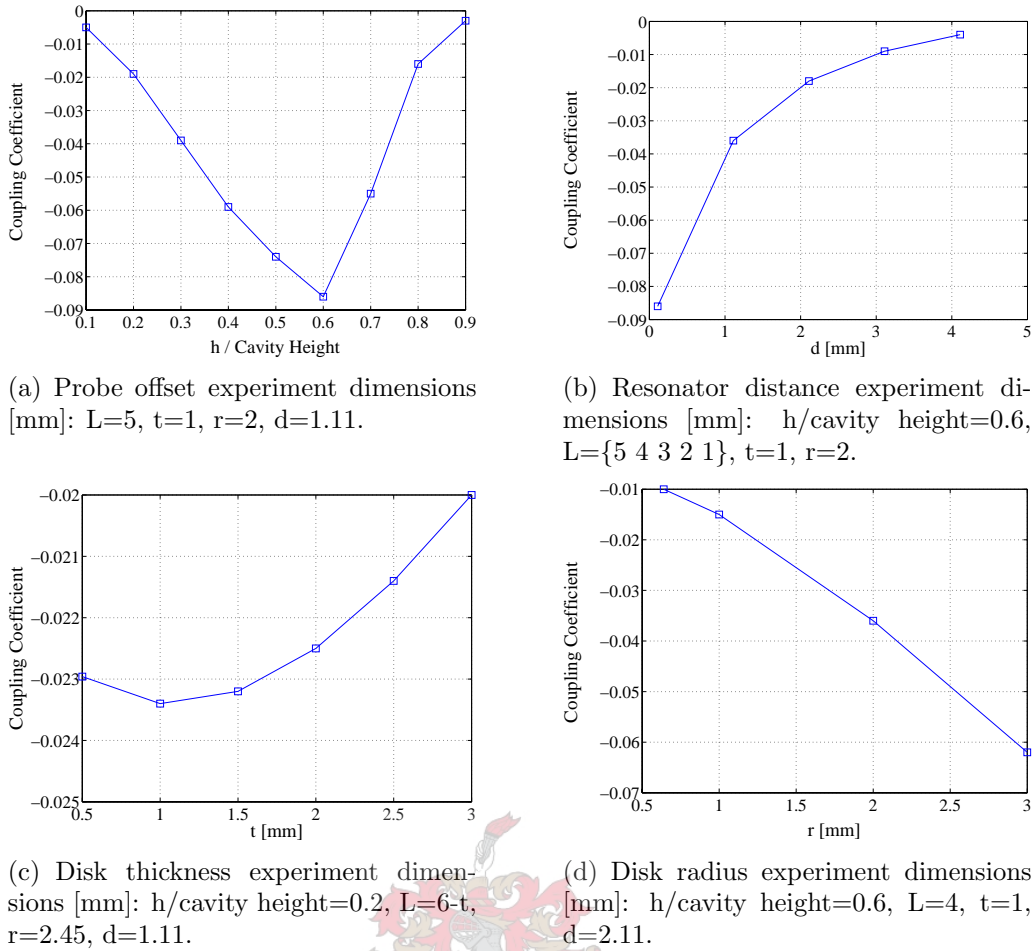


Fig. 4.28. Coupling coefficient as a function of capacitive probe parameters.

The price to pay for the large range of negative coupling, is the extreme sensitivity of the coupling value to the physical parameters, and the relative difficulty with which the structure is manufactured, due to the extension of a thin centre conductor and the attachment of small disks at its ends. Additionally, this coupling mechanism is not tunable after its construction.

## 4.5 Port Impedance Transformation

In order for a coupled resonator filter to function correctly, it has to see a certain source and load impedance at its terminals. As illustrated in Fig. 2.3, in a normalised system, the source and load impedance of  $1\ \Omega$  must transform to  $n_1^2$  and  $n_2^2$ , respectively. For symmetrical networks,  $n_1 = n_2 = n$ . After applying the necessary bandwidth, frequency and impedance scaling (illustrated in Appendix A), the required source and load impedances are equal to

$$R = BZ_0n^2 \quad (4.30)$$

with  $B$  the fractional bandwidth and  $Z_0$  the filter characteristic impedance. For this application,  $B = 0.03$ ,  $Z_0 = 77\ \Omega$  and  $n^2 = 1.069$ , which leads to  $R = 2.47\ \Omega$ . Con-

sidering that the source and load design impedances are  $50 \Omega$ , some form of impedance transformation is needed, as illustrated in Fig. 4.29.

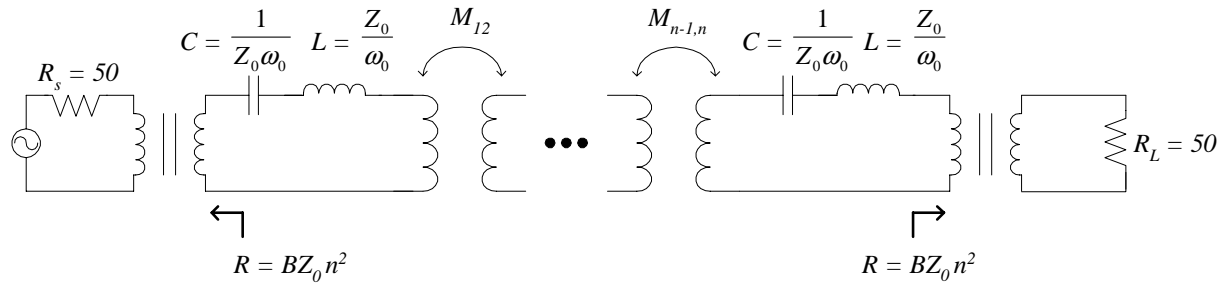


Fig. 4.29. Coupled resonator filter in a  $50 \Omega$  environment.

### 4.5.1 Inductance in the Feed Structure

For the current implementation, the transformation will be achieved by extending the centre conductor of the feed line into the cavity and attaching it to the resonator post at a certain height. As this seems like one is ‘tapping’ into the filter, this type of feed is called a tap point design. An illustration of this feed structure is given in Fig. 4.30.

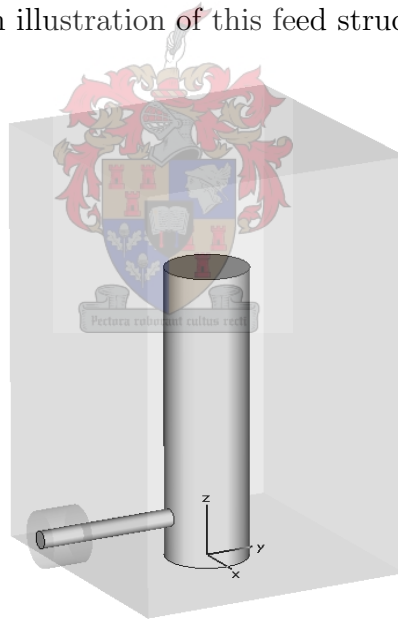


Fig. 4.30. A single coaxial resonator cavity with tapped feed line.

The loaded or external Q-factor of the filter relates the reactance slope parameter  $x$  to the required source resistance  $R$  [17, p.430]. By using eqn. 4.4 and eqn. 4.30, with  $L = Z_0/\omega_0$ , the required external Q-factor can be determined.

$$\begin{aligned}
 Q_e &= \frac{x}{R} \\
 &= \frac{\omega_0 L}{R} \\
 &= \frac{\omega_0 \left( \frac{Z_0}{\omega_0} \right)}{B Z_0 n^2} \\
 &= \frac{1}{B n^2}
 \end{aligned} \tag{4.31}$$

For the current application,  $Q_e = 31.18$ .

In order to gain some understanding in the practical implications of the tap point positioning, the height of the tap points in a two-cavity second order design was adjusted from very close to the short-circuited end to the open end of the resonator post. Alteration of the feed position causes the filter response to change. It is, however, possible to optimise the system impedance to a value where the analysis yields the correct response and bandwidth, which means that the external Q-factor has the required value. By repeating this optimisation procedure for various tap positions, it was found that the closer the tap point is placed to the short-circuited end of the resonator post, the higher the system impedance has to be for a constant  $Q_e$ . This is counter-intuitive, as one would expect the system impedance to decrease as it approaches a short circuit.

The reason for this behaviour lies in the non-negligible inductance of the extended centre conductor. Consider the equivalent circuit of the feed and first resonator in Fig. 4.31.

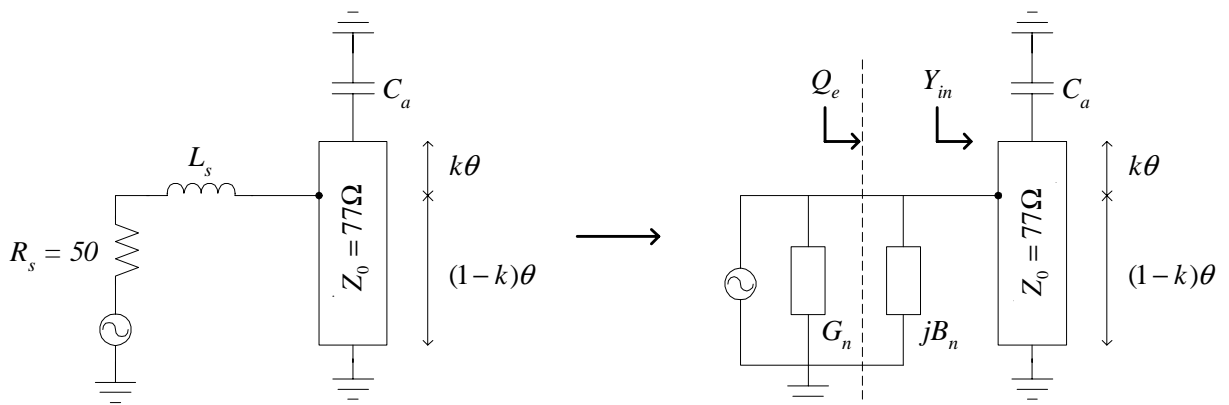


Fig. 4.31. Inductance in the feed structure.

In order to find an expression for the capacitance between the end of the resonator post and the cavity wall, one simply enforces the condition for resonance, which is zero total admittance of the capacitor  $C_a$  and short-circuited transmission line at the centre frequency  $\omega_0$ .

$$\begin{aligned}
Y_{sc} + Y_{cap} &= 0 \\
\frac{Y_0}{j \tan(\theta_0)} + j\omega_0 C_a &= 0 \\
\Rightarrow C_a &= \frac{Y_0 \cot(\theta_0)}{\omega_0} \\
\Rightarrow \omega C_a &= \frac{\omega Y_0 \cot(\theta_0)}{\omega_0} \\
&= \frac{\theta Y_0 \cot(\theta_0)}{\theta_0}
\end{aligned} \tag{4.32}$$

Next, the parallel equivalent of the feed and source is determined.

$$\begin{aligned}
Z_s &= R_s + j\omega L_s \\
\Rightarrow Y_s &= \frac{1}{R_s + j\omega L_s} \\
&= \frac{R_s - j\omega L_s}{R_s^2 + (\omega L_s)^2} \\
&= G_n + jB_n
\end{aligned} \tag{4.33}$$

In order to find  $Q_e$ , one also needs the input admittance  $Y_{in}$  of the resonator at the feed connection point. For the section of short-circuited transmission line seen from the feed point, the input admittance is

$$Y_{sc2} = \frac{Y_0}{j \tan(1-k)\theta} \tag{4.34}$$

For the section of transmission line terminated in a capacitor  $C_a$ , the input impedance is

$$\begin{aligned}
Z_{cl} &= Z_0 \frac{Z_c + jZ_0 \tan(k\theta)}{Z_0 + jZ_c \tan(k\theta)} \\
\Rightarrow Y_{cl} &= Y_0 \frac{Z_0 + jZ_c \tan(k\theta)}{Z_c + jZ_0 \tan(k\theta)}
\end{aligned} \tag{4.35}$$

with

$$Z_c = \frac{1}{j\omega C_a}$$

Using eqns. 4.34 and 4.35, this leads to a total input admittance at the feed point of

$$\begin{aligned}
Y_{in} &= Y_{sc2} + Y_{cl} \\
&= -jY_0 \left[ \frac{Z_0 \tan(k\theta) - \frac{1}{\omega C_a} + Z_0 \tan(1-k)\theta + \frac{1}{\omega C_a} \tan(k\theta) \tan(1-k)\theta}{\tan(1-k)\theta \left[ Z_0 \tan(k\theta) - \frac{1}{\omega C_a} \right]} \right]
\end{aligned} \tag{4.36}$$

With  $Y_{in} = jB_{in}$ , the external Q-factor of the parallel resonator can now be determined.

$$Q_e = \frac{b}{G_n} \tag{4.37}$$



with

$$b = \frac{\omega_0}{2} \left. \frac{dB}{d\omega} \right|_{\omega_0} \quad (4.38)$$

and

$$B = B_n + B_{in} \quad (4.39)$$

as illustrated in Fig. 4.31. By including  $B_n$  in the susceptance term of eqn. 4.39, one is including the effect of the feed inductance in the Q-factor calculation. With  $\omega = \theta/T$  and  $\frac{dB}{d\omega} = \frac{dB}{d\theta} \frac{d\theta}{d\omega} = \frac{dB}{d\theta} T$ ,

$$\begin{aligned} b &= \frac{\theta_0}{2T} T \left. \frac{dB}{d\theta} \right|_{\theta_0} \\ &= \frac{\theta_0}{2} \left. \frac{dB}{d\theta} \right|_{\theta_0} \end{aligned} \quad (4.40)$$

By writing  $B$  completely in terms of  $\theta$  and applying numerical differentiation with respect to  $\theta$ ,  $Q_e$  can be determined for a specific value of tap position  $k$ . Fig. 4.32 illustrates the variation of  $Q_e$ , as calculated with different tap positions.  $k = 0$  corresponds to the open end of the resonator post.

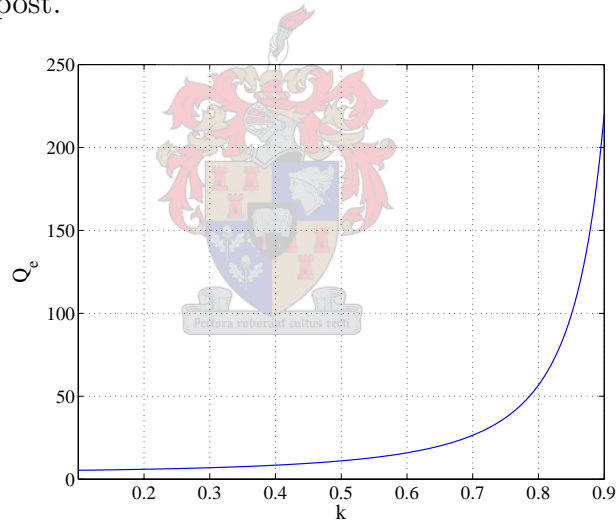


Fig. 4.32. External Q-factor versus feed tap position. Dimensions of Fig. 4.9 [mm]:  $a=6$ ,  $b=20.22$ ,  $H=30$ ,  $l=21.08$ .

For the structure under consideration, calculations yield the following results:

- $Q_e$  increases as the feed point moves closer to the short-circuited end of the resonator post.
- $b$  increases with  $k$ . This is the case for various different values of  $L_s$ .

If one assumes that the feed inductance is negligible,  $\omega_0 L_s \ll R_s$ . Referring to eqn. 4.33 and eqn. 4.37,

$$G_n \simeq \frac{1}{R_s}$$

and

$$Q_e \simeq bR_s$$

For constant  $Q_e$ ,  $R_s$  thus has to decrease as  $k$  increases. This is consistent with one's initial expectation of a decrease in system impedance as the tap point approaches the short-circuited end of the resonator post.

Conversely, consider the case where the feed inductance is not negligible, with  $\omega_0 L_s \gg R_s$ . In this case, eqn. 4.33 and eqn. 4.37 can be approximated as

$$G_n \simeq \frac{R_s}{(\omega_0 L_s)^2}$$

and

$$Q_e \simeq b \frac{(\omega_0 L_s)^2}{R_s}$$

For constant  $Q_e$ ,  $R_s$  therefore has to increase as  $k$  increases. This is exactly what was found for the structure under consideration. Consequently, it is clear that the feed inductance plays an important part in the filter operation.

## 4.5.2 Measurement of the External Q-factor

In order to complete the feed design, a method is needed by which one can measure the external Q-factor from a simulation or measurement of the physical structure. Williams [24] suggested a way of doing this, based on the model of a single cavity series resonator shown in Fig. 4.33.

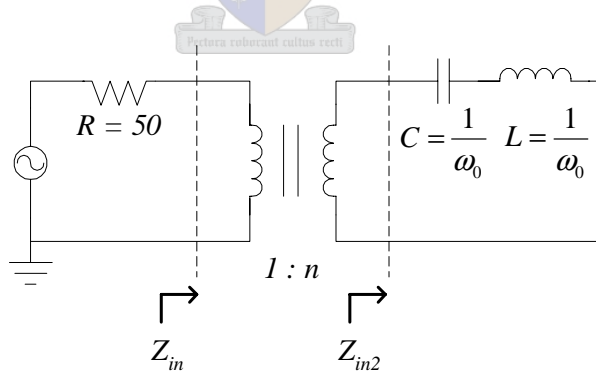


Fig. 4.33. Single cavity resonator and feed.

By relating the impedances across the transformer,

$$Z_{in2} = n^2 Z_{in} \quad (4.41)$$

$$R_s = n^2 R \quad (4.42)$$

From the definition of the reflection coefficient,

$$\begin{aligned} S_{11} &= \frac{Z_{in} - R}{Z_{in} + R} \times \frac{n^2}{n^2} \\ &= \frac{Z_{in2} - R_s}{Z_{in2} + R_s} \end{aligned} \quad (4.43)$$

Assume  $S_{11} = \pm j$ . Then,

$$\begin{aligned} Z_{in2} - R_s &= \pm j (Z_{in2} + R_s) \\ \Rightarrow Z_{in2} (1 \mp j) &= R_s (1 \pm j) \end{aligned} \quad (4.44)$$

This reduces to

$$Z_{in2} = \pm j R_s \quad (4.45)$$

In terms of the  $LC$  circuit,

$$\begin{aligned} Z_{in2} &= j \left( \frac{\omega}{\omega_0} - \frac{\omega_0}{\omega} \right) \\ &= j\lambda \end{aligned} \quad (4.46)$$

Therefore, at the  $-90^\circ$  and  $-270^\circ$  frequencies of  $S_{11}$ ,

$$\lambda_r = \pm R_s$$

and

$$\begin{aligned} \lambda_{r2} - \lambda_{r1} &= 2R_s \\ &= \underbrace{\frac{1}{\omega_0} (\omega_{r2} - \omega_{r1})}_{t_1} - \omega_0 \underbrace{\left( \frac{1}{\omega_{r2}} - \frac{1}{\omega_{r1}} \right)}_{t_2} \end{aligned} \quad (4.47)$$

Numerically,  $t_1 \approx t_2$ . This allows a simple expression to be used for  $R_s$ .

$$R_s \approx \frac{\omega_{r2} - \omega_{r1}}{\omega_0}$$

which leads to

$$Q_e = \frac{\omega_0 L}{R_s} = \frac{1}{R_s} = \frac{\omega_0}{\omega_{r2} - \omega_{r1}} \quad (4.48)$$

with  $\omega_0 = \omega(-180^\circ)$ ,  $\omega_{r1} = \omega(-90^\circ)$  and  $\omega_{r2} = \omega(-270^\circ)$  of  $S_{11}$ .

By therefore measuring the phase of  $S_{11}$  for a single cavity and feed structure, it is possible to determine the external Q-factor of the circuit. However, this derivation applies to series resonators, while the current realisation requires parallel resonators. More importantly, eqn. 4.46 does not take the effect of the feed inductance on the phase response into account.

The parallel realisation does not really pose a problem. The above derivation can be repeated for the case of a single parallel resonator, which results in

$$Q_e = \frac{\omega_0 C}{G_s} = \frac{1}{G_s} = \frac{\omega_0}{\omega_{r2} - \omega_{r1}} \quad (4.49)$$

with  $\omega_0 = \omega(0^\circ)$ ,  $\omega_{r1} = \omega(90^\circ)$  and  $\omega_{r2} = \omega(-90^\circ)$  of  $S_{11}$ .

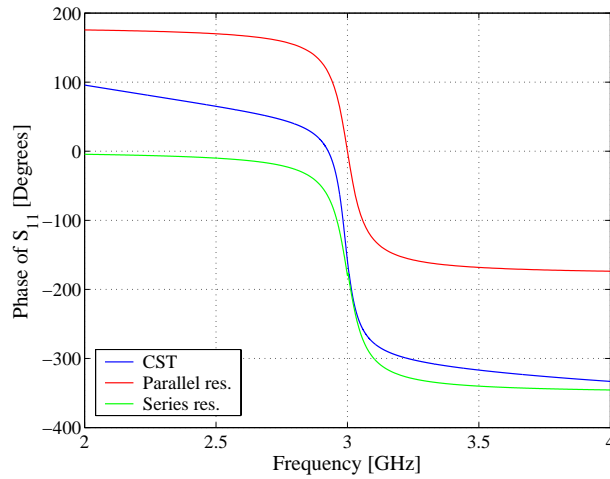


Fig. 4.34. Comparison of  $S_{11}$  phase of a single coaxial resonator with tapped feed, an ideal parallel resonator and an ideal series resonator.

Fig. 4.34 shows the plots of the angle of  $S_{11}$  for three single cavities.

The case of the ideal series resonator shows how (in a Microwave Office simulation) the phase goes to zero at frequencies far from the centre frequency, where the circuit behaves like an open circuit. The phase of the ideal parallel resonator goes to  $180^\circ$  far from the centre frequency, where the circuit behaves like a short circuit. Comparing the gradient of  $\angle S_{11}$  in the CST simulation at low and high frequencies, it is clear that this gradient varies with frequency. Accordingly, one cannot simply cancel the effect of the feed by adding an opposite linear phase term to the phase of  $S_{11}$ . Additionally, the structure does not behave like a pure series or parallel resonator, which makes the direct application of Williams's theory meaningless. New theory, which takes the feed inductance into account, is therefore needed for the measurement of the external Q-factor.

Consider the more complete model of a single parallel resonator with non-negligible feed inductance in Fig. 4.35.

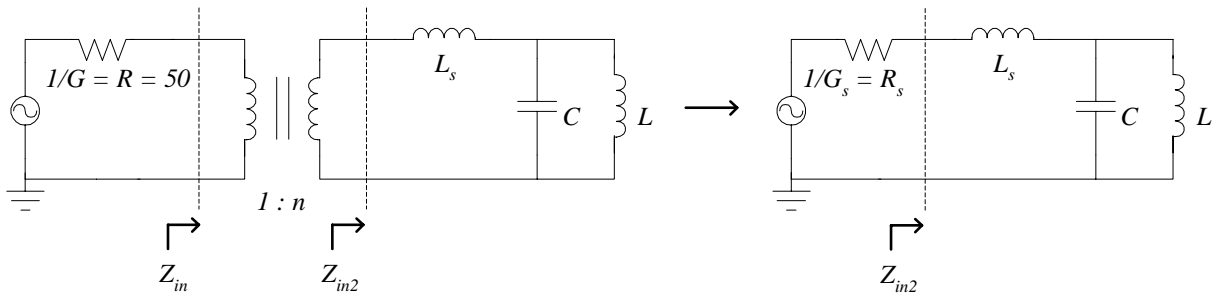


Fig. 4.35. Model of a single parallel  $LC$  resonator with feed inductance  $L_s$ .

As before,

$$Z_{in2} = n^2 Z_{in} \quad (4.50)$$

and

$$R_s = n^2 R \quad (4.51)$$

The reflection coefficient is defined as

$$\begin{aligned} S_{11} &= \frac{Z_{in2} - R_s}{Z_{in2} + R_s} \\ &= \frac{G_s - Y_{in2}}{G_s + Y_{in2}} \end{aligned} \quad (4.52)$$

with  $G_s = 1/R_s$  and  $Y_{in2} = 1/Z_{in2}$ .

If  $S_{11} = \pm j$ , eqn. 4.52 reduces to

$$Y_{in2} = \pm jG_s \quad (4.53)$$

By defining  $\omega_{01}$  as  $\omega(0^\circ)$ , the frequency where the parallel combination of  $L$  and  $C$  resonates, it is possible to choose the values of  $L$  and  $C$ .

$$L = C = \frac{1}{\omega_{01}} \quad (4.54)$$

With  $L_s$  still unknown, the expression for  $Y_{in2}$  is

$$\begin{aligned} Y_{in2} &= \frac{\left(\frac{1}{j\omega L_s}\right) j \left(\frac{\omega}{\omega_{01}} - \frac{\omega_{01}}{\omega}\right)}{\frac{1}{j\omega L_s} + j \left(\frac{\omega}{\omega_{01}} - \frac{\omega_{01}}{\omega}\right)} \\ &= \frac{\frac{1}{\omega L_s} \left(\frac{\omega_{01}}{\omega} - \frac{\omega}{\omega_{01}}\right)}{j \frac{\omega}{\omega_{01}} - \frac{1}{\omega} - \frac{1}{\omega L_s}} \end{aligned} \quad (4.55)$$

Comparing eqns. 4.53 and 4.55, it follows that at  $\omega_{r1}$  and  $\omega_{r2}$  (the  $-90^\circ$  and  $-270^\circ$  frequencies of  $S_{11}$ ),  $Y_{in2}$  is equal to  $\pm G_s$ . This criterion can be used to determine the value of  $L_s$ .

$$\frac{\frac{1}{\omega_{r2} L_s} \left(\frac{\omega_{01}}{\omega_{r2}} - \frac{\omega_{r2}}{\omega_{01}}\right)}{\frac{\omega_{r2}}{\omega_{01}} - \frac{\omega_{01}}{\omega_{r2}} - \frac{1}{\omega_{r2} L_s}} = -\frac{\frac{1}{\omega_{r1} L_s} \left(\frac{\omega_{01}}{\omega_{r1}} - \frac{\omega_{r1}}{\omega_{01}}\right)}{\frac{\omega_{r1}}{\omega_{01}} - \frac{\omega_{01}}{\omega_{r1}} - \frac{1}{\omega_{r1} L_s}} \quad (4.56)$$

With  $D_1 = \left(\frac{\omega_{01}}{\omega_{r1}} - \frac{\omega_{r1}}{\omega_{01}}\right)$  and  $D_2 = \left(\frac{\omega_{01}}{\omega_{r2}} - \frac{\omega_{r2}}{\omega_{01}}\right)$ , eqn. 4.56 can be solved for  $L_s$ .

$$L_s = -\frac{D_1 + D_2}{D_1 D_2 (\omega_{r1} + \omega_{r2})} \quad (4.57)$$

Substitution of  $L_s$  into eqn. 4.56 makes it possible to solve  $G_s$ .

$$G_s = \frac{\frac{1}{\omega_{r2} L_s} D_2}{-D_2 - \frac{1}{\omega_{r2} L_s}} \quad (4.58)$$

Referring to Fig. 4.35, these are the values of transformed feed inductance and source conductance which, together with the chosen values of  $L$  and  $C$ , result in the best possible approximation of the measured phase response.

At this stage, all the element values in the model of Fig. 4.35 have been solved from the measured phase of  $S_{11}$ . In order to determine  $Q_e$ , the model has to be transformed to a circuit consisting entirely of parallel elements, as this is what the definition of the Q-factor requires. Define  $Z_s$  as

$$Z_s = R_s + j\omega L_s \quad (4.59)$$

Then,

$$\begin{aligned} Y_s &= 1/Z_s \\ &= \frac{R_s - j\omega L_s}{R_s^2 + (\omega L_s)^2} \\ &= G_n + jB_n \\ &= G_n - j\frac{1}{\omega L_n} \end{aligned} \quad (4.60)$$

It follows that

$$G_n = \frac{R_s}{R_s^2 + (\omega L_s)^2} \quad (4.61)$$

and

$$L_n = \frac{R_s^2 + (\omega L_s)^2}{\omega^2 L_s} \quad (4.62)$$

The transformed model is shown in Fig. 4.36, with  $L$  and  $C$  unchanged. The value of  $L_n$  is approximated as the value of eqn. 4.62 evaluated at  $\omega_{01}$ .

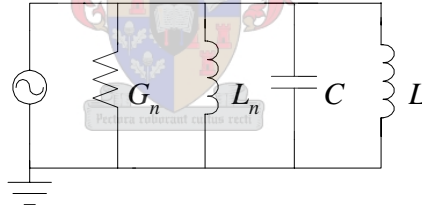


Fig. 4.36. Transformed model of a single parallel resonator with feed inductance.

In order to determine the new resonant frequency, the total inductance of the circuit must be determined.

$$L_t = \frac{L_n L}{L_n + L} \quad (4.63)$$

Subsequently,

$$\omega_{02} = \frac{1}{\sqrt{L_t C}} \quad (4.64)$$

and

$$C' = \frac{1}{\omega_{02}^2} \quad (4.65)$$

where  $C'$  is defined as the capacitance of a hypothetical parallel  $LC$  combination which would yield a resonant frequency of  $\omega_{02}$ .

From the definition of  $Q_e$  for a parallel resonator,

$$\begin{aligned}
 Q_e &= \frac{\omega_{02} C'}{G_n} \\
 &= \frac{1}{G_n} \\
 &= \frac{R_s^2 + (\omega_{02} L_s)^2}{R_s}
 \end{aligned} \tag{4.66}$$

By implementing this procedure, the position of the tap point can be optimised in order to yield the desired external Q-factor.

## 4.6 Realisation of Coupling Matrix Diagonal Entries

Application of the techniques described in Chapter 2 and 3 leads to the construction of a normalised coupling matrix. After applying the necessary frequency and bandwidth scaling (described in Appendix A), it is possible to relate the individual resonant frequency of each cavity to the diagonal entries in the coupling matrix. The filter centre frequency is defined as  $\omega_0$ , while the  $i^{\text{th}}$  individual resonant frequency is defined as  $\omega_i = 1/\sqrt{L_i C_i}$ . As before,  $Z_0 = \sqrt{L_i/C_i}$  is the characteristic impedance of the filter. As a starting point, consider the impedance matrix introduced in Chapter 2, which relates the loop currents and nodal voltages of the equivalent coupled resonator circuit. For the sake of convenience, eqn. 2.2 is duplicated below.

$$\begin{bmatrix} e_1 \\ 0 \\ 0 \\ \cdot \\ \cdot \\ 0 \\ -e_n \end{bmatrix} = \begin{bmatrix} S & -jM_{12} & -jM_{13} & \cdots & \cdot & -jM_{1n} \\ -jM_{12} & S & -jM_{23} & \cdots & \cdot & -jM_{2n} \\ -jM_{13} & -jM_{23} & S & \cdots & \cdot & \cdot \\ \cdot & \cdot & \cdot & \cdots & \cdot & \cdot \\ \cdot & \cdot & \cdot & \cdots & \cdot & \cdot \\ \cdot & \cdot & \cdot & \cdots & S & -jM_{n-1,n} \\ -jM_{1n} & \cdot & \cdot & \cdots & -jM_{n-1,n} & S \end{bmatrix} \cdot \begin{bmatrix} i_1 \\ i_2 \\ i_3 \\ \cdot \\ \cdot \\ i_{n-1} \\ i_n \end{bmatrix} \tag{4.67}$$

with

$$\begin{aligned}
 S &= Z_L + Z_C \\
 &= j\omega L_i - j\frac{1}{\omega C_i}
 \end{aligned} \tag{4.68}$$

In order to obtain the coupling matrix, the impedance matrix of eqn. 4.67 is factorised as follows.

$$\mathbf{Z} = -j \begin{bmatrix} -\omega L_1 + 1/\omega C_1 & M_{12} & M_{13} & \cdots & M_{1n} \\ M_{12} & -\omega L_2 + 1/\omega C_2 & M_{23} & \cdots & M_{2n} \\ M_{13} & M_{23} & \cdot & \cdots & \cdot \\ \cdot & \cdot & \cdot & \cdots & \cdot \\ \cdot & \cdot & \cdot & \cdots & M_{n-1,n} \\ M_{1n} & \cdot & \cdot & \cdots & -\omega L_n + 1/\omega C_n \end{bmatrix} \quad (4.69)$$

Accordingly, if one should consider resonator  $i$  at the filter centre frequency,

$$\begin{aligned} M_{ii} &= -\omega_0 L_i + \frac{1}{\omega_0 C_i} \\ \Rightarrow -M_{ii} &= \omega_0 L_i - \frac{\omega_i^2 L_i}{\omega_0} \\ \Rightarrow \frac{-M_{ii}}{Z_0} &= \frac{\omega_0}{\omega_i} - \frac{\omega_i}{\omega_0} \\ \Rightarrow 0 &= \omega_0^2 + \left( \frac{\omega_i M_{ii}}{Z_0} \right) \omega_0 - \omega_i^2 \end{aligned}$$

Next, it is possible to find the roots of  $\omega_0$  by applying the formula for a quadratic equation.

$$\frac{\omega_0}{\omega_i} = \frac{-M_{ii}}{2Z_0} \pm \sqrt{\left( \frac{M_{ii}}{2Z_0} \right)^2 + 1} \quad (4.70)$$

By choosing only the positive frequencies, the  $i^{\text{th}}$  resonant frequency can be calculated as

$$\omega_i = \frac{\omega_0}{\frac{-M_{ii}}{2Z_0} + \sqrt{\left( \frac{M_{ii}}{2Z_0} \right)^2 + 1}}. \quad (4.71)$$

## 4.7 Conclusion

In this chapter, the most important aspects related to the physical implementation of the coupling matrix were discussed. It was discovered that the size of the coaxial resonators and inductance associated with the tapped feed play important roles in the operation of the coupled resonator filter. Various coupling mechanisms and their limitations were also investigated and compared. Negative iris coupling was found to have quite a big limitation in size and range, while negative evanescent mode coupling creates a small spurious pass band which moves closer to the real pass band for certain smaller element values. Capacitive probe coupling yields a useful range of negative coupling values, but proves to be quite sensitive with regards to the probe dimensions. In order to measure the external Q-factor of a tapped feed structure, Williams's theory was adapted to take the non-negligible feed inductance into account. Finally, a relation was developed between the coupling matrix diagonal entries and individual resonator centre frequencies.



# Chapter 5

## Parameter Extraction from Simulation and Measurements

### 5.1 Introduction

An essential part of the coupled resonator filter design process is the extraction of coupling values and resonant frequencies from the structure under consideration. Although it has been shown in Section 4.3 that the coupling value between two cavities can be determined accurately from the simulated resonant frequencies of the characteristic modes, a method for determining the coupling values and resonant frequencies of the entire structure is essential, as these values are altered when the whole structure is assembled. For filters of a higher order or narrow bandwidth, even a slightly detuned resonant frequency or coupling value can change the performance of the filter. This is especially the case when the design contains cross coupling. The process of alternating filter response evaluation and adjustment of the filter coupling values and resonant frequencies is known as tuning, and parameter extraction is a vital aid in this process. However, no parameter in a high performance microwave filter is entirely isolated. This has made the tuning of these devices a non-trivial, time-consuming and expensive task, which is often described to be as much of an art as a science. The aim of many researchers in the field of parameter extraction is therefore to automate this process, and make the tuning of filter units on the production floor a reality. As a worst case scenario, parameter extraction is used as a troubleshooting tool to determine why a filter does not work well, or at all.

In this chapter, some of the parameter extraction and tuning methods employed over the past two decades will be summarised and evaluated in terms of their applications and restrictions.

## 5.2 Extraction with a Short-Circuited Final Cavity

In order to address the issue of parameter extraction, Atia and Williams proposed a method in 1975 which uses the finely sampled  $S_{11}$  phase measurement performed on a coupled resonator filter with a short-circuited final cavity [25, 24]. This is discussed in Section 5.2.1. Atia and Yao refined the technique with the implementation of recursive equations [26], as described in Section 5.2.2. Hsu *et al.* added more functionality to the parameter extraction of Atia and Yao by introducing a method which removes the loading effect of the short circuited final cavity, and by providing a deterministic tuning method which allows an  $n$ -resonator direct-coupled filter to be tuned within  $(2n - 1)$  steps [27]. This is the topic of Section 5.2.3. An alternative procedure which expresses the coupling values in terms of the group delay of  $S_{11}$  was first introduced by Ness [28], and is described in Section 5.2.4.

### 5.2.1 Coupling Coefficients from $\angle S_{11}$

This section will outline the parameter extraction method presented in [25]. The method is based on the fundamental theory of narrow band coupled resonator synthesis, laid out in Chapter 2. Consider the general equivalent circuit of  $n$  coupled cavities with the final resonant cavity terminated in a short circuit in Fig. 5.1.

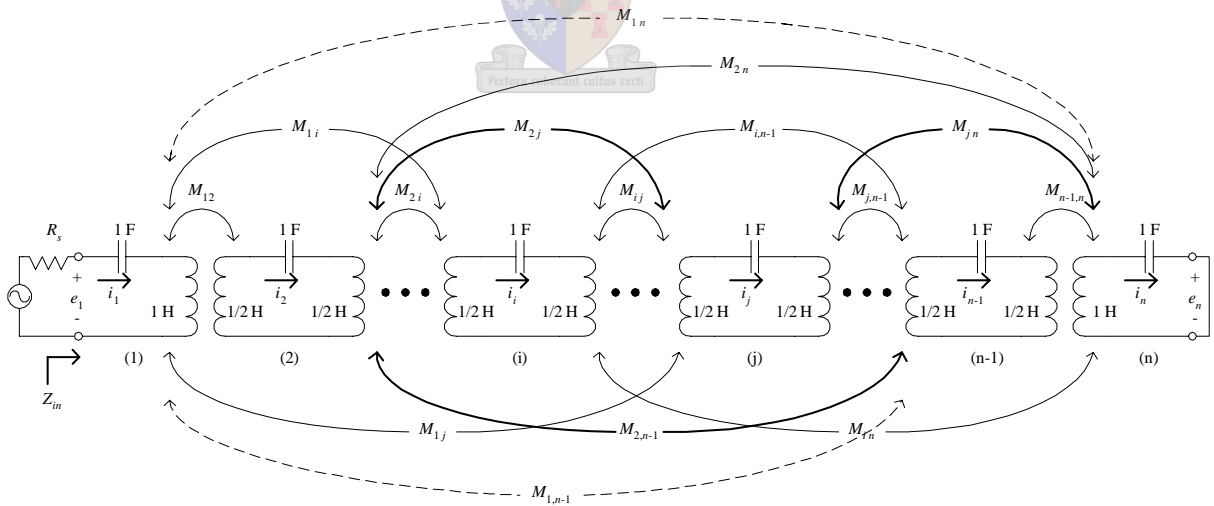


Fig. 5.1. Equivalent circuit of  $n$  coupled cavities.

For this circuit,

$$\begin{aligned}
 y_{11} &= \left. \frac{i_1}{e_1} \right|_{e_n=0} \\
 &= \mathbf{Z}_{11}^{-1} \\
 &= \frac{C_{11}}{\det(\mathbf{Z})}
 \end{aligned} \tag{5.1}$$

where  $\mathbf{Z}_{mn}^{-1}$  refers to the  $(m, n)^{\text{th}}$  component of the inverse of the impedance matrix, and  $C_{ij}$  is the cofactor of  $\mathbf{Z}$  [11, p.198]. Because the final cavity is terminated in a short circuit,  $y_{11} = Y_{in} = 1/Z_{in}$ . Therefore,

$$\begin{aligned} Z_{in} &= \frac{\det(\mathbf{Z})}{C_{11}} \\ &= \frac{\det(S\mathcal{I} - j\mathbf{M}_n)}{\det(S\mathcal{I} - j\mathbf{M}_{n-1})} \end{aligned} \quad (5.2)$$

$\mathbf{M}_{n-1}$  is the matrix resulting from the deletion of the first row and column of the coupling matrix  $\mathbf{M}_n$  and  $S = j\lambda = j\left(\frac{\omega}{\omega_0} - \frac{\omega_0}{\omega}\right)$  with  $\omega_0 = 2\pi f_0$  the centre frequency. Also,

$$S_{11} = \frac{Z_{in} - R_s}{Z_{in} + R_s} \quad (5.3)$$

Therefore,  $\angle S_{11} = 0^\circ$  represents a pole of  $Z_{in}$ , while  $\angle S_{11} = 180^\circ$  represents a zero of  $Z_{in}$ . To illustrate this procedure, consider the case of two coupled cavities ( $n = 2$ ). From eqn. 5.2,

$$\begin{aligned} Z_{in}(\omega) &= \frac{\det \begin{bmatrix} j\lambda & -jM_{12} \\ -jM_{12} & j\lambda \end{bmatrix}}{\det(j\lambda)} \\ &= j \frac{\lambda^2 - M_{12}^2}{\lambda} \end{aligned} \quad (5.4)$$

It is clear that the zeros of  $Z_{in}(\omega)$  exist at frequencies  $\lambda_z = \pm M_{12}$ , while the pole frequency of  $Z_{in}(\omega)$  is  $\lambda_p = 0$ . If one could therefore measure the pole and zero frequencies with enough accuracy, it would be possible to determine the coupling coefficient  $M_{12}$ . Numerically, the following approximation is valid.

$$\lambda = \left(\frac{\omega}{\omega_0} - \frac{\omega_0}{\omega}\right) \simeq \frac{2}{\omega_0}(\omega - \omega_0) \quad (5.5)$$

It follows that

$$\begin{aligned} 2M_{12} &= \lambda_{z2} - \lambda_{z1} \\ &\simeq \frac{2}{\omega_0}(\omega_{z2} - \omega_0) - \frac{2}{\omega_0}(\omega_{z1} - \omega_0) \\ &= \frac{2}{\omega_0}(\omega_{z2} - \omega_{z1}) \end{aligned} \quad (5.6)$$

with  $\omega_{z1}$  and  $\omega_{z2}$  the frequencies of the first and second zeros of  $Z_{in}$  respectively, and  $\omega_0$  the centre frequency. This leads to a convenient expression for the coupling coefficient in eqn. 5.7, with  $\omega_0 = \omega_p$ .

$$M_{12} = \frac{\omega_{z2} - \omega_{z1}}{\omega_0} \quad (5.7)$$

A typical phase response of an ideal second order series resonator with centre frequency 3 GHz, together with the location of the two zeros and one pole, is illustrated in Fig. 5.2.

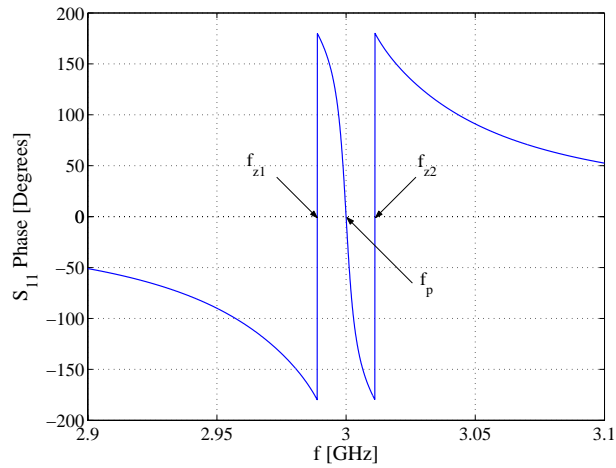


Fig. 5.2. Phase response of a short-circuited set of two coupled series resonators.

It is possible to determine the coupling values in the general case of  $n$  cavities. However, this solution may not be unique. After constructing the M-matrix, the specific coupling values can be obtained by reducing the diagonal elements to zero, together with the off-diagonal elements which were designed to be zero. This is done by performing similarity transforms, as discussed in [8]. Although the theory has been derived for series resonators, it is possible to repeat the process with the dual circuit of parallel resonators and an open-circuited final cavity. The only difference in the results is the interchange of the pole and zero frequency positions. For example, the phase response of a second order parallel resonator filter is illustrated in Fig. 5.3.

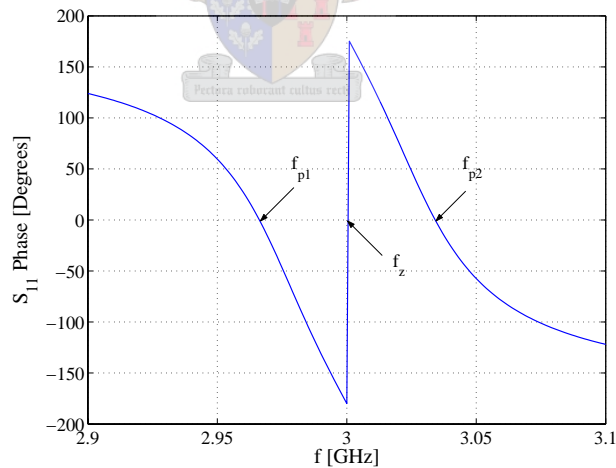


Fig. 5.3. Phase response of an open-circuited set of two coupled parallel resonators.

Subsequently, the coupling coefficient for a second order filter with parallel resonators can be calculated as

$$M_{12} = \frac{\omega_{p2} - \omega_{p1}}{\omega_z} \quad (5.8)$$

## Applications and Restrictions

The application of this extraction method is limited to direct-coupled filters with no centre frequency offsets. If cross couplings are indeed present in the filter under consideration, it should be removed by detuning the resonators in the cross-coupled path. As the phase response varies quickly in the region of the centre frequency, substantial measurement resolution is required. For example, for a fourth order filter at 3 GHz, 100 data points are measured for every 5 MHz. In terms of accuracy, there is a limitation on the smallest coupling value that can be measured, due to the effect of a finite loaded Q-factor in practical filters. As a general rule, to obtain an error of smaller than 0.5%,  $M \geq 10/Q$ .

For the chosen filter realisation, illustrated in Chapter 4, the tapped feed possesses non-negligible series inductance ( $L_f$ ) in the extended centre conductor, and also parallel capacitance ( $C_f$ ) between the centre conductor and the grounded cavity walls. Consequently, the phase response differs quite notably from the ideal response of a structure without feed inductance and capacitance. This is confirmed with a Microwave Office simulation in Fig. 5.4. Typical values for  $L_f$  and  $C_f$  are calculated in Section 5.3.3.

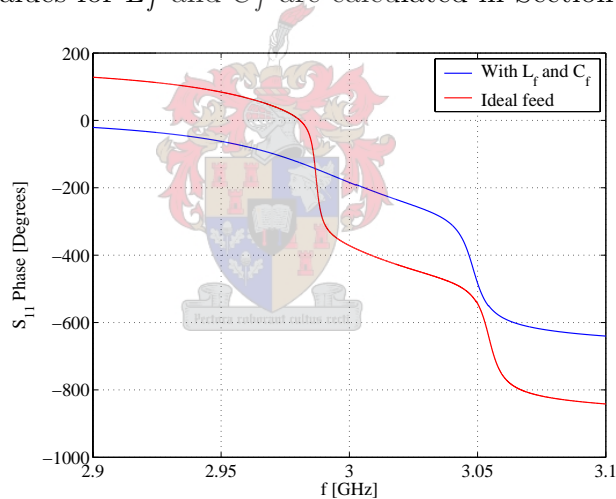


Fig. 5.4. Phase response of 3 parallel coupled resonators, terminated in an open circuit, with and without a complex feed structure.

From Fig. 5.4 it is clear that the coupling values calculated by using the two phase responses will differ. This is not correct, as both filters use the same coupling structures and only differ in their feed mechanisms. Therefore, although this method is easy to implement and could be useful for simple filters, it cannot be used for more complex filters which possess a phase response different from the ideal series or parallel response.

### 5.2.2 Computer-Aided Parameter Extraction from $\angle S_{11}$

The next parameter extraction method was introduced by Atia and Yao [26] and is an extension of the theory in Section 5.2.1. The essence of this procedure is a recursive

formula which takes the poles and zeros of a short-circuited set of coupled series resonators as its input, and yields the individual resonant frequencies, input coupling value and inter-cavity couplings as its output.

As in the previous section, the theory will be developed for the case of coupled series resonators. Consider a circuit with  $n$  cascaded direct-coupled resonators and a short-circuited  $n^{\text{th}}$  cavity in Fig. 5.5.

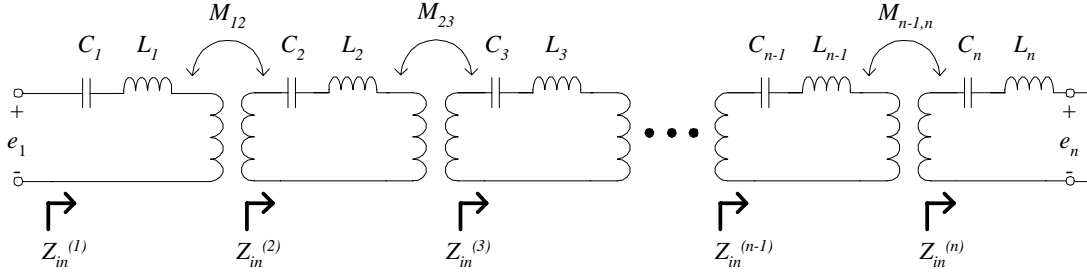


Fig. 5.5. Equivalent circuit representation of  $n$  cascaded coupled resonators.

For this circuit, the input impedance at loop  $i$  can be written as

$$Z_{in}^{(i)} = j \frac{Z_{0i} P_i(\omega^2)}{\omega \omega_{0i} Q_i(\omega^2)} \quad i = 1, 2 \dots n \quad (5.9)$$

$Z_{0i} = \sqrt{L_i/C_i}$  is the characteristic impedance and  $\omega_{0i} = 1/\sqrt{L_i C_i}$  is the resonant frequency of resonator  $i$ . The zeros of  $P_i(\omega^2)$  and  $Q_i(\omega^2)$  correspond to the zeros and poles of the input impedance of the one port network.

To start the process, the  $n - 1$  pole frequencies  $\omega_p^{(1)}$  (corresponding to the  $0^\circ$  frequencies of  $\angle S_{11}$ ) and the  $n$  zero frequencies  $\omega_z^{(1)}$  (corresponding to the  $180^\circ$  frequencies of  $\angle S_{11}$ ), as seen from the first resonator ( $i = 1$ ), are input to the following equations.

$$\begin{aligned} P_i(\omega^2) &= \prod_{t=1}^{n-i+1} (\omega^2 - \omega_{zt}^{(i)2}) \\ &= \sum_{t=0}^{n-i+1} c_t^{(i)} (\omega^2)^t \quad i = 1, 2 \dots n \end{aligned} \quad (5.10)$$

$$\begin{aligned} Q_i(\omega^2) &= \prod_{q=1}^{n-i} (\omega^2 - \omega_{pq}^{(i)2}) \\ &= \sum_{q=0}^{n-i} d_q^{(i)} (\omega^2)^q \quad i = 1, 2 \dots n \end{aligned} \quad (5.11)$$

$$\begin{aligned}
\omega_{0i}^2 &= \frac{\prod_{t=1}^{n-i+1} \omega_{zt}^{(i)2}}{n-i} \\
&= -\frac{c_o^{(i)}}{d_o^{(i)}} \quad i = 1, 2 \dots n
\end{aligned} \tag{5.12}$$

$$\begin{aligned}
m_{i,i+1}^2 &= \sum_{t=1}^{n-i+1} \omega_{zt}^{(i)2} - \sum_{q=1}^{n-i} \omega_{pq}^{(i)2} - \omega_{0i}^2 \\
&= d_{n-i-1}^{(i)} - c_{n-i}^{(i)} - \omega_{0i}^2 \quad i = 1, 2 \dots n-1
\end{aligned} \tag{5.13}$$

In eqn. 5.13,  $m_{i,i+1}$  is defined as the coupling bandwidth. The relation to the coupling coefficient  $k_{i,i+1}$  is given in eqn. 5.14.

$$m_{i,i+1}^2 = \omega_{0i} \omega_{0,i+1} k_{i,i+1}^2 \tag{5.14}$$

The following recursive equations are then used to solve  $P_{i+1}$  and  $Q_{i+1}$ .

$$P_{i+1}(\omega^2) = Q_i(\omega^2) \quad i = 1, 2 \dots n-1 \tag{5.15}$$

$$m_{i,i+1}^2 \omega^2 Q_{i+1}(\omega^2) = (\omega^2 - \omega_{0i}^2) P_{i+1}(\omega^2) - P_i(\omega^2) \quad i = 1, 2 \dots n-1 \tag{5.16}$$

Now, it is possible to increment  $i$  and find the next resonant frequency and coupling value by using eqns. 5.10 to 5.13. This process is repeated until all the resonant frequencies and coupling values have been solved.

The input coupling  $R_1$  can also be determined from the initial pole and zero frequencies.

$$\frac{\omega_{01} R_1}{Z_{01}} = \left| \frac{\prod_{t=1}^n (\omega_R^2 - \omega_{zt}^{(1)2})}{\omega_R \prod_{q=1}^{n-1} (\omega_R^2 - \omega_{pq}^{(1)2})} \right| \tag{5.17}$$

where  $\omega_R$  is the  $\pm 90^\circ$  frequency of the phase of  $S_{11}$ .

## Applications and Restrictions

This method, like the one described in Section 5.2.1, uses the phase response of cascaded coupled resonators without knowledge of the specific resonator characteristics, which makes it a useful general tool. Additionally, it is not restricted to series resonators. Parallel resonators are handled by replacing the short circuit in Fig. 5.5 with an

open circuit, and reversing the order in which the vectors  $\omega_p$  and  $\omega_z$  are input to the procedure. This essentially means the routine is receiving data for  $Y_{in}$  instead of  $Z_{in}$ , which corresponds to the parallel dual of the series network. The fact that the method can extract individual resonant frequencies which differ from the centre frequency, makes it an attractive option for the measurement and tuning of asymmetrical filters, which often require resonator frequency offsets.

Although cross couplings are not a problem, they cannot be handled by the method and must be removed by detuning the appropriate resonators. With regards to accuracy, random measurement error of the poles and zeros has a bigger effect on coupling values and resonant frequencies calculated later in the process when  $i$  approaches  $n$ . Additionally, the effect of these measurement errors increases with the number of resonators. The final set of restrictions pertain to complex feed structures, and correspond to those named in Section 5.2.1 — If the effect of the feed structure is to alter the phase response of the filter significantly, this method cannot be used for parameter extraction.

### 5.2.3 A Deterministic Tuning Procedure with $\angle S_{11}$

The methods described thus far have focused on the time-consuming process of iterative tuning and extraction of filter parameters from measurements, without providing a systematic solution. In a 2002 article by Hsu *et al.* [27], a deterministic tuning algorithm is introduced which makes it possible for an  $n$ -resonator filter to be tuned within  $(2n - 1)$  steps.

The first step in the tuning process is to perform parameter extraction from measurements or simulation. This is achieved by using the theory outlined in Section 5.2.2. As described above, this technique relies on a short circuit termination directly beyond the final resonator. However, in a practical system, the connector between the final resonator and short circuit acts as a length of transmission line with an unknown amount of phase shift, as illustrated in Fig. 5.6.

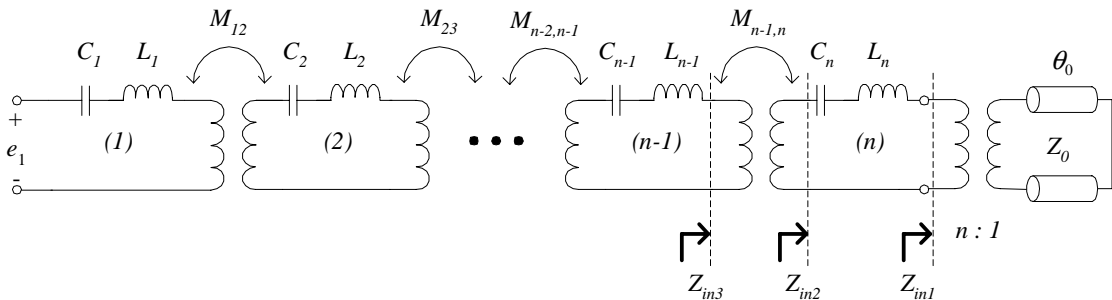


Fig. 5.6. Modified equivalent circuit including an unknown length of transmission line to account for the shift in the short circuit reference plane [27].



A useful extension to the method in Section 5.2.2 is the ability to remove the effect of this piece of transmission line from the calculated filter parameters.

With

$$Z_{in1} = n^2 j Z_0 \tan \theta_0 \quad (5.18)$$

and

$$Z_{in2} = \frac{1}{j\omega C_n} + j\omega L_n + Z_{in1} \quad (5.19)$$

the input impedance of the final resonator can be written as

$$Z_{in3} = -j \frac{M_{n-1,n}^2}{Z_{0n}\lambda + n^2 Z_0 \tan \theta_0} \quad (5.20)$$

In the above equation,  $Z_{0n} = \sqrt{L_n/C_n}$  and  $2\pi f_{0n} = 1/\sqrt{L_n C_n}$  are defined as the characteristic impedance and *actual* resonant frequency of resonator  $n$ , respectively, while  $\lambda$  is defined as

$$\lambda = \frac{f}{f_{0n}} - \frac{f_{0n}}{f} \quad (5.21)$$

By using the recursive equations outlined in Section 5.2.2, it is possible to extract the *measured* natural frequency of the final resonator ( $f_{0n}^{(a)}$ ) from the circuit corresponding to Fig. 5.6. To obtain a relation between  $f_{0n}^{(a)}$  and  $\theta_0$ , set  $Z_{in2} = 0$ .

$$\lambda_a \equiv \frac{f_{0n}^{(a)}}{f_{0n}} - \frac{f_{0n}}{f_{0n}^{(a)}} = -\frac{R_n}{Z_{0n}} \tan \theta_0 \quad (5.22)$$

In eqn. 5.22,  $R_n = n^2 Z_0$  is the known equivalent output coupling resistance and the three unknown variables are  $f_{0n}$ ,  $Z_{0n}$  and  $\theta_0$ . Therefore, in order to solve these unknowns, two more equations are needed. The first equation is obtained by repeating the measurement after connecting a short piece of transmission line of known length  $\theta_1$  between the filter and short circuit, and determining the final resonator frequency  $f_{0n}^{(b)}$ . Another repetition of the measurement, this time with  $\theta_2$  instead of  $\theta_1$ , yields the second equation in terms of  $f_{0n}^{(c)}$ .

$$\lambda_b \equiv \frac{f_{0n}^{(b)}}{f_{0n}} - \frac{f_{0n}}{f_{0n}^{(b)}} = -\frac{R_n}{Z_{0n}} \tan (\theta_0 + \theta_1) \quad (5.23)$$

$$\lambda_c \equiv \frac{f_{0n}^{(c)}}{f_{0n}} - \frac{f_{0n}}{f_{0n}^{(c)}} = -\frac{R_n}{Z_{0n}} \tan (\theta_0 + \theta_2) \quad (5.24)$$

With eqns. 5.22 to 5.24, it is possible to solve all the aforementioned unknowns. As a practical consideration, in order for the approximations in the parameter extraction theory to be valid, the addition of  $\theta_1$  and  $\theta_2$  should not alter the filter response too dramatically. Typically, this requires  $\theta_1$  and  $\theta_2$  to be smaller than  $30^\circ$ . Once  $\theta_0$  is known, the only parameter that has to be changed from the initial parameter extraction results is the resonant frequency of the final resonator. The difference between the perturbed and unperturbed  $n^{\text{th}}$  resonant frequency can be derived as

$$\Delta f = \frac{1}{2} \text{BW} \cdot R_n \cdot \tan \theta_0 \quad (5.25)$$

with BW the filter bandwidth [27].

## Tuning Procedure

The deterministic tuning procedure is initialised by establishing the location of the reference plane, in order to make accurate phase measurements possible. For series resonators, this is achieved by detuning all resonators and adjusting the reference plane until the phase of the reflection coefficient is located at  $0^\circ$ .

Secondly, the input and output coupling values have to be measured and adjusted. This can be done by applying the techniques described in Section 4.5.2, and will depend on the type of resonator and feed structure.

After the adjustment of the input and output couplings, all the resonators are brought into resonance and the unknown connector length  $\theta_0$  is determined with the technique described earlier in the section. Next, the output port of the filter is terminated in a short circuit and the zeros and poles of the structure are recorded as  $\{f_{zi}^{(0)}; f_{pj}^{(0)}\}_{i=1-n; j=1-(n-1)}$ . By using eqns. 5.10 to 5.15, the individual resonant frequencies and coupling values can be synthesised from the poles and zeros as  $\{f_{0i}^{(0)}; m_{j,j+1}^{(0)}\}_{i=1-n; j=1-(n-1)}$ . These extracted filter parameters will differ from the ideal values  $\{\hat{f}_{0i}; \hat{m}_{j,j+1}\}_{i=1-n; j=1-(n-1)}$ .

The tuning procedure can be summarised as follows: By replacing one of the parameters in the current coupling matrix with its ideal value, synthesising poles and zeros from this new coupling matrix, and tuning the corresponding parameter until the measured poles and zeros on the vector network analyser (VNA) correspond to the synthesised poles and zeros, one is effectively tuning the current parameter to its ideal value. For example, replace  $m_{12}^{(0)}$  with its ideal value  $\hat{m}_{12}$  in the list of extracted filter parameters. This yields parameters of  $\{f_{0i}^{(0)}; \hat{m}_{12}, m_{j,j+1}^{(0)}\}_{i=1-n; j=2-(n-1)}$ . From these values, synthesise poles and zeros  $\{f_{zi}^{(1)}; f_{pj}^{(1)}\}_{i=1-n; j=1-(n-1)}$  and indicate them with markers on the VNA. Now, tune the structure which provides coupling  $m_{12}$  until the measured poles and zeros correspond to the markers. When this is the case,  $m_{12}^{(1)}$  will be equal to  $\hat{m}_{12}$ . Necessarily, one has to assume that the change in the value of  $m_{12}$  due to the adjustment of other parameters is so small that it will not have a substantial effect on the final filter response. However, it has not been verified in this thesis.

The procedure of adding one ideal parameter at a time, synthesising poles and zeros, and tuning the corresponding parameter, is repeated for all coupling values and resonant frequencies and can be executed in any order. In a direct-coupled filter, this would lead to the tuning of  $n$  resonant frequencies and  $(n - 1)$  coupling values.

## Applications and Restrictions

What makes this procedure different from the methods discussed previously, is its ability to provide a deterministic tuning method which isolates the effect of one parameter. As each parameter is tuned only once, an  $n^{\text{th}}$  order direct-coupled filter can be tuned in  $(2n - 1)$  steps. Parameter extraction is achieved as in Section 5.2.2, with the added functionality of the removal of the phase shift caused by the connector between the final resonator and the short circuit plane. As in the previous section, this parameter extraction method can be applied to either series or parallel resonators and can be used with filters which require different individual resonant frequencies.

The restrictions which apply to the parameter extraction procedure are identical to those listed in Section 5.2.2. It includes the required detuning of cross couplings, the increased effect of random phase measurement error with the number of resonators, and the inability to use this extraction method when the effect of the feed structure is to alter the phase response of the filter. The only restriction which applies to the tuning procedure itself, is the required ability to tune all coupling values and resonant frequencies in real time, while the filter is connected to the vector network analyser. This procedure promises to be a useful tool in the design process and brings high performance microwave filter design one small step closer to a fully automated tuning process.

### 5.2.4 Parameter Extraction via $S_{11}$ Group Delay

As an alternative to the zero crossing parameter extraction techniques described thus far, Ness [28] presents a method which utilises the group delay of a short-circuited set of resonators. The theory is derived from the standard low pass to bandpass to inverter-coupled resonator process which is often used in filter design. The corresponding prototype circuits are shown in Fig. 5.7.

The group delay of  $S_{11}$  is defined as

$$\Gamma_d(\omega) = -\frac{\partial\phi}{\partial\omega} \quad (5.26)$$

with  $\phi$  the phase of  $S_{11}$  in radians, and  $\omega$  the angular frequency. Through the expansion of the group delay with a low pass to bandpass transformation, Ness proceeds to derive the following equation.

$$\Gamma_d(\omega) = \frac{2(\omega^2 + \omega_0^2)}{\omega^2(\omega_2 - \omega_1)} \frac{\partial}{\partial\omega^1} \left( \tan^{-1} \left[ \frac{X_{in}(\omega^1)}{Z_0} \right] \right) \quad (5.27)$$

In eqn. 5.27,  $\omega_0$  is the filter centre frequency,  $\omega_1$  and  $\omega_2$  is the lower and upper frequency of the pass band respectively,  $\omega^1$  is the angular frequency of the low pass prototype,  $Z_{in} =$

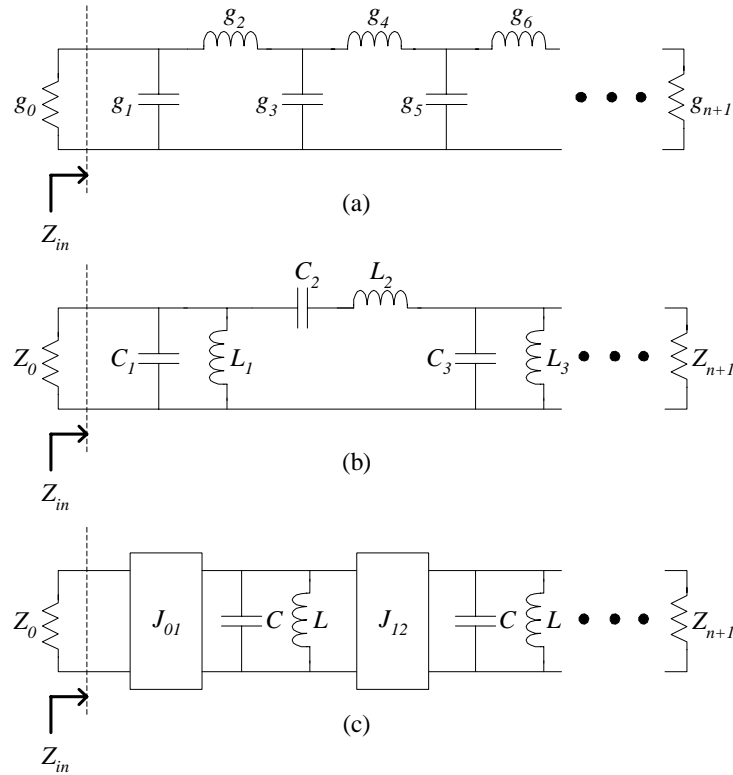


Fig. 5.7. Circuits corresponding to the (a) low pass, (b) bandpass and (c) inverter-coupled resonator prototypes. [28]

$jX_{in}$  is the input impedance of the filter, and  $Z_0$  is the source impedance. Considering the low pass network when only the first capacitor is included in the circuit,

$$X_{in}(\omega^1) = -\frac{1}{\omega^1 g_1} \quad (5.28)$$

and

$$Z_0 = g_0 \quad (5.29)$$

Substitution of eqns. 5.28 and 5.29 into eqn. 5.27, leads to the following expression for the group delay in terms of the low pass filter parameters, as evaluated at  $\omega_0$ . Resonance is defined as the frequency corresponding to the maximum group delay value of the single-resonator circuit.

$$\Gamma_{d1}(\omega_0) = \frac{4g_0 g_1}{\omega_2 - \omega_1} \quad (5.30)$$

In terms of the inverter circuit, the group delay can be written as

$$\Gamma_{d1}(\omega_0) = \frac{4Q_e}{\omega_0} \quad (5.31)$$

with  $Q_e$  defined as the external Q-factor, established by the input coupling value. This relates  $Q_e$  to the group delay at the centre frequency, measured when only one resonator has been brought into resonance.

By repeating this process for the addition of each resonator, it is possible to find expressions for  $\Gamma_{di}$  (the group delay corresponding to the addition of the  $i^{\text{th}}$  resonator) in

terms of the low pass parameters and bandpass coupling coefficients. The results are summarised in [28].

### Applications and Restrictions

This theory enables the calculation of group delay values corresponding to the low pass filter element values which realise a certain desired response. The realisation of this filter response is then achieved by adjusting the group delay values at the centre frequency to correspond to the predetermined values calculated from the low pass parameters, while maintaining a symmetrical response as each resonator is added to the circuit. Conversely, parameter extraction can be applied by measuring the different values of group delay as each resonator is added, and using these values to calculate the coupling coefficients and external Q-factor.

As with the procedures discussed earlier in this section, the current technique is limited by the ideal filter model used in the derivation, as it does not take the effect of a more complex feed structure into account. Due to the fact that the procedure relies on the sequential tuning of resonators, cross couplings have to be detuned. The absence of losses in the filter model does not pose a major problem, as it is proven to be a practical assumption for filters with insertion loss of less than 3 dB, or a ratio of external to unloaded Q-factor of smaller than 0.1. This is the case for many coupled resonator filters, especially those realised in waveguide or coaxial resonator cavities. Additionally, the theory requires frequency-invariant coupling reactances, negligible non-adjacent couplings and the modeling of resonators as  $LC$ -circuits. These are essentially narrow band approximations and become less valid when bandwidths exceed 20%.

## 5.3 Parameter Extraction via Optimisation

Although parameter extraction methods based on the model of a short-circuited final series resonator are easy to implement and, in some cases, promise to be a powerful aid in the tuning procedure, they have a severe restriction in the inability to handle feed structures which alter the phase response of the filter from the ideal series or parallel response. The parameter extraction methods described in this section are not based on the phase measurements of a set of resonators, but rather on direct optimisation methods. In Section 5.3.1 gradient-based optimisation is used to construct the ideal coupling matrix from the transfer polynomials, and also to extract the coupling matrix from the measured complex S-parameters. Another gradient-based parameter extraction technique is summarised in Section 5.3.2, which makes it possible to align severely detuned

filters. Finally, in Section 5.3.3, parameter extraction is performed in Microwave Office with the aid of an equivalent circuit model.

### 5.3.1 Automated Filter Tuning Using Gradient-Based Parameter Extraction

In a 2001 paper by Harscher *et al.* [29] a different approach to the problem of automated filter tuning is presented. Firstly, an alternative method, based on gradient optimisation, is given for the synthesis of the ideal coupling matrix. Then, parameter extraction and a sensitivity analysis make it possible to tune the filter automatically with controlling software and DC motors which turn the tuning screws. As an example, the equations for a fourth order filter with series resonators and cross coupling between resonators 1 and 4 will be given. Consider the equivalent circuit in Fig. 5.8.

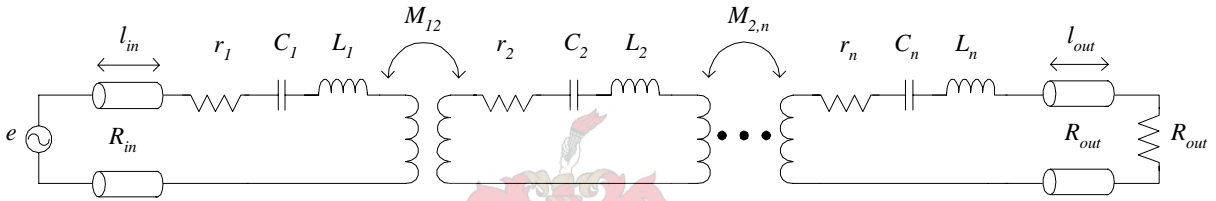


Fig. 5.8. Prototype filter model of  $n$  coupled resonators.

By performing the circuit analysis outlined in Chapter 2, it follows that the low pass loop currents  $\mathbf{I}$  and port voltages  $\mathbf{E}$  can be related by the matrix  $\mathbf{A}$  as follows.

$$\mathbf{I} = -j [\mathbf{A}^{-1}] \cdot \mathbf{E} \quad (5.32)$$

with

$$\mathbf{A} = \begin{bmatrix} \omega + \omega_1 - jr_1 - jR_{in} & M_{12} & 0 & M_{14} \\ M_{12} & \omega + \omega_2 - jr_2 & M_{23} & 0 \\ 0 & M_{23} & \omega + \omega_3 - jr_3 & M_{34} \\ M_{14} & 0 & M_{34} & \omega + \omega_4 - jr_4 - jR_{out} \end{bmatrix} \quad (5.33)$$

In eqn. 5.33,  $\omega$  is the centre frequency of the filter,  $\omega_i$  is the individual resonator frequency offset,  $r_i$  represents the resonator loss, and  $R_{in}$  and  $R_{out}$  are the input and output coupling resistances, respectively.

From general two port analysis, the S-parameters of the two port prototype network are given by

$$\begin{aligned} S_{21} &= 2\sqrt{R_{in}R_{out}}I_4 \\ &= -2j\sqrt{R_{in}R_{out}}\mathbf{A}_{41}^{-1} \end{aligned} \quad (5.34)$$

and

$$\begin{aligned} S_{11} &= 1 - 2R_{in}I_1 \\ &= 1 + 2jR_{in}\mathbf{A}_{11}^{-1} \end{aligned} \quad (5.35)$$

Expansion of eqn. 5.34 makes it possible to write  $S_{21}$  as a ratio of polynomials with complex coefficients.

$$S_{21} = 2\sqrt{R_{in}R_{out}} \frac{a_2\omega^2 + a_1\omega + a_0}{b_4\omega^4 + b_3\omega^3 + b_2\omega^2 + b_1\omega + b_0} \quad (5.36)$$

In terms of coupling values, the complex coefficients are given by eqn. 5.37. For the sake of simplicity, the ideal  $A$ -matrix is used, with  $r_i = \omega_i = 0$ .

$$\begin{aligned} a_2 &= jM_{14} \\ a_1 &= 0 \\ a_0 &= -jM_{14}M_{23}^2 + jM_{12}M_{23}M_{34} \\ b_4 &= 1 \\ b_3 &= -jR_{in} - jR_{out} \\ b_2 &= -M_{12}^2 - M_{23}^2 - M_{34}^2 - M_{14}^2 - R_{in}R_{out} \\ b_1 &= jR_{in}(M_{23}^2 + M_{34}^2) + jR_{out}(M_{12}^2 + M_{23}^2) \\ b_0 &= M_{14}^2M_{23}^2 + M_{12}^2M_{34}^2 + M_{23}^2R_{in}R_{out} - 2M_{12}M_{23}M_{34}M_{14} \end{aligned} \quad (5.37)$$

At this stage, the coupling values and input/output resistances in eqn. 5.37 are still unknown. In order to find these values in terms of a desired transfer function (e.g. a specified level of return loss and prescribed transmission zeros), a low pass prototype transfer function in terms of  $\omega$ ,  $S_{21}(\omega)^{\text{math}}$ , is synthesised.

$$\begin{aligned} S_{21}(\omega)^{\text{math}} &= \frac{P(\omega)}{\epsilon E(\omega)} \\ &= \frac{a_2^{\text{math}}\omega^2 + a_1^{\text{math}}\omega + a_0^{\text{math}}}{\omega^4 + b_3^{\text{math}}\omega^3 + b_2^{\text{math}}\omega^2 + b_1^{\text{math}}\omega + b_0^{\text{math}}} \end{aligned} \quad (5.38)$$

This is a well-known procedure, first used by Darlington in 1939 for a symmetrical filter response [13], and later, amongst others, by Cameron for an asymmetrical filter response [8]. The unknown values of the coupling matrix are found by optimising values for  $M_{ij}$ ,  $R_{in}$  and  $R_{out}$  in order to minimise the cost function  $F_1$  created by the difference between the unknown complex coefficients in eqn. 5.37 and the known, synthesised coefficients of  $S_{21}(\omega)^{\text{math}}$ .

$$\begin{aligned} F_1 &= (a_2 - a_2^{\text{math}})^2 + (a_1 - a_1^{\text{math}})^2 + (a_0 - a_0^{\text{math}})^2 \\ &\quad + (b_3 - b_3^{\text{math}})^2 + (b_2 - b_2^{\text{math}})^2 + (b_1 - b_1^{\text{math}})^2 + (b_0 - b_0^{\text{math}})^2 \end{aligned} \quad (5.39)$$

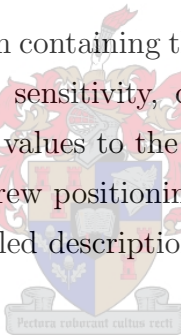
Convergence of the gradient optimisation leads to the ideal values of  $M_{ij}$ ,  $R_{in}$  and  $R_{out}$ .

Next, parameter extraction has to be performed on the measured response of the roughly pre-tuned filter. This is done by performing a bandpass to low pass transformation on the measured data ( $S_{ij}^{\text{meas}}$ ) and minimising the cost function  $F_2$  in eqn. 5.40, obtained from the difference between  $S_{ij}^{\text{meas}}$  and the S-parameters of the prototype model in Fig. 5.8 ( $S_{ij}^{\text{netw}}$ ). This is done by optimising the prototype model parameters. Convergence of the optimisation procedure leaves one with model parameters equal to the measured parameters.

$$F_2 = \sum_f \sum_{i=1}^2 \sum_{j=1}^2 [\text{Re}\{S_{ij}^{\text{netw}}\} - \text{Re}\{S_{ij}^{\text{meas}}\}]^2 + [\text{Im}\{S_{ij}^{\text{netw}}\} - \text{Im}\{S_{ij}^{\text{meas}}\}]^2 \quad (5.40)$$

In order to make filter tuning without human operators possible, the system controlling the tuning screws needs information about the effect of each individual tuning screw on all the other filter parameters. This is obtained by performing a sensitivity analysis. By turning one screw at a time a fixed amount and repeating the parameter extraction, the differences in all the filter parameters can be noted, and parameter sensitivities can be calculated.

Subsequently, another cost function containing the maladjustment of each filter parameter and the corresponding parameter sensitivity, can be minimised to yield the optimum screw positions. By sending these values to the DC motor controlling the tuning screws, the appropriate adjustments in screw positioning can be made, resulting in a well-tuned microwave filter. For a more detailed description of the tuning procedure, refer to [29].



## Applications and Restrictions

Although parameter extraction with the current procedure has not been implemented in this thesis, it seems very promising. Together with the ability to handle arbitrary filter topologies and other means of tuning, this method does not require the detuning of cross couplings. This is a great advantage, as ultimately, the detuning of a resonator does have a measurable effect on the operation of the rest of the filter. Another benefit is the ability to use prototype filters of varying complexity in the parameter extraction optimisation procedure. This allows one, for example, to incorporate an accurate model of the tapped feed structure and make parameter extraction of a more complex filter possible. Individual resonant frequencies, losses in the resonator and the effect of the unknown pieces of transmission line at the ports of the filter can also be accounted for in the model. The optimisation procedure is accelerated by the use of analytically calculated gradients of cost functions, and the absence of any matrix inversions or rotations. Accurate results are obtained through the use of complex S-parameters.

However, in order to use the presented prototype model in the parameter extraction pro-



cedure, the initial response of the filter has to be sufficiently close the the ideal filter response. If this is not the case, a local minimum might be encountered in the gradient optimisation procedure, leading to a convergence failure and the inability to extract meaningful filter parameters from measurement [30].

The results presented in [29] bode well for the future of automatic filter tuning. Sensitivity analysis, together with controlling software, make the motorised tuning of units on the production floor a possibility. It has to be stated, though, that automated tuning relies on the approximation of a linear relationship between the tuning screw positions and the filter response. In practice, this is only the case for small tuning ranges, which makes the current procedure only truly applicable in the case of fine tuning.

### 5.3.2 Sequential Tuning Using Adaptive Models and Parameter Extraction

In order to address the challenge of efficiently tuning strongly detuned microwave filters, Pepe *et al.* [30] created a parameter extraction and tuning procedure based on the equivalent circuit of  $n$  multiple-coupled parallel resonators. The resonators are represented by dispersive and lossy open-ended transmission line sections, while the mutual couplings are realised with J-inverters, as illustrated in Fig. 5.9. For the relation between magnetic coupling, K-inverters and J-inverters, see Appendix A.

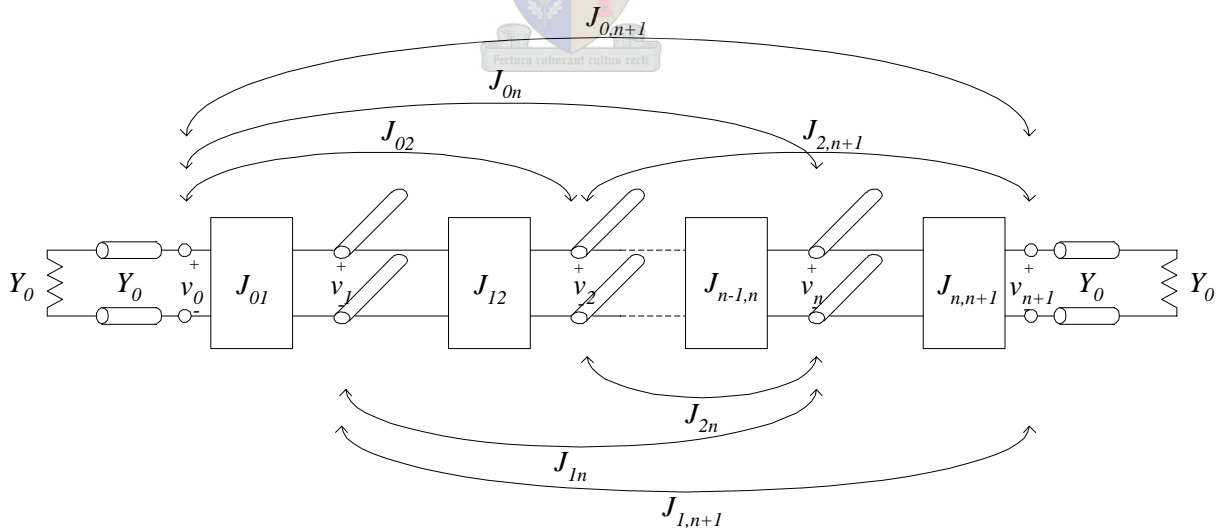


Fig. 5.9. Equivalent circuit of  $n$  coupled parallel resonators.

The vector of nodal voltages  $\mathbf{V} = [v_0, v_1, \dots, v_{n+1}]^T$  and vector of excitation currents  $\mathbf{I} = [i_0, i_1, \dots, i_{n+1}]^T$  are related by the inverse of the nodal admittance matrix  $\mathbf{Y}$ , corresponding to the coupling matrix of the filter.

$$\mathbf{V} = \mathbf{Y}^{-1} \cdot \mathbf{I} \tag{5.41}$$

with

$$\mathbf{Y} = \begin{bmatrix} Y_0 & jJ_{01} & jJ_{02} & \cdots & jJ_{0,n+1} \\ jJ_{01} & \delta_1 & jJ_{12} & \cdots & jJ_{1,n+1} \\ jJ_{02} & jJ_{12} & \ddots & & \vdots \\ \vdots & \vdots & & \delta_n & jJ_{n,n+1} \\ jJ_{0,n+1} & jJ_{1,n+1} & \cdots & jJ_{n,n+1} & Y_0 \end{bmatrix} \quad (5.42)$$

The first and last elements on the main diagonal are equal to the termination admittances  $Y_0$ , while the off-diagonal components are related to the real-valued inverter constants  $J_{ij}$ . The rest of the elements on the main diagonal represent the input admittances  $\delta_i$  of a lossy and dispersive open-ended transmission line of length  $l_i$ , possessing an attenuation factor  $\alpha_i$  and propagation constant  $\beta$ .

$$\begin{aligned} \delta_i(f) &= Y_1 \tanh [(\alpha_i(f) + j\beta(f)) \cdot l_i] \\ &\approx Y_1 [\alpha_i(f)l_i + j \tan(\beta(f)l_i)] \end{aligned} \quad (5.43)$$

The above approximation is valid in the case of low dissipative losses ( $\alpha_i l_i \ll 1$ ).

Next, it is necessary to find a relation between  $S_{11}$  of the equivalent circuit and the admittance matrix which contains the filter coupling values. In Fig. 5.10, the description of the equivalent circuit as a simple two port network consisting of a current source  $I_g$  with internal admittance  $Y_0$ , a network with input admittance  $Y_{in}$  and a load termination of admittance  $Y_0$ , yields an equation for  $S_{11}$ .

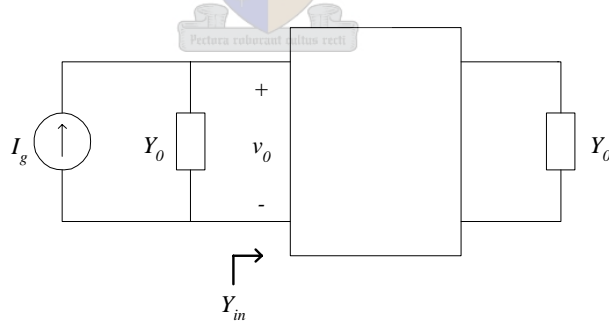


Fig. 5.10. Equivalent circuit as a simplified two port network.

$$S_{11} = v_0 \sqrt{Y_0} - 1 \quad (5.44)$$

It is therefore possible to establish a link between  $\mathbf{Y}$  and  $S_{11}$ , as the nodal voltage  $v_0$  in eqn. 5.44 can be written in terms of the admittance matrix by using eqn. 5.41. With current excitation at port 1,

$$v_0 = \mathbf{Y}_{11}^{-1} i_0 \quad (5.45)$$

where  $\mathbf{Y}_{ij}^{-1}$  refers to the  $(i, j)^{\text{th}}$  component of the inverse of  $\mathbf{Y}$ . Additionally, in order to make provision for the finite length of the connector between the filter and measurement

setup, a phase term is added to eqn. 5.44, and the reflection coefficient of the filter model is redefined as  $S_{11}^{\text{Mod}}$ .

$$S_{11}^{\text{Mod}} = S_{11} e^{-2j\beta_a l_L} \quad (5.46)$$

In the above equation,  $\beta_a$  is the propagation constant of the adapters, and  $l_L$  is the effective adapter length. The relation between  $l_L$  and the measurable adapter length is given in [30].

The current tuning algorithm is based on a sequential procedure which is initialised by detuning all resonators. In the case of coaxial cavity resonators, this is accomplished by turning the tuning screws into the cavity until it touches the resonator post and effectively short circuits the post. The coupling matrix corresponding to this initial state is described by  $\mathbf{Y}^{(0)}$ , while the ideal coupling matrix is defined as  $\mathbf{Y}^{(\text{ID})}$ . Subsequently, the resonators are brought into resonance one after the other, with the addition of each resonator corresponding to a subfilter. A filter of degree  $n$  would therefore have  $n$  subfilters, with subfilter  $i$  consisting of  $i$  un-shortened and  $(n - i)$  shorted resonators. After each subfilter addition, the initial parameters are extracted by minimising the error function  $\epsilon_{(i)}$ .

$$\epsilon_{(i)} = \sum_{j=1}^m |S_{11}^{\text{Meas}}(f_j) - S_{11}^{\text{Mod}}(f_j)_{(i)}|^2 \quad (5.47)$$

In eqn. 5.47,  $m$  is the number of frequency points in the measurement,  $S_{11}^{\text{Meas}}(f)$  is obtained from the measured subfilter, and  $S_{11}^{\text{Mod}}(f)_{(i)}$  is calculated from the coupling matrix

$$\mathbf{Y}^{(i)a} = \begin{bmatrix} \mathbf{A}^{(i)a} & \mathbf{B}^{(i)} \\ \mathbf{C}^{(i)} & \mathbf{D}^{(i)} \end{bmatrix} \quad (5.48)$$

by using eqn. 5.46. Submatrix  $\mathbf{A}^{(i)a}$  contains the parameters of the current subfilter, while  $\mathbf{B}^{(i)}$ ,  $\mathbf{C}^{(i)}$  and  $\mathbf{D}^{(i)}$  represent the detuned part of the filter and are described by the corresponding elements in the detuned coupling matrix  $\mathbf{Y}^{(0)}$ . For example, the following coupling matrix belongs to a third order filter, with resonator 1 brought into resonance, corresponding to subfilter 1. The underlined elements are the unknown values of submatrix  $\mathbf{A}^{(i)a}$  which have to be determined via optimisation, while the other elements belong to  $\mathbf{Y}^{(0)}$ .

$$\begin{bmatrix} \mathbf{A}^{(i)a} & \mathbf{B}^{(i)} \\ \mathbf{C}^{(i)} & \mathbf{D}^{(i)} \end{bmatrix} = \begin{bmatrix} \underline{Y_0} & \underline{jJ_{01}} & Y_{02}^{(0)} & Y_{03}^{(0)} & Y_{04}^{(0)} \\ \underline{jJ_{01}} & \underline{\delta_1} & Y_{12}^{(0)} & \cdot & \cdot \\ Y_{02}^{(0)} & Y_{12}^{(0)} & Y_{22}^{(0)} & \cdot & \cdot \\ Y_{03}^{(0)} & \cdot & \cdot & \cdot & \cdot \\ Y_{04}^{(0)} & \cdot & \cdot & \cdot & Y_{44}^{(0)} \end{bmatrix} \quad (5.49)$$

The goal of the tuning step  $i$  is the convergence of  $\mathbf{A}^{(i)a}$  with the corresponding submatrix  $\mathbf{A}^{(i)}$  of the ideal coupling matrix  $\mathbf{Y}^{(\text{ID})}$ .

However, in practice, there will be some deviation between the current subfilter and the ideal coupling values. In order to prevent these residual errors in the optimisation

process from propagating, not all the previously tuned elements are tuned again after the addition of a new subfilter. If one chooses to adjust  $m$  resonators in tuning step  $i$ , only resonators  $(i - m + 1)$  to  $i$ , and any coupling value included by these resonators, will be tuned in order to agree with the corresponding elements in the ideal coupling matrix. The rest of the elements of  $\mathbf{A}^{(i)}$  are changed to be equal to the corresponding elements in matrix  $\mathbf{A}^{(i-1)a}$ . For example, consider an eighth order filter, with subfilter 6 being brought into resonance ( $i = 6$ ). If one chooses to re-adjust four resonators in this tuning step ( $m = 4$ ), only resonators 3 to 6 and couplings  $\{J_{34}, J_{35}, J_{36}, J_{45}, J_{46}, J_{56}\}$  will be readjusted to correspond to the ideal coupling matrix.

In addition to a systematic tuning approach, this method also provides a means of conducting fault diagnosis. The failure of submatrix  $\mathbf{A}^{(i)a}$  to converge with  $\mathbf{A}^{(i)}$  indicates that the parameter out of tolerance exists in the current subfilter.

### Applications and Restrictions

This method of parameter extraction and tuning promises to be quite a powerful aid in the process of microwave filter alignment, as it handles filters of both a low and high degree, singly and doubly terminated filters, and single and dual mode resonators. Cross couplings and resonant frequency offsets are also extracted without any complications. More importantly, though, is the ability of this procedure to tune strongly detuned filters systematically, and to isolate a component which is out of tolerance. In the case of simple, lower-order filters, there will be sufficient filter alignment after completing this procedure, while for higher-order filters, it will serve as an excellent basis for further fine-tuning procedures.

In order to use this technique, it has to be possible to detune the filter resonators. The state of the filter after completing the tuning procedure will depend strongly on the degree of convergence to the ideal coupling matrix that was achieved with the addition of each subfilter.

### 5.3.3 Parameter Extraction in Microwave Office

The principles which apply to parameter extraction in Microwave Office are the same as those discussed in the two previous sections — One starts with an equivalent model and a measurement, and optimises the model in order to match the model response to the measured response. The more accurately the model represents the actual filter, the more successful parameter extraction will be.

If one refers to Fig. 4.34, it is clear that the effect of the tapped feed line structure is to

alter the phase response of the filter quite dramatically. As stated in Section 5.2.1, this is because the extended centre conductor of the 50  $\Omega$  connector possesses considerable series inductance ( $L_f$ ), and the proximity of the grounded cavity walls creates parallel capacitance between the centre conductor and ground ( $C_f$ ). The model also includes an ideal transformer which represents the tap point and determines the amount of input coupling that is achieved. This leads to the circuit in Fig. 5.11.

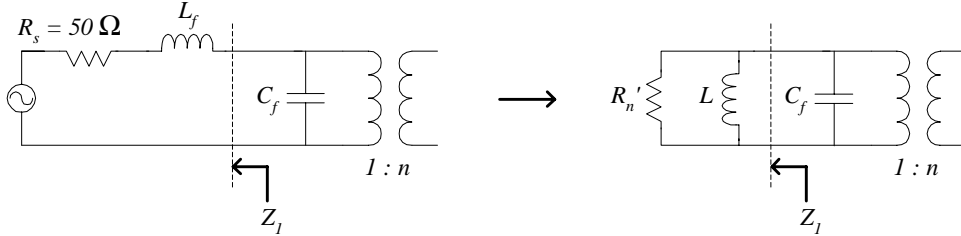


Fig. 5.11. Model of tapped feed structure.

In order to create an acceptable model of the feed, the values of  $L_f$ ,  $C_f$  and the transformer ratio  $n$  have to be determined. To do so, one enforces the condition for resonance of  $L$  and  $C_f$  at  $\omega_0$ , the centre frequency of the filter. If this is the case, the filter would see a purely resistive input impedance. Although this is a convenient and fairly accurate way to model the feed, the actual dynamics are probably slightly different. It is more likely that the resonant frequency of  $L$  and  $C_f$  does not correspond to  $\omega_0$ , and that there exists a certain parallel admittance at  $\omega_0$  which transforms across to the main cavity. The effect of this would be a shift in the resonant frequency of resonator 1 after the insertion of the feed structure. Simulations in CST Microwave Studio show this to be the case.

Returning to the problem of solving the unknown feed model parameters, consider the impedance  $Z_1$ . As an initial estimate, one may assume that wire possesses inductance of 1 nH/mm. This makes it possible to have an estimated value for  $L_f$  by measuring the length of extended centre conductor in the cavity. At the centre frequency of the filter,

$$Z_1 = R_s + j\omega_0 L_f \quad (5.50)$$

which leads to

$$\begin{aligned} Y_1 &= 1/Z_1 \\ &= \frac{R_s - j\omega_0 L_f}{R_s^2 + (\omega_0 L_f)^2} \\ &= \frac{1}{R_n'} - j\frac{1}{\omega_0 L} \end{aligned} \quad (5.51)$$

As  $R_s$  and  $L_f$  are known, it is possible to solve  $R_n'$  and  $L$  from eqn. 5.51. The aforementioned condition for resonance at  $\omega_0$  yields an expression for  $C_f$ .

$$C_f = \frac{1}{\omega_0^2 L} \quad (5.52)$$

Finally, the transformer ratio  $n$  is calculated by relating  $R_n'$  to the required input coupling value  $R_n$ . In eqn. 5.53,  $B$  is the filter bandwidth,  $R$  corresponds to the low pass input coupling, and  $Z_0$  is the filter characteristic impedance. For details of the impedance and bandwidth scaling procedure, refer to Appendix B.

$$R_n = \frac{1}{B R Z_0} \quad (5.53)$$

$$= n^2 R_n' \quad (5.54)$$

To complete the filter, parallel resonators are constructed from ideal inductors and capacitors. By using the theory in Section 4.6 which relates the individual resonator resonant frequency to its corresponding diagonal entry in the coupling matrix, it is possible to find an expression for the resonator inductors and capacitors in terms of the coupling matrix. With  $\omega_i$  the individual resonant frequency of the  $i^{\text{th}}$  resonator,  $\omega_0$  the filter centre frequency and  $Z_0$  the filter characteristic impedance, eqn. 4.70 can be used to determine the values of the resonator elements.

$$L_i = C_i = \frac{1}{\omega_i} \frac{-M_{ii} + \sqrt{\left(\frac{M_{ii}}{2Z_0}\right)^2 + 1}}{\omega_0} \quad (5.55)$$

The inter-resonator couplings are established with ideal J-inverters, with values specified by the off-diagonal entries in the coupling matrix. To create J-inverters, frequency independent inductors are used in a  $\pi$ -formation, with values of  $1/(\omega_0 M_{ij})$ . Please refer to Appendix B for a comparison between K- and J-inverters and the values of each in relation to its constituting elements.

Fig. 5.12 illustrates the final coupled resonator model. As no transmission line is included as part of the feed, the measured S-parameters have to be de-embedded to remove the connectors' residual phase shift. In CST, this can be done automatically by shifting the reference plane. In order to de-embed measurements, one has to add transmission lines with negative phase shift corresponding to the length of the teflon inside each connector, to the data set which contains the measurements. This can be done in Microwave Office.

What makes Microwave Office an attractive option for parameter extraction, is the fact that there are many pre-written optimisation routines to choose from. However, it should be stated that most extraction efforts in this thesis did not end in complete convergence of the model and measurements. This is probably because the solution space is quite complex, with many local minima which the optimiser may find. The optimisation process was completed as follows:

- In order to decrease the probability of the optimiser for finding a local minimum, one should start with only a few variables, ideally no more than four.
- By first optimising the main diagonal entries in the coupling matrix, one finds an estimate of the individual resonant frequencies, which leads to the optimised response being centred around the measured response.
- The second optimisation run can then be completed with the off-diagonal couplings and cross couplings to match the shape of the optimised response to the measurement.
- Finally, the value of the feed inductance is optimised to yield the best match to the measurement.

It was found that, for the current application, the best optimisers to use in Microwave Office are the Simplex, Pointer Robust and Pointer Gradient optimisers.

### Applications and Restrictions

All parameter extraction procedures in this thesis were completed in Microwave Office, as, at the time, it was the only known procedure which could accommodate the complex feed structure. Although only a few optimisation runs resulted in a complete convergence of the model response and measurements, the results were accurate enough to indicate which parameters were in need of adjustment. This made it possible to correct the shift in resonant frequencies caused by the initial assembly of the individual cavities and coupling structures in CST Microwave Studio. Parameter extraction in Microwave Office was also applied with great success to measurements of the constructed filters.

Considering its limitations, this method does not contain sensitivity analyses. Additionally, there exists no real time connection between the parameter extraction software and the measurement setup. It is therefore impossible to use the current parameter extraction in Microwave Office as a fine tuning procedure. Essentially, its use lies in the ability to isolate strongly detuned parameters, and to conduct fault diagnosis on a post-processing basis. If filter fine tuning should be required, a routine such as the one outlined in Section 5.3.1 is recommended.

## 5.4 Conclusion

After the evaluation of some of the parameter extraction and tuning procedures which have been employed over the last two decades, it was found that the extraction methods

based on a one port phase measurement of the filter cannot be used when the filter includes a feed structure, like a tapped line, which alters the phase response from the ideal series or parallel phase response. A different solution is to perform optimisation procedures which adjust the parameters of a model to match a measured response. The success of this approach lies in the accuracy of the model and the complexity of the error space. Tuning procedures have been outlined which makes it possible to align severely detuned filters, as well as perform fine-tuning steps with the aid of sensitivity analysis. Fine tuning with the aid of controlling software and tuning screws turned by DC motors, make the alignment of filter units on the production floor a real possibility.





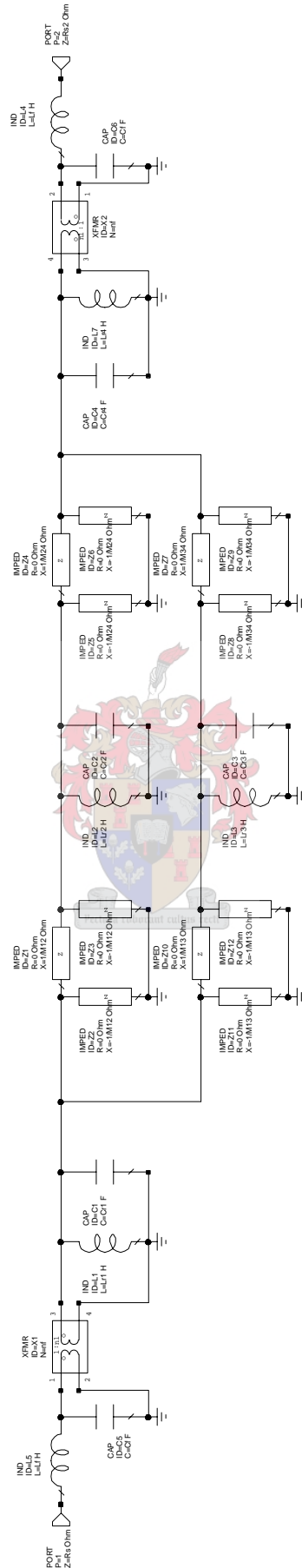


Fig. 5.12. Microwave Office parameter extraction model.

# Chapter 6

## Prototype Filters

### 6.1 Introduction

In order to complete the cycle of analysis, synthesis, design and measurement, two asymmetrical fourth order filters were designed and built by using the theory presented in Chapter 4. The first filter uses an evanescent mode coupling element to establish negative coupling, while the second filter achieves this by means of a capacitive probe.

Identical specifications were used in the design of the filters, in order to make it possible to compare the two types of filter in terms of their ease of implementation and performance. In the current design, the main objective is the realisation of an asymmetrical transfer function. Asymmetrical filters are commonly used in duplexers which require high rejection levels between transmit and receive bands. A summary of the filter specifications is given in Table 6.1.

Parameter	Low pass value	Bandpass value
Centre frequency	0 rad/s	3 GHz
Bandwidth	1 rad/s	3 % = 90 MHz
Transmission zero frequency	2 rad/s	3.092 GHz
Return loss in pass band	$\geq 20$ dB	$\geq 20$ dB
Filter order	4	4

TABLE 6.1  
Filter specifications.

The design and assembly of the filter structure was completed in CST Microwave Studio.

### 6.2 Coupling Matrix Synthesis

The design of a microwave filter begins with the synthesis of the coupling matrix from a set of low pass specifications. With three infinite transmission zeros, one finite transmission

zero at 2 rad/s, and a return loss level of 20 dB inside the pass band, the coupling matrix  $\mathbf{M}_1$  is synthesised by applying the theory described in Chapter 2 and 3.

$$\mathbf{M}_1 = \begin{bmatrix} -0.045038 & 0.507415 & -0.754566 & 0 \\ 0.507415 & 0.865923 & 0 & 0.507415 \\ -0.754566 & 0 & -0.507897 & 0.754566 \\ 0 & 0.507415 & 0.754566 & -0.045038 \end{bmatrix} \quad (6.1)$$

In addition to the coupling matrix, the synthesis procedure yields the value for the input and output coupling resistances,  $R_{in} = R_{out} = R = 1.069 \Omega$ . After performing the necessary bandwidth scaling, the matrix  $\mathbf{M}$  contains the coupling values and resonant frequency offsets which have to be implemented in the filter. With bandwidth  $B$  of 3%,

$$\begin{aligned} \mathbf{M} &= B \cdot \mathbf{M}_1 \\ &= \begin{bmatrix} -0.001351 & 0.015222 & -0.022637 & 0 \\ 0.015222 & 0.025978 & 0 & 0.015222 \\ -0.022637 & 0 & -0.015237 & 0.022637 \\ 0 & 0.015222 & 0.022637 & -0.001351 \end{bmatrix} \end{aligned} \quad (6.2)$$

The off-diagonal entries of  $\mathbf{M}$  in eqn. 6.2 represent the coupling values which have to be implemented by the filter structure.  $M_{13}$ , the negative coupling between resonators 1 and 3, is implemented with capacitive coupling, while  $M_{12}$ ,  $M_{24}$  and  $M_{34}$  are positive and implemented with magnetic coupling. Fig. 6.1 illustrates the basic resonator cavity dimensions used throughout the design.

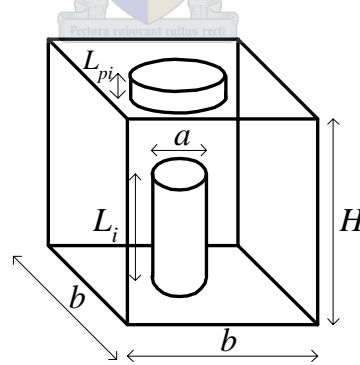


Fig. 6.1. Coaxial resonator cavity dimensions.

With a resonator centre conductor diameter  $a$  of 6 mm and filter characteristic impedance of  $77 \Omega$ , eqn. 4.1 yields a cavity side length  $b$  of 20.22 mm. A cavity depth  $H$  of 30 mm is selected for the filters, which yields an unloaded Q-factor of 4325. With  $H$  constant, the length of the resonator post ( $L_i$ ) can be optimised for a resonant frequency of 3 GHz. In doing so,  $L_i = 21.08$  mm. The initial protrusion level ( $L_{pi}$ ) of the 8.8 mm diameter tuning post is set to 2 mm.

### 6.3 The External Q-factor

The value of the external Q-factor of the filter is determined by the position of the tapped feed line. By referring to eqn. 4.31, the ideal external Q-factor is

$$Q_e = \frac{1}{Bn^2} = 31.18 \quad (6.3)$$

Application of eqn. 4.66 makes it possible to extract the external Q-factor from a one-port  $S_{11}$  simulation. Subsequent comparison of the extracted value with eqn. 6.3 makes it possible to adjust the feed position  $h_f$ . As discussed in Section 4.5.1, a decrease in  $h_f$  will increase  $Q_e$ , while an increase in  $h_f$  will have the opposite effect. This part of the design is extremely important, as an incorrect external Q-factor will ultimately limit the value of  $S_{11}$  in the pass band. Fig. 6.2 demonstrates the tapped feed line and tap position utilised in this design. The lengths of the resonator post and tuning post are given in Section 6.2. For  $h_f = 3.46$  mm,  $Q_e = 31.15$ , which is sufficiently close to the ideal value.

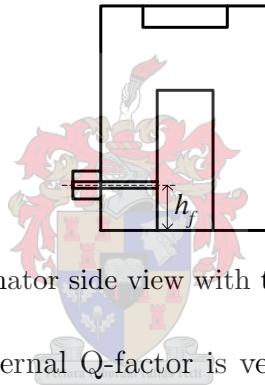


Fig. 6.2. Resonator side view with tapped feed position.

It should be noted that the external Q-factor is very sensitive with respect to the feed position. By decreasing  $h_f$  from 3.4 to 3.2 mm,  $Q_e$  increases from 31.71 to 34.42. The feed structure therefore requires high manufacturing precision.

## 6.4 Prototype Filter 1

### 6.4.1 Filter dimensions

The first filter prototype utilises an evanescent mode coupling element to establish negative coupling. The underlying theory and design considerations are described in Section 4.4.2. Fig. 6.3 shows a side and top view of the completed filter with its roof removed. On the photograph, the resonator cavities are numbered from 1 to 4, with resonator 1 bottom left, 2 top left, 3 bottom right and 4 top right. Resonator 1 corresponds to the input port, while resonator 4 corresponds to the output port.

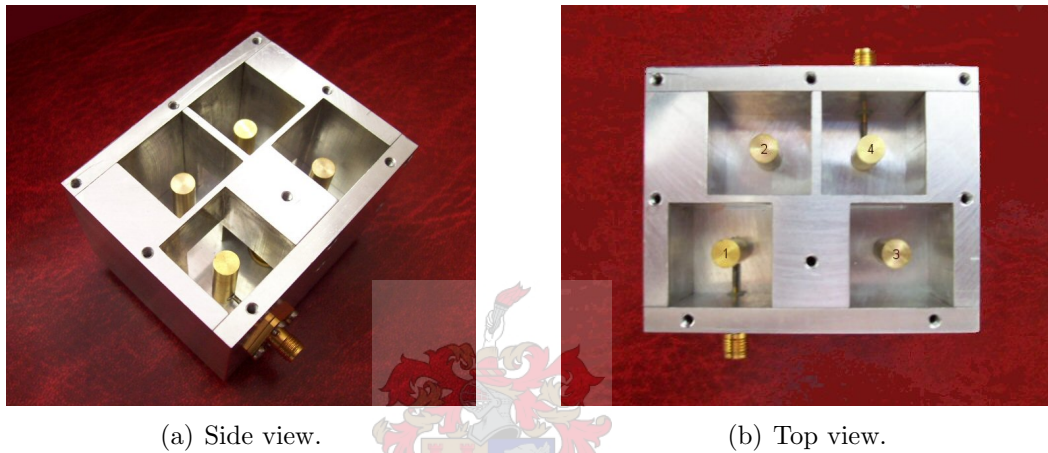


Fig. 6.3. Prototype filter one.

Although the non-zero diagonal entries in  $\mathbf{M}$  require all resonators to be at a certain frequency offset from 3 GHz, the initial resonator cavities used to establish the coupling values are identical and resonate at 3 GHz. This follows from the theory used to determine the coupling value between two cavities (described in Section 4.3), which requires cavities with identical resonant frequencies.

While iris coupling is always the simplest form of coupling, the biggest magnitude of negative E-field coupling that can be obtained via iris coupling with the current resonator structure, is about  $2.5 \times 10^{-3}$ , which is ten times too small for the current application. It is therefore necessary to resort to a different form of negative coupling, the evanescent mode waveguide filter. The necessary coupling values were established by using the theory in Sections 4.3 and 4.4.2. Fig. 6.4 shows resonators 1 and 3 and the first order evanescent mode filter coupling element which establishes  $M_{13}$ . These elements are indicated by the solid blue lines in the foreground. The dimensions corresponding to Fig. 6.4 are given in Table 6.2.

Iris coupling at the base of each resonator is employed to realise the positive H-field coupling values. In order to indicate the dimensions of apertures 1-2 and 3-4 clearly, a

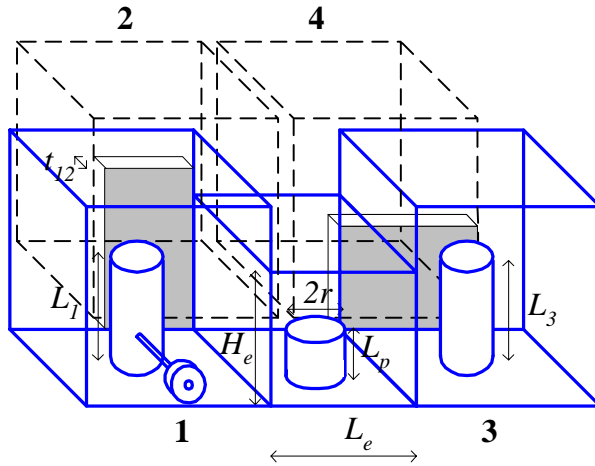


Fig. 6.4. Filter 1: Cavities 1 and 3.

Parameter	Value [mm]
$L_1$	21.05
$L_3$	20.70
$L_e$	15.00
$L_p$	10.11
$H_e$	10.58
$r$	4.40
$t_{12}$	1.50

TABLE 6.2

side view of Fig. 6.4, with cavities 1 and 3 in the foreground, is presented in Fig. 6.5. For the sake of simplicity, resonator posts are omitted from the figure. Note that the filter structure is not symmetrical, with different cavity offsets  $d_{12}$  and  $d_{34}$ . The reason for this asymmetry lies in the required evanescent section length of 15 mm, which differs from  $t_{24}$ , the 2 mm wall thickness between cavities 2 and 4. A purely symmetrical structure with  $d_{12} = d_{34}$  does not yield magnetic coupling large enough to realise  $M_{34}$ . As discussed in Section 4.3, beyond a certain point magnetic coupling fails to increase with aperture height, due to the effect of increasing E-fields. The only solution is therefore to increase the width of aperture 3-4, at the cost of the width of aperture 1-2. Table 6.3 contains the parameter values corresponding to Fig. 6.5.

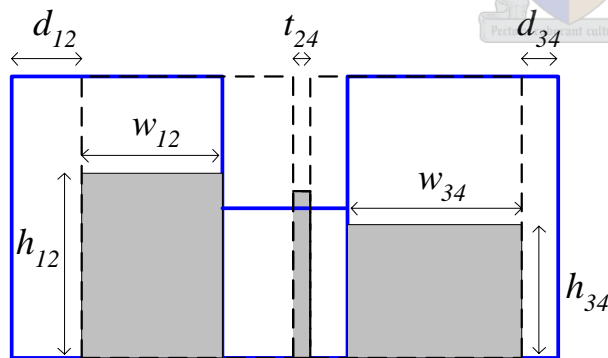


Fig. 6.5. Filter 1: Couplings 1-2 and 3-4.

Parameter	Value [mm]
$d_{12}$	7.60
$d_{34}$	5.40
$t_{24}$	2.00
$w_{12}$	12.64
$h_{12}$	13.91
$w_{34}$	14.84
$h_{34}$	8.47

TABLE 6.3

The only remaining filter cavity dimensions are those related to cavities 2 and 4. In order to illustrate this part of the filter, Fig. 6.4 is essentially ‘turned around’ and viewed from the opposite side. Accordingly, cavities 2 and 4 are in the foreground, as illustrated in Fig. 6.6. Table 6.4 contains the corresponding dimensions.

In order to make the adjustment of the cavity resonant frequencies possible, it is necessary to insert tuning posts in the roof of the filter structure, as illustrated in Fig. 6.7. The post radii and initial protrusion levels are listed in Table 6.5.

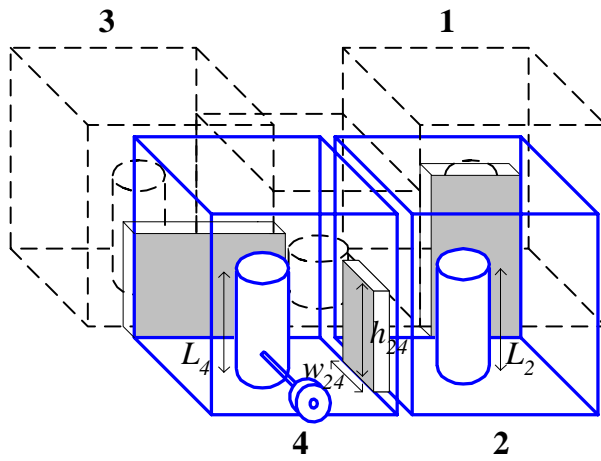


Fig. 6.6. Filter 1: Cavities 2 and 4.

Parameter	Value [mm]
$L_2$	20.30
$L_4$	21.05
$w_{24}$	9.51
$h_{24}$	12.70

TABLE 6.4

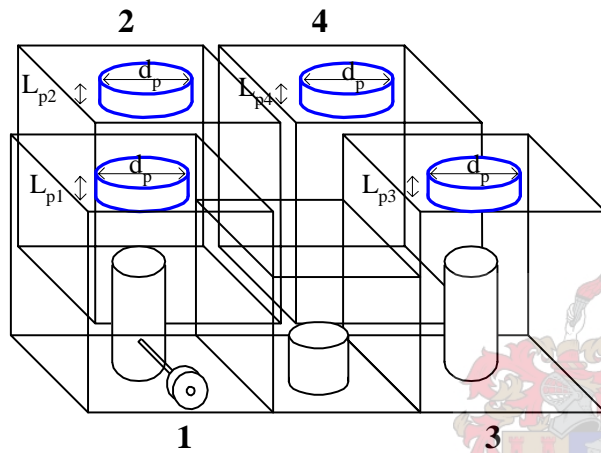


Fig. 6.7. Filter 1: Tuning posts.

Parameter	Value [mm]
$L_{pi}$	2.0
$d_p$	8.8

TABLE 6.5

## 6.4.2 Measurements

Evaluation of the filter performance was completed on an HP8510C vector network analyser (VNA). One notable aspect of this implementation, is the sensitivity of the transmission zero with respect to the evanescent mode capacitive post position. It was found that a change of only 0.01 mm in tuning post position shifts the location of the transmission zero by 31.55 MHz. Fig 6.8 illustrates three filter responses, each with a differently tuned transmission zero frequency. Black horizontal and vertical lines indicate the ideal return loss level and bandwidth, while the rejection specification is indicated in red. From the transmission zero frequency, the rejection can be specified as greater than 40 dB for all frequencies higher than 3.086 GHz.

It was found that, in order for the response to show a clear transmission zero, the return loss level in the pass band is compromised. Shifting the transmission zero up in frequency improves the return loss level from 14.3 dB in Fig. 6.8(a) to 18 dB in Fig. 6.8(e), while the 40 dB rejection specification at 3.086 GHz is compromised slightly. Insertion loss levels also show an improvement when the transmission zero is shifted up in frequency.

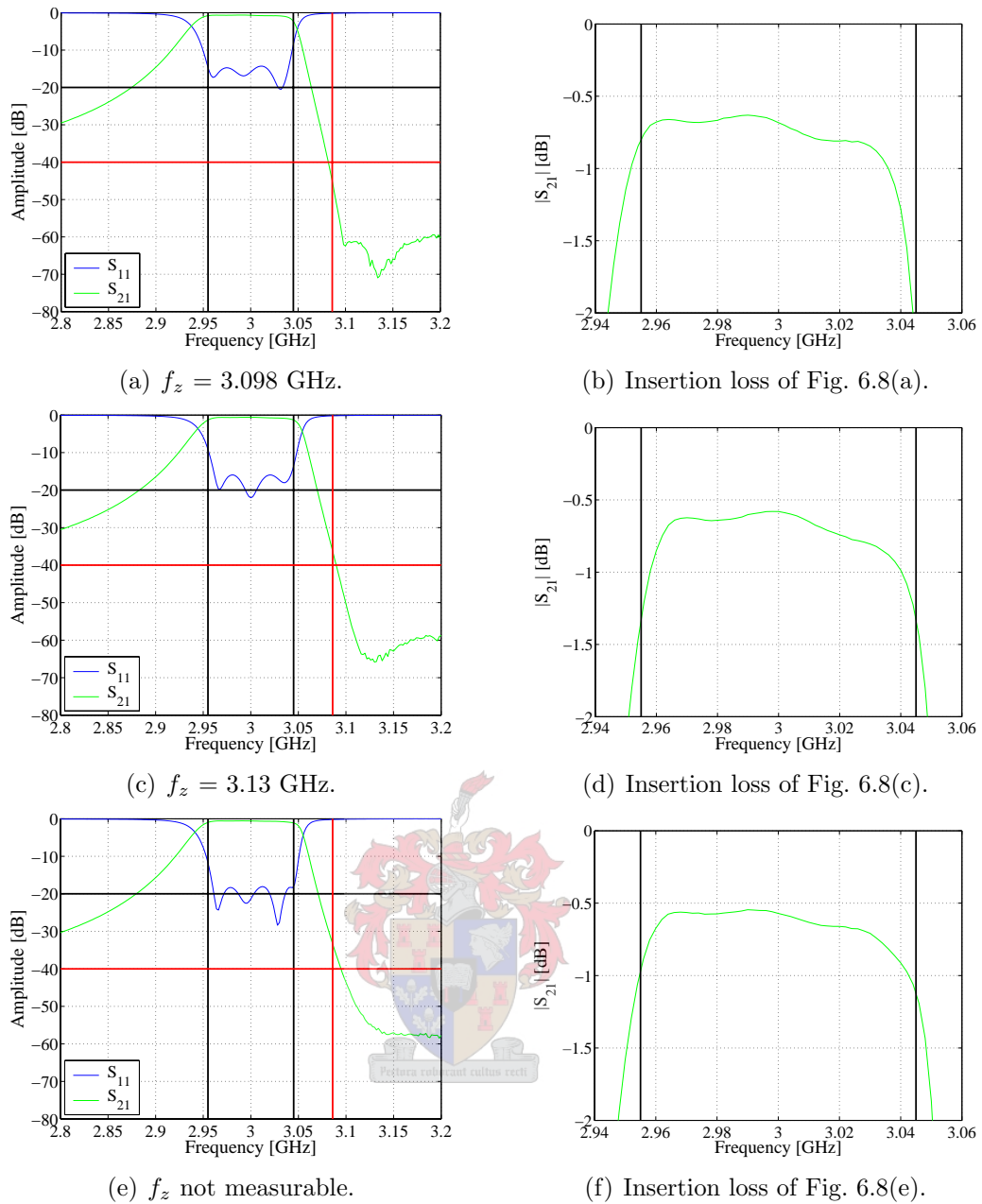


Fig. 6.8. Filter 1: Measurements with different transmission zero frequencies,  $f_z$ .

A summary of the three measurements is provided in Table 6.6.

The wide band measurement in Fig. 6.9 indicates the presence of a spurious pass band at 2.44 GHz, associated with the evanescent mode coupling element. The location of this spurious response is linked directly to the position of the transmission zero. As illustrated in Fig. 6.10, the spurious response moves down in frequency as the transmission zero is shifted up in frequency. Referring back to Fig. 6.9, the rejection level between 3.5 and 7 GHz is 80 dB. Although  $S_{11}$  and  $S_{21}$  show some activity around 8 GHz, it cannot be described as a good filtering action, as  $S_{21}$  never reaches levels higher than -10 dB.

On the whole, the first prototype filter shows good agreement with the specifications, together with good wide band performance on the high frequency side of the pass band.



	$S_{11}$ [dB]	$S_{11}$ bandwidth	$S_{21}$ at 3.086 GHz [dB]
Specification	-20.0	3.00 %	-40
Fig. 6.8(a)	-14.3	2.86 %	-45
Fig. 6.8(c)	-16.0	2.67 %	-36
Fig. 6.8(e)	-18.05	2.82 %	-34

TABLE 6.6

Summary of filter 1 narrow band measurements.

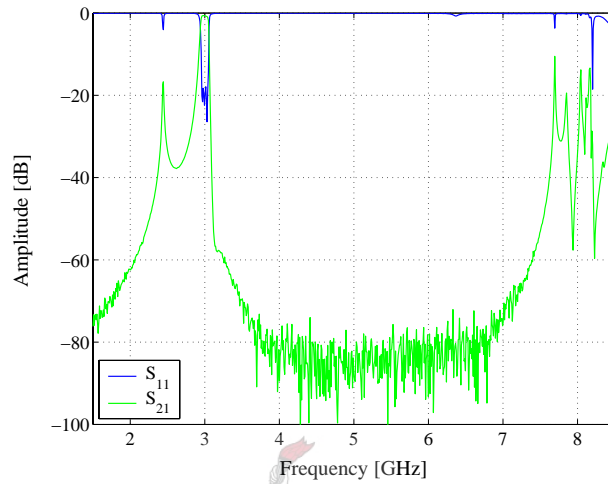


Fig. 6.9. Filter 1: Wide band measurement.

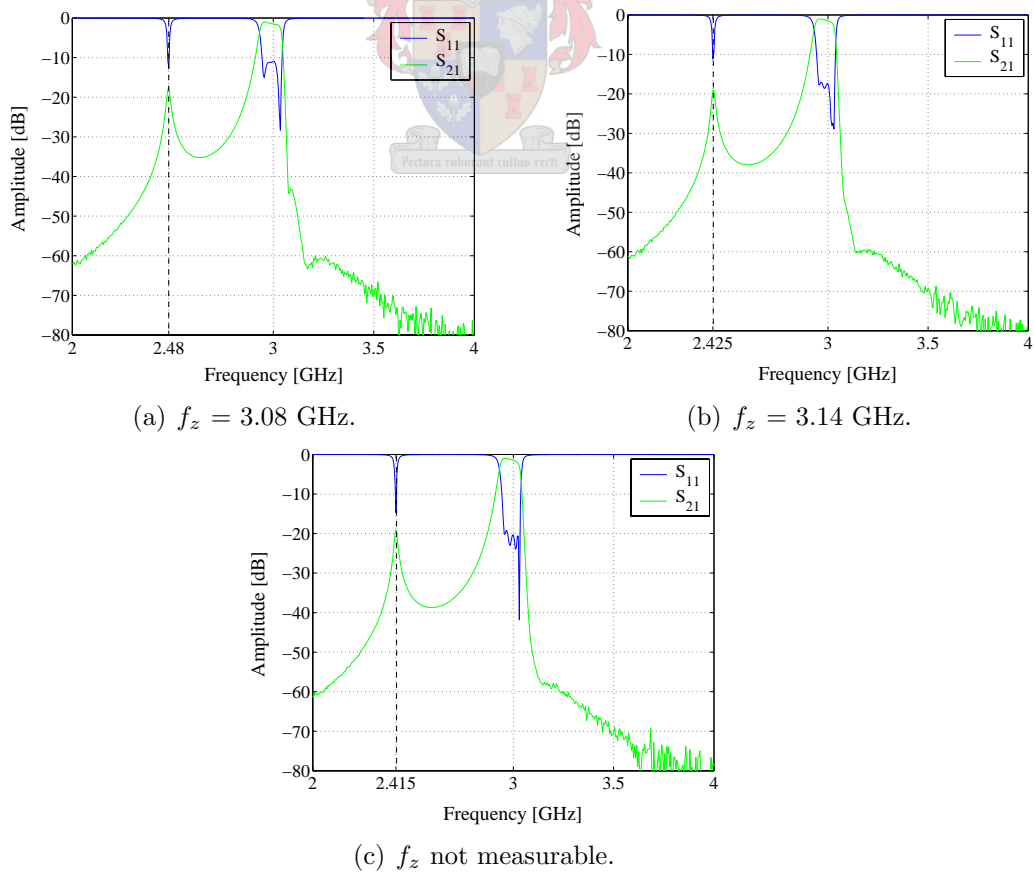


Fig. 6.10. Filter 1: Spurious response location with respect to different transmission zero frequencies,  $f_z$ .

However, the low frequency spurious response is a significant drawback of this implementation. In order to position this spurious signal as far away as possible from the pass band, considerable restrictions are placed on the dimensions of the evanescent mode coupling element. Additionally, the physical asymmetry introduced by the evanescent mode coupling element complicates the manufacturing process, thereby adding to the production costs. Tuning of the filter is also not a trivial matter, as the transmission zero is extremely sensitive with regards to the evanescent capacitive post and resonator centre frequencies.

## 6.5 Prototype Filter 2

### 6.5.1 Filter Dimensions

In order to investigate the performance of an alternative negative coupling scheme, a second filter is designed which realises  $M_{13}$  with the aid of a capacitive probe, as described in Section 4.4.3. Fig. 6.11 shows a photograph of the final prototype, with the filter roof removed. In Fig. 6.11(b), resonator 1 is located at the input port (bottom left), while resonator 4 is located at the output port (top right). Resonators 2 and 3 are in the top left and bottom right corners, respectively. The cavity spacing of this filter is symmetric, due to the fact that the capacitive coupling element does not require a wall thickness different from that of the magnetic coupling elements. Accordingly, the resonator layout shows greater correspondence with a conventional cavity resonator filter, making this filter simpler to construct than the prototype in Section 6.4.

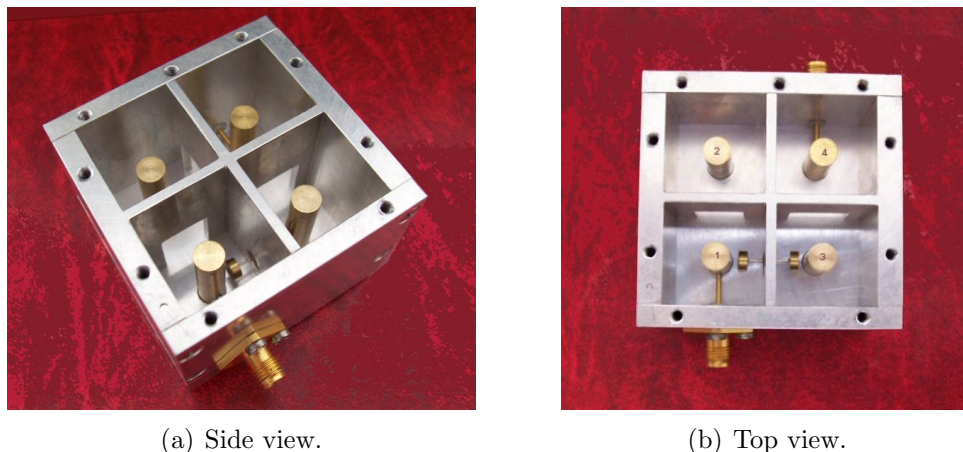
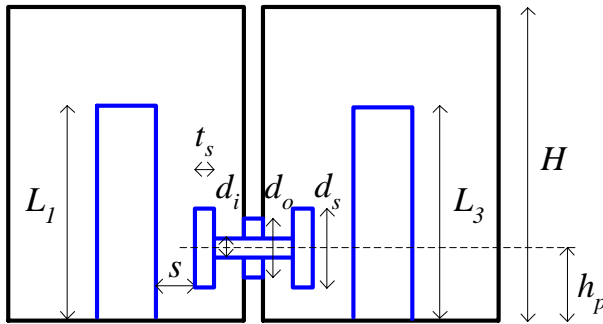


Fig. 6.11. Prototype filter two.

Next, different parts of the filter structure will be highlighted. Fig. 6.12 illustrates a side elevation with the capacitive probe coupling element and resonators 1 and 3 in the foreground. Table 6.7 contains the corresponding parameters. The probe was constructed by securing a piece of semi-rigid cable in the wall between the two neighbouring cavities, and cutting away the dielectric which extends into the two cavities, in order to expose

the thin centre conductor. Following this, two round ‘dumbbells’ were connected to the ends of the centre conductor.

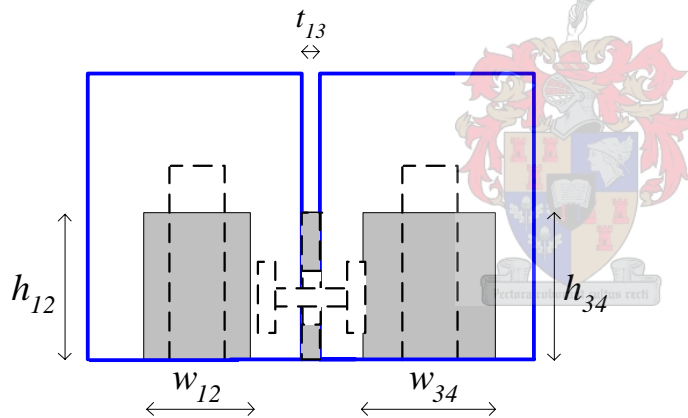


Parameter	Value [mm]
$L_1$	21.20
$L_3$	20.70
$H$	30.00
$h_p$	5.00
$s$	1.11
$t_s$	2.00
$d_i$	0.51
$d_o$	2.20
$d_s$	4.50

Fig. 6.12. Filter 2: Cavities 1 and 3 with capacitive coupling probe.

TABLE 6.7

The magnetic coupling irises realising  $M_{12}$  and  $M_{34}$  are illustrated in Fig. 6.13. As in Fig. 6.12, resonators 1 and 3 are in the foreground. Table 6.8 contains the corresponding parameter values.



Parameter	Value [mm]
$w_{12}$	10.86
$h_{12}$	13.00
$w_{34}$	13.12
$h_{34}$	13.00
$t_{13}$	2.00

Fig. 6.13. Filter 2: Cavities 1 and 3 with magnetic coupling irises.

TABLE 6.8

In order to illustrate the iris connecting cavities 2 and 4, the view in Fig. 6.13 is rotated 90° anti-clockwise, to yield the elevation in Fig. 6.14 with cavities 1 and 2 in the foreground. Table 6.9 contains the relevant parameters.

By viewing the filter from its output port in Fig. 6.15, the lengths of resonator posts 2 and 4, together with the initial tuning post lengths, can be illustrated. Table 6.10 contains the parameter values.

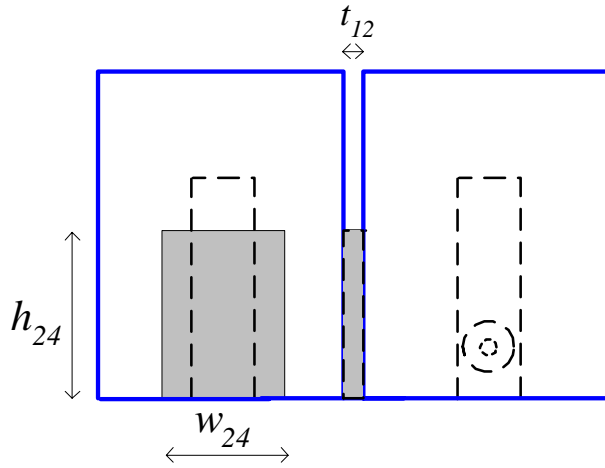


Fig. 6.14. Filter 2: Cavities 1 and 2.

Parameter	Value [mm]
$w_{24}$	10.86
$h_{24}$	13.00
$t_{12}$	2.00

TABLE 6.9

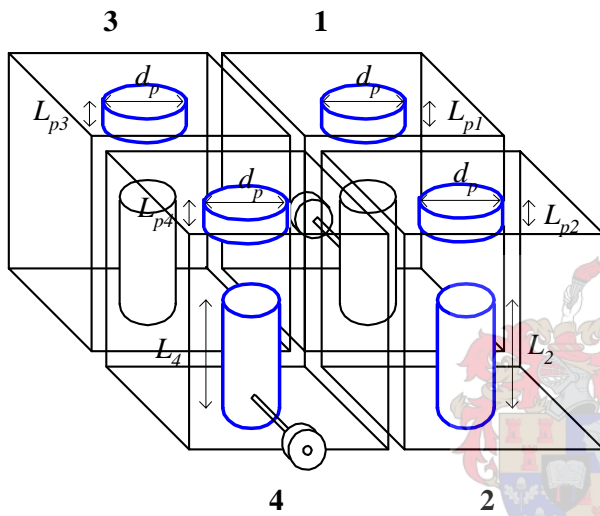


Fig. 6.15. Filter 2: Resonators 2 and 4, with filter tuning posts.

Parameter	Value [mm]
$L_2$	20.25
$L_4$	21.10
$L_{pi}$	2.00
$d_p$	8.80

TABLE 6.10

## 6.5.2 Measurements

The narrow band measurement of the second prototype filter was completed on the HP8510C VNA and is given in Fig. 6.16. Table 6.11 provides a summary of the filter performance.

	$S_{11}$ [dB]	$S_{11}$ bandwidth	$S_{21}$ at 3.086 GHz [dB]
Specification	-20.0	3.00 %	-40
Measurement	-14.8	2.013 %	-31

TABLE 6.11

Summary of filter 2 narrow band measurement.

From these measurements, it is clear that the filter's performance does not reach the specifications. To find out which parameters were causing this, parameter extraction in Microwave Office was completed with the measured S-parameters by using the model presented in Section 5.3.3. Convergence between the measurements and model response

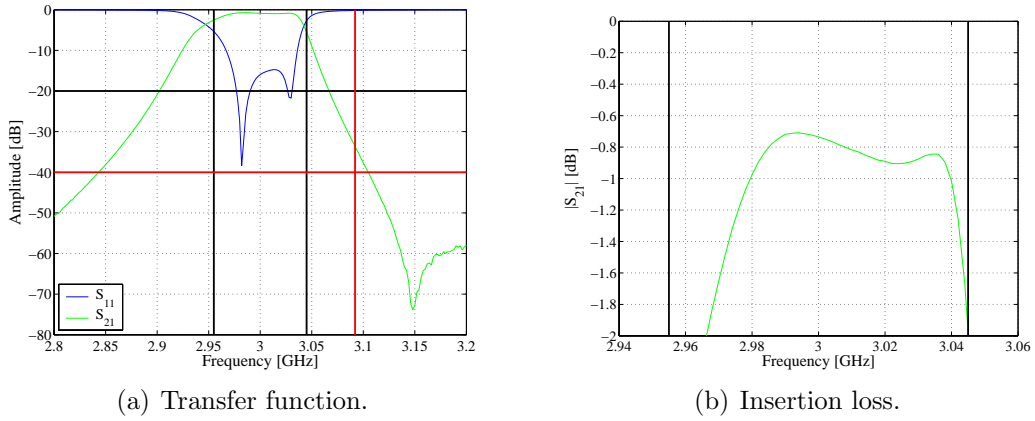


Fig. 6.16. Filter 2: Narrow band measurement.

was obtained with a very low cost value of  $4 \times 10^{-5}$ , to yield the measured coupling values in eqn. 6.4. The ideal values are given in brackets.

$$\begin{aligned}
 M_{11} &= -0.00267 \quad (-0.00135) & M_{12} &= 0.01638 \quad (0.01522) \\
 M_{22} &= 0.01319 \quad (0.02598) & M_{13} &= -0.01561 \quad (-0.02264) \\
 M_{33} &= -0.01334 \quad (-0.01524) & M_{24} &= 0.01925 \quad (0.01522) \\
 M_{44} &= -0.02228 \quad (-0.00135) & M_{34} &= 0.02457 \quad (0.02264)
 \end{aligned} \tag{6.4}$$

From eqn. 6.4 it can be seen that the extracted values of  $M_{13}$  and  $M_{24}$  differ dramatically from the ideal values. The reason for this lies in two of the coupling structures whose dimensions are out of tolerance. Firstly, the iris providing  $M_{24}$  has a width of 11.66 mm instead of 10.86 mm, thereby yielding a coupling value larger than the ideal value. A two-cavity CST simulation with the measured iris dimensions results in a coupling value of 0.0180. For the current application, this difference in coupling value is large enough to alter the filter performance.

Secondly, and more importantly, distances between the capacitive probe providing  $M_{13}$  and the resonator centre conductors were found to be too large. Fig. 6.17 provides the measurements which were made with the aid of a traveling microscope. The ideal parameter values are given in brackets next to the measured values.

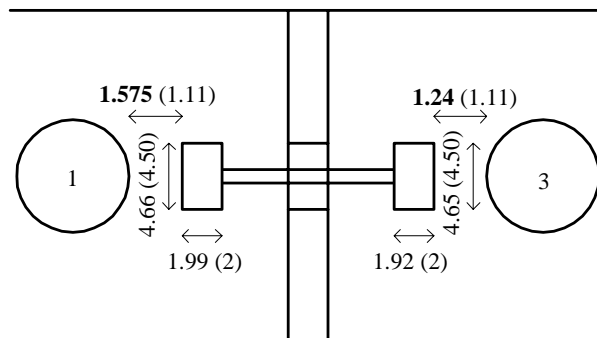


Fig. 6.17. Traveling microscope measurements of capacitive probe.

As the coupling is established by means of E-field lines existing between the resonator posts and probe, it is expected that the coupling value would depend strongly on the distances which separates these elements. This was confirmed by a CST simulation of the non-ideal coupling structure in Fig. 6.17, which yielded a coupling value of  $-0.0143$  instead on  $-0.02264$ . This is a substantial difference in terms of the filter bandwidth and centre frequency. Additionally, a severely detuned parameter will influence all the remaining coupling values, thereby degrading the filter performance even further. This can be seen in eqn. 6.4, where  $M_{12}$  shows some deviation from its ideal value, in spite of correct iris dimensions. When working with a small element like the capacitive probe, such extreme parameter sensitivity makes the manufacturing thereof time consuming and very difficult, if not impossible.

A comparison between the coupling values extracted in MWO from the measured S-parameters and those obtained with CST simulations of the traveling microscope measurements, is given in Table 6.12.

Coupling	MWO extraction	CST simulation
$M_{13}$	-0.01529	-0.0143
$M_{24}$	0.01926	0.0180

TABLE 6.12

Comparison between MWO and CST results.

The good correlation which exists between the two sets of values, serves as confirmation of the correctness of the extracted coupling values, and proves that the incorrect dimensions of elements  $M_{13}$  and  $M_{24}$  is the reason for the reduced filter bandwidth and return loss.

The wide band performance of the filter is given in Fig. 6.18.

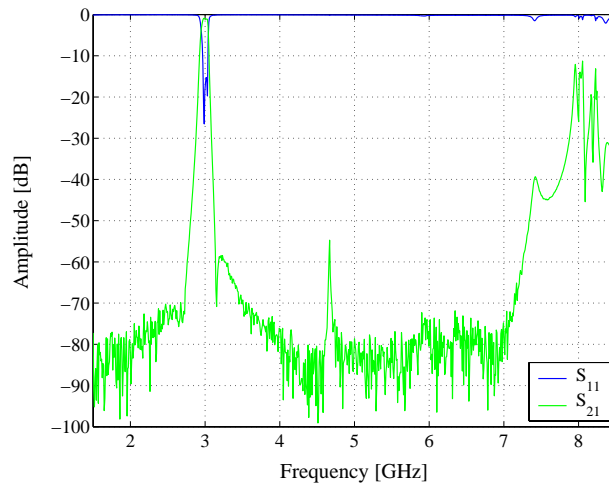


Fig. 6.18. Filter 2: Wide band measurement.

The second prototype filter shows good wide band performance, with no activity between 3 and 7 GHz, apart from a spurious signal of  $-55$  dB located at 4.6 GHz. The cause of

this spurious signal is unknown. Although  $S_{21}$  reaches levels of  $-12$  dB at 8 GHz,  $S_{11}$  levels never decrease below  $-3$  dB, which means the activity does not actually constitute a second pass band. Note the considerable improvement in the low frequency response, compared to prototype 1, due to the absence of a low frequency spurious pass band.

## 6.6 Conclusion

Two prototype filters, each realising a different negative coupling mechanism, were designed and evaluated. Good performance of prototype 1 indicates that the manufacturing tolerances of the evanescent mode coupling element lies within the required accuracy range. Manual tuning of this filter is time consuming, due to the extra tuning post in the evanescent section and high sensitivity of the transmission zero position. The presence of a low frequency spurious pass band could limit the use of this implementation.

The capacitive probe coupling element utilised in prototype 2 requires extreme manufacturing precision. A probe length of only a few tenths of a millimeter too short, causes the coupling value to change to almost half its required value. Tuning of this parameter after the initial filter assembly is practically impossible. However, this type of negative coupling realisation cannot be dismissed, as it does not require asymmetrical resonant cavities, and has the ability to yield a large range of negative coupling values, without the presence of a spurious low frequency pass band. One possible solution is to use a thicker probe without terminating disks, which is mechanically more stable and contains fewer critical dimensions. Additionally, if the filter should handle high power levels, it is essential to have only smooth edges on the probe, as sharp edges could lead to possible arcing between the probe and resonator post.

# Chapter 7

## Conclusion

With this thesis, the investigation of some of the issues related to the realisation of an asymmetric filter characteristic in coaxial coupled resonator technology is completed successfully.

The main aim of this thesis was to design, build and test two fourth order asymmetrical S-band filters through the use of coupled resonator theory. Such devices are commonly used in duplexers, which require high rejection levels in the frequency band between the transmit and receive channels.

The first problem encountered in the practical realisation of the filter, was the establishment of the required external Q-factor. Due to the non-negligible inductance in the tapped feed line structure, new theory had to be developed to facilitate the measurement of the external Q-factor.

In order to realise an asymmetrical transfer function, a coupling matrix is generated which employs both positive and negative coupling. It was therefore necessary to investigate different coupling schemes. An accepted practice is to define magnetic (H-field) coupling as positive, and electric (E-field) coupling as negative. It was found that magnetic coupling is more robust and easier to implement than electric coupling, with a large range of positive values realisable through the use of an iris placed either at the short-circuited or open-circuited end of the coaxial resonator post. To implement electric coupling with an iris, certain resonator dimensions are required, especially with regards to resonator post diameter and post length. The reason for this can be traced back to the relation between the average electric and magnetic energy at the aperture location. The limited magnitude and range of electric iris coupling eliminates its use in this project.

With the purpose of achieving larger negative coupling, the use of a single-pole evanescent mode filter and a capacitive probe were investigated. As both these coupling mechanisms yield values in the required range, two prototype filters were designed, the first reali-



sing negative coupling with an evanescent mode filter, the second achieving this with a capacitive probe.

At this stage of the design process, various parameter extraction techniques were investigated. It was found that techniques which employ the phase measurement of a short-circuited set of cavities could not be applied to the current designs, due to the effect of the tapped feed line on the phase response. Optimisation techniques which employ equivalent circuits seem to hold the most promise, as one is free to add complexity to the equivalent circuit so as to account for more complex filter characteristics.

Measurements of the first prototype filter reveal the extreme sensitivity of the transmission zero with respect to the evanescent mode capacitive post position. Although the tunability of this implementation makes it possible to adjust the filter response after manufacturing, one notable drawback is the spurious response on the low frequency side of the pass band. It was found that the tuning process which moves the spurious response down in frequency, also affects the position and existence of the transmission zero, thereby making the filter tuning a complicated and time consuming process.

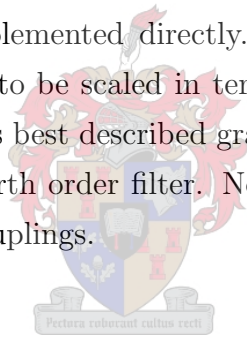
Measurements of the second prototype filter pointed out the tremendous sensitivity of the negative coupling value with regards to the capacitive probe dimensions, especially the distance between the probe and resonator post. With regards to current achievable manufacturing tolerances, such sensitivity and inability to tune, eliminates this prototype as a viable option for high performance filter designs.

In the light of these findings, the question which has to be asked, is whether the reduction in filter order which is achieved by the use of an asymmetrical transfer function, justifies the manufacturing and tuning complications brought about by the negative coupling elements. One possible solution to the larger size accompanying the increased order of symmetrical filters, could be the use of dielectric resonators to decrease the size of each resonator in the filter. Especially in terms of mass production, the implementation complexity of negative coupling elements will have to be reduced significantly in order for coaxial coupled resonator filters with asymmetrical transfer functions to be a viable technology.

# Appendix A

## Bandwidth and Frequency Scaling of the Coupling Matrix

The completion of the coupling matrix synthesis procedure outlined in Chapter 2, results in an  $n \times n$  matrix describing the coupling values and individual resonant frequency offsets of an  $n^{\text{th}}$  order coupled resonator filter. However, these values are normalised low pass couplings which cannot be implemented directly. Before the practical realisation can begin, the coupling matrix has to be scaled in terms of the appropriate bandwidth and centre frequency. This process is best described graphically, as illustrated in Fig. A.1, for the case of a direct-coupled fourth order filter. No difference exists between the scaling of direct couplings and cross couplings.



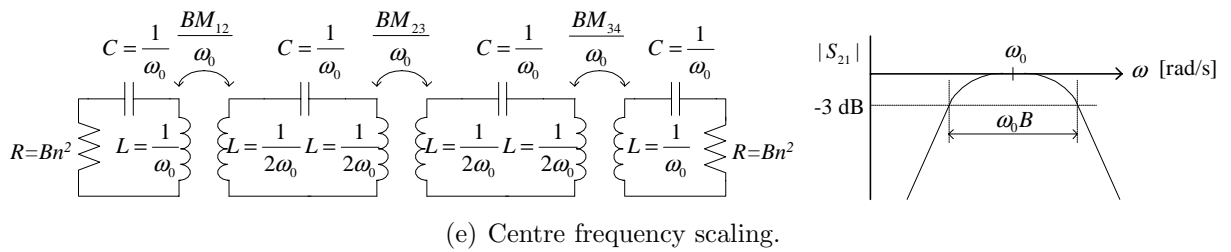
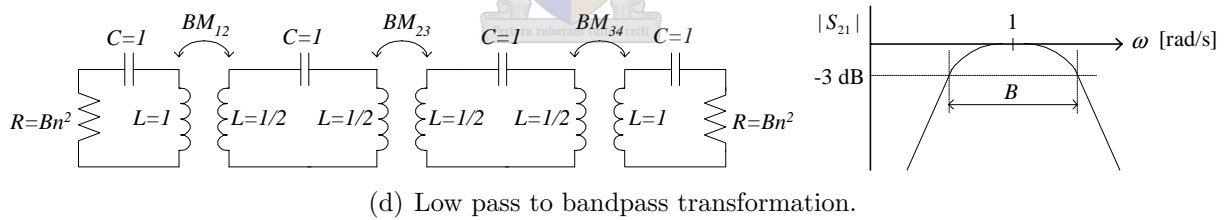
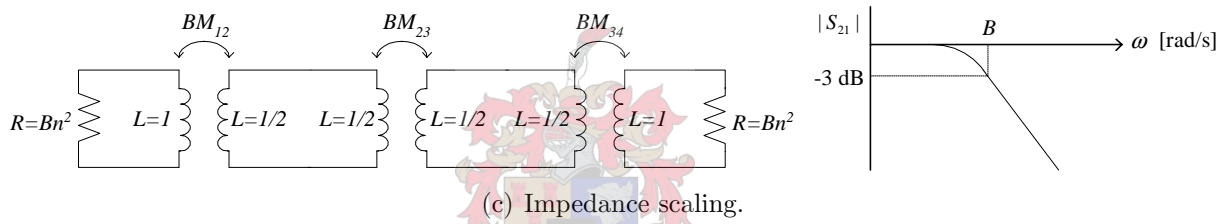
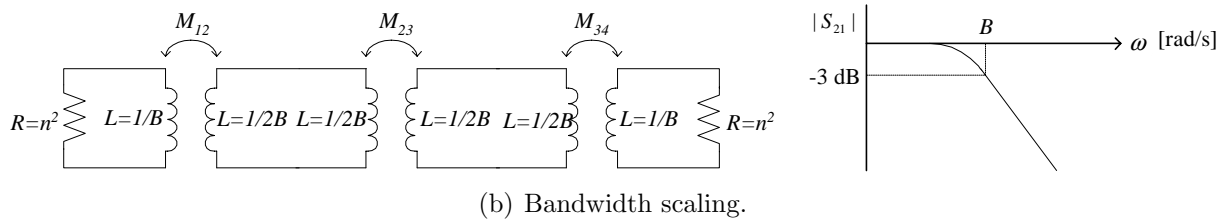
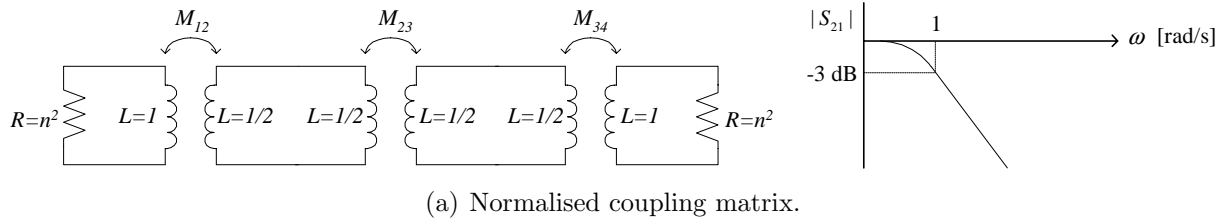


Fig. A.1. Systematic scaling of the coupling matrix equivalent circuit.

# Appendix B

## Impedance and Admittance Inverters

### B.1 General Definition

Impedance and admittance inverters operate like quarter wavelength transmission lines of characteristic impedance  $K$  and  $J$ , respectively, as depicted in Fig. B.1. As a result, impedance inverters are often referred to as K-inverters, while admittance inverters and J-inverters are synonymous.

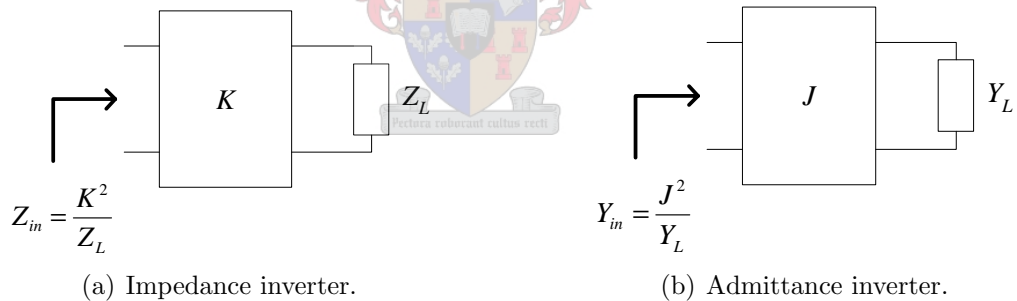


Fig. B.1. Inverter definitions.

In coupled resonator filters, impedance inverters are used in conjunction with series resonators, while admittance inverters are used with parallel resonators.

## B.2 Equivalent Circuits of K- and J-inverters

Illustrated in Fig. B.2(a), are two inductively coupled loops. Due to the equivalence of the loop equations in the two circuits of Fig. B.2, it is a well-known practice to represent an inductive coupling element as a T-network of inductors.  $M$  is defined as the mutual inductance, while  $L_s$  is the self inductance of the coupling element.

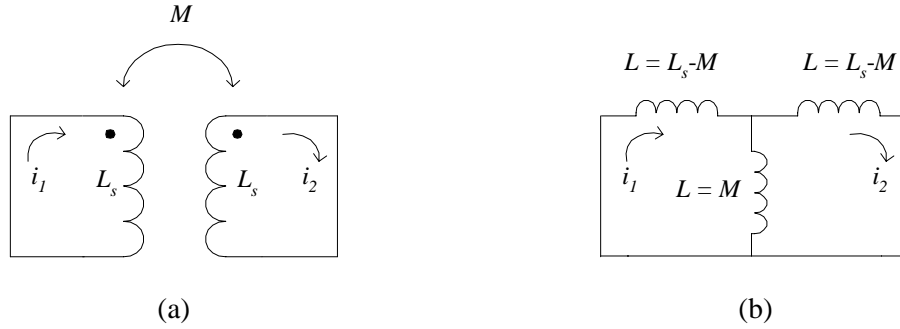


Fig. B.2. Circuit representation of magnetic coupling.

Consider the ideal coupling element with negligible self inductance and arbitrary load impedance in Fig. B.3. As  $L_s = 0$ ,  $X = \omega M$ .

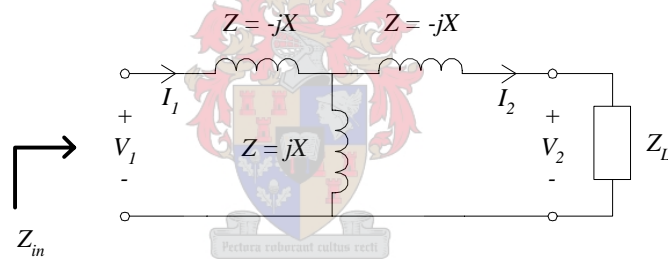


Fig. B.3. Ideal magnetic coupling element with load impedance.

The T-matrix of the coupling element in Fig. B.3 can be written as

$$\begin{bmatrix} V_1 \\ I_1 \end{bmatrix} = \begin{bmatrix} 0 & -jX \\ 1/jX & 0 \end{bmatrix} \begin{bmatrix} V_2 \\ I_2 \end{bmatrix} \tag{B.1}$$

Accordingly,

$$\begin{aligned} Z_{in} &= \frac{V_1}{I_1} \\ &= \frac{-jX I_2}{\frac{1}{jX} V_2} \\ &= \frac{X^2}{Z_L} \end{aligned} \tag{B.2}$$

Therefore, the T-network of inductors acts as an impedance inverter with  $K = X = \omega M$ .



This implies, as expected, that the T-network of inductors yields positive coupling for positive values of  $M$ .

The analysis can be repeated for the remaining impedance and admittance inverters. The results are summarised in Table B.1.

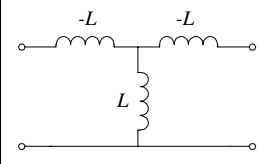
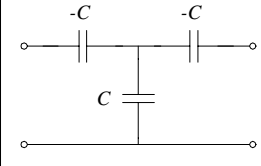
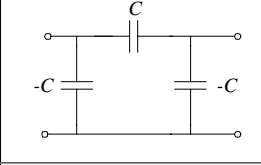
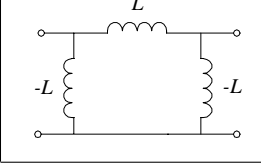
Circuit	Inverter Type	Inverter Value	Coupling
	Impedance	$K = \omega L$	Magnetic (positive) for $L > 0$
	Impedance	$K = 1/\omega C$	Electric (negative) for $C > 0$
	Admittance	$J = \omega C$	Electric (negative) for $C > 0$
	Admittance	$J = 1/\omega L$	Magnetic (positive) for $L > 0$

TABLE B.1

Summary of impedance and admittance inverters.

# Appendix C

## Derivation of Two Port Driving Point Impedance

Consider the network in Fig. C.1.

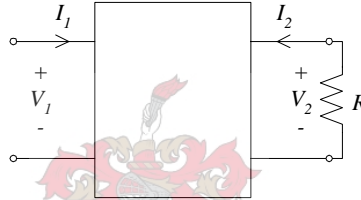


Fig. C.1. Two port network and load resistance.

In terms of impedance parameters, the port voltages and currents can be written as

$$V_1 = z_{11}I_1 + z_{12}I_2 \quad (\text{C.1})$$

$$V_2 = z_{21}I_1 + z_{22}I_2 \quad (\text{C.2})$$

Multiplication of eqn. C.1 by  $z_{21}$  and eqn. C.2 by  $z_{11}$ , and taking the difference between the two terms, yields

$$-z_{21}V_1 + z_{11}V_2 = (z_{11}z_{22} - z_{12}z_{21})I_2 \quad (\text{C.3})$$

with  $(z_{11}z_{22} - z_{12}z_{21})$  defined as  $\Delta z$ . Hence,

$$I_2 = \frac{-z_{21}}{\Delta z}V_1 + \frac{z_{11}}{\Delta z}V_2 \quad (\text{C.4})$$

which results in

$$\begin{aligned} y_{21} &= \frac{-z_{21}}{\Delta z} \\ y_{22} &= \frac{z_{11}}{\Delta z} \end{aligned} \quad (\text{C.5})$$

Next, substitute  $V_2 = -I_2R$  into eqn. C.2. It follows that

$$\begin{aligned} -I_2R &= z_{21}I_1 + z_{22}I_2 \\ \Rightarrow I_2 &= \frac{-z_{21}I_1}{z_{22} + R} \end{aligned} \quad (\text{C.6})$$

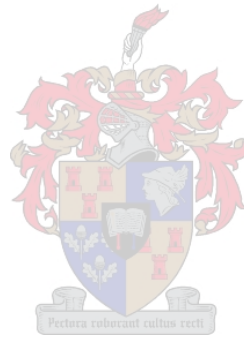


Substitution of eqn. C.6 into eqn. C.1 results in

$$\begin{aligned}\frac{V_1}{I_1} = Z_{in} &= z_{11} - \frac{z_{12}z_{21}}{z_{22} + R} \\ &= \frac{z_{11}z_{22} + z_{11}R - z_{12}z_{21}}{z_{22} + R} \\ &= \frac{z_{11} \left( \frac{\Delta z}{z_{11}} + R \right)}{z_{22} + R}\end{aligned}\tag{C.7}$$

Through the use of eqn. C.5, the driving point impedance of the two port network can be written as

$$Z_{in} = \frac{z_{11} \left( \frac{1}{y_{22}} + R \right)}{z_{22} + R}\tag{C.8}$$



# Bibliography

- [1] G.L. Ragan, *Microwave Transmission Circuits*, vol. 9 of *MIT Radiation Laboratory Series*, New York: McGraw-Hill, 1948.
- [2] H.A. Bethe, “Theory of diffraction by small holes,” *Phys. Rev.*, vol. 66, pp. 163–182, 1944.
- [3] S.B. Cohn, “Determination of aperture parameters by electrolytic-tank measurements,” *Proc. IRE*, vol. 39, pp. 1416–1421, 1951.
- [4] S.B. Cohn, “The electric polarizability of apertures of arbitrary shape,” *Proc. IRE*, vol. 40, pp. 1069–1071, 1952.
- [5] N.A. McDonald, “Electric and magnetic coupling through small apertures in shield walls of any thickness,” *IEEE Trans. on Microwave Theory and Techniques*, vol. MTT-20, no. 10, pp. 689–695, Oct. 1972.
- [6] R. Levy, “Improved large aperture waveguide coupling theory,” *IEEE MTT-S Digest*, pp. 431–433, 1979.
- [7] A.E. Atia and A.E. Williams, “New types of waveguide bandpass filters for satellite communications,” *COMSAT Technical Review*, vol. 1, no. 1, pp. 21–43, 1971.
- [8] R.J. Cameron, “General coupling matrix synthesis methods for chebyshev filtering functions,” *IEEE Trans. on Microwave Theory and Techniques*, vol. 47, no. 4, pp. 433–442, Apr. 1999.
- [9] A.E. Atia and A.E. Williams, “Narrow-bandpass waveguide filters,” *IEEE Trans. on Microwave Theory and Techniques*, vol. MTT-20, no. 4, pp. 258–265, Apr. 1972.
- [10] A.E. Atia, A.E. Williams, and R.W. Newcomb, “Narrow-band multiple-coupled cavity synthesis,” *IEEE Trans. on Circuits and Systems*, vol. MTT-21, no. 5, pp. 648–655, Sept. 1974.
- [11] D.C. Lay, *Linear Algebra and its Applications*, Addison Wesley Longman, Inc., second edition, 2000.

- [12] mathworld.wolfram.com, “Gram-schmidt orthonormalization,” 2004.
- [13] S. Darlington, “Synthesis of reactance 4-poles which produce prescribed insertion loss characteristics,” *Journal of Mathematics and Physics*, vol. 18, no. 4, pp. 257–353, 1939.
- [14] G.C. Temes and J.W. LaPatra, *Introduction to Circuit Synthesis and Design*, McGraw-Hill, Inc., 1977.
- [15] M.E. Van Valkenburg, *Introduction To Modern Network Synthesis*, John Wiley & Sons, Inc., 1960.
- [16] R. Levy, R.V. Snyder, and G Matthaei, “Design of microwave filters,” *IEEE Trans. on Microwave Theory and Techniques*, vol. 50, no. 3, pp. 783–793, 2002.
- [17] G. Matthaei, L. Young, and E.M.T. Jones, *Microwave Filters, Impedance-Matching Networks, and Coupling Structures*, Artech House, 1980.
- [18] W. Lin, “Polygonal coaxial line with round center conductor,” *IEEE Trans. on Microwave Theory and Techniques*, pp. 545–550, 1985.
- [19] A.R. Harish and J.S.K. Raj, “A direct method to compute the coupling between nonidentical microwave cavities,” *IEEE Trans. on Microwave Theory and Techniques*, vol. MTT-52, no. 12, pp. 2645–2650, Dec. 2004.
- [20] M. El Sabbagh, K.A. Zaki, H. Yao, and M. Yu, “Full-wave analysis of coupling between combline resonators and its application to combline filters with canonical configurations,” *IEEE Trans. on Microwave Theory and Techniques*, vol. 49, no. 12, pp. 2384–2393, 2001.
- [21] S.B. Cohn, “Microwave coupling by large apertures,” *Proc. IRE*, vol. 40, pp. 696–699, 1952.
- [22] R.V. Snyder, “Generalized cross-coupled filters using evanescent mode coupling elements,” *IEEE MTT-S Digest*, vol. 2, pp. 1095–1098, 1997.
- [23] G.F. Craven and C.K. Mok, “The design of evanescent mode waveguide bandpass filters for a prescribed insertion loss characteristic,” *IEEE Trans. on Microwave Theory and Techniques*, vol. MTT-19, no. 3, pp. 295–308, 1971.
- [24] A.E. Williams, R.G. Egri, and R.R. Johnson, “Automatic measurement of filter coupling parameters,” *IEEE MTT-S Digest*, pp. 418–420, 1983.
- [25] A.E. Atia and A.E. Williams, “Measurements of intercavity couplings,” *IEEE Trans. on Microwave Theory and Techniques*, pp. 519–522, June 1975.

- [26] A.E. Atia and H.W. Yao, "Tuning and measurements of couplings and resonant frequencies for cascaded resonators," *IEEE MTT-S Digest*, June 2000.
- [27] H.T.H. Hsu, H.W. Yao, K.A. Zaki, and A.E. Atia, "Computer-aided diagnosis and tuning of cascaded coupled resonator filters," *IEEE Trans. on Microwave Theory and Techniques*, vol. 50, no. 4, pp. 1137–1145, 2002.
- [28] J.B. Ness, "A unified approach to the design, measurement and tuning of coupled-resonator filters," *IEEE Trans. on Microwave Theory and Techniques*, vol. 46, no. 4, pp. 343–351, 1998.
- [29] P. Harscher, R. Vahldieck, and S. Amari, "Automated filter tuning using generalized low-pass prototype networks and gradient-based parameter extraction," *IEEE Trans. on Microwave Theory and Techniques*, vol. 49, no. 12, pp. 2532–2538, 2001.
- [30] G. Pepe, F.J. Gortz, and H. Chaloupka, "Sequential tuning of microwave filters using adaptive models and parameter extraction," *IEEE Trans. on Microwave Theory and Techniques*, vol. 53, no. 1, pp. 22–31, 2005.

